COHERENT CONTROL OF DIPOLAR COUPLED SPINS IN LARGE HILBERT SPACES

by

SUDDHASATTWA SINHA

B.Sc.(Hons.) in Physics, Indian Institute of Technology, Kharagpur, India (2001)

Submitted to the Department of Nuclear Science and Engineering
in partial fulfillment of the requirements for the degree of

DOCTOR OF PHILOSOPHY

at the

MASSACHUSETTS INSTITUTE OF TECHNOLOGY

April 2006
[June 2006]

© Massachusetts Institute of Technology 2006. All rights reserved.

Author______________________________
Department of Nuclear Science and Engineering
April 27, 2006

Certified by______________________________
David G. Cory
Professor
Thesis Supervisor

Read by______________________________
Terry P. Orlando
Professor
Thesis Reader

Read by______________________________
Seth Lloyd
Professor
Thesis Reader

Accepted by______________________________
Jeffery Coderre
Chairman, Department Committee on Graduate Students

MASSACHUSETTS INSTITUTE
OF TECHNOLOGY
OCT 12 2007
LIBRARIES

ARCHIVES

Coherent control of dipolar coupled spins in large Hilbert spaces

by

Suddhasattwa Sinha

Submitted to the Department of Nuclear Science and Engineering
on April 27, 2006, in partial fulfillment of the
requirements for the degree of
Doctor of Philosophy

Abstract

Controlling the dynamics of a dipolar-coupled spin system is critical to the development of solid-state spin-based quantum information processors. Such control remains challenging, as every spin is coupled to a large number of surrounding spins. In this thesis, we primarily focus on developing coherent control techniques for such large spin systems.

We start by experimentally simulating spin squeezing using a liquid-state NMR quantum information processor. We demonstrate that the precision of quantum control obtained using strongly modulating pulses was sufficient to reproduce the theoretically expected behavior of the spin observables and the associated entanglement measures among the underlying qubits.

We then investigate coherent control in a more complex solid-state spin system consisting of an ensemble of spin pairs. Using pulse amplitude modulation techniques, we decouple the weaker interactions between different pairs and extend the coherence lifetimes within the two-spin system. This is achieved without decoupling the stronger interaction between the two spins within a pair. We thus demonstrated that it is possible to restrict the evolution of a dipolar coupled spin network to a much smaller subspace of the system Hilbert space which allows us to significantly extend the phase coherence times for selected states.

Finally, we demonstrate the sensitivity of highly correlated multiple-quantum states to the presence of rare spin defects in a solid-state spin system. We design two multiple-pulse control sequences - one that suspends all spin interactions in the system including that of the defect spins, while the other selectively allows the defect spins to interact only with the abundant spins. By measuring the effective relaxation time of the rare spins, we demonstrate the efficiency of the two control sequences. Furthermore we observe that for small spin cluster sizes, the sensitivity of the highly correlated spin states to the spin defects depends on the coherence order of these correlated spin states. But beyond a certain cluster size, one observes a saturation effect as the higher coherence orders are no longer increasingly sensitive to the defect spin dynamics.

Thesis Committee Member: David G. Cory
Title: Professor

Acknowledgments

I would like to thank Professor David Cory for giving me the opportunity to work with him and guiding me for the past four years. His insight on every aspect of Nuclear Magnetic Resonance and Quantum Information Processing has been inspiring. I would also like to acknowledge Dr. Sekhar Ramanathan for his help and advice. He has been intimately involved in the each and every one of my research projects and has been extremely supportive all through out. His words of encouragement and compassion have especially helped me get through the past six months when things were not going well.

Among my group mates, first and foremost I would like to thank all my office mates – Paola (the fille fille), Jonathan (the bike shop garçon) and Nick (the garçon garçon). It was a lot of fun working with them over the past few years on various research projects and problem-sets. It was always a pleasure working with Joon (the probe garçon) trying to tune probes and run solid-state NMR experiments. I would also like to thank Jamie (the cool garçon), Michael (the dude garçon), Anatoly (the DNP garçon), Ben (the cake garçon), Dima (the Russian garçon) and Cecilia (the party fille). It had a wonderful experience spending time with them in the lab. I would also like to thank some of the people who had helped me get started during my first year at MIT including Evan, Marco, Grum, Yaakov and Dr. Timothy Havel and Dr. Joseph Emerson.

Outside the lab, I would like to thank all my friends in Ashdown. The list is too long to enumerate here. But their friendship has made my MIT experience even more rewarding. I have many fond memories of my years at MIT and I will cherish them for the rest of my life.

Finally, I would like to thank my family - my parents and my sister. It would be impossible for me to convey my gratitude to them in a few sentences. All I can say is: without their love and support I would not have seen this day.

In loving memory of Bapi (father):

His perseverance and dedication will always inspire me;
His encouragement and ideals will forever guide me;
His love and affection will never cease to comfort me.

CONTENTS

Abstract **3**

Acknowledgments **5**

Table of Contents **9**

List of Figures **13**

List of Tables **21**

1 Introduction **23**

2 Experimental Simulation of Spin Squeezing by NMR **27**

2.1 Introduction 27

2.2 Simulation of spin squeezing in a multi-spin–1/2 system 28

2.3 The NMR implementation of squeezed spin states 32

2.4 Results of spin squeezing experiments 36

2.4.1 The spin-1 case 39

2.4.2 The spin–3/2 case 39

    2.4.3 Behavior of entanglement measures 41

  2.5 Conclusions 44

3 Selective coherence transfers in homonuclear dipolar coupled spin systems 47

  3.1 Introduction 47

  3.2 Theory of the modulation scheme 49

  3.3 Experimental Results 52

  3.4 Conclusions 55

4 Sensitivity of highly correlated multiple-spin states to the presence of rare spins 59

  4.1 Introduction 59

    4.1.1 Creation and detection of highly correlated multiple-quantum states 60

    4.1.2 Decay of highly correlated multiple-spin states in CaF$_2$ 63

    4.1.3 Effect of rare spins on the decay of the multiple-spin states. . 65

    4.1.4 Sensitivity the of highly correlated multiple-spin states to the presence of rare spins 70

  4.2 Overview of average Hamiltonian theory 71

  4.3 The C-48 time-suspension sequence 73

  4.4 The design criteria for the new time-suspension and heteronuclear recoupling sequences 77

  4.5 The properties of the TS-96 and the HR-96 sequences 82

  4.6 Experimental Results 84

4.6.1 Effective T_2 relaxation times of ^{13}C spins under the TS-96 and the HR-96 sequences. 84

4.6.2 Sensitivity of ^{1}H multiple quantum coherence to the presence of ^{13}C spins 87

4.7 Conclusions and future work 90

A Zeroth order average Hamiltonian calculations for the TS-96 and the HR-96 sequences 95

LIST OF FIGURES

2-1 (i) A coherent state spin–j vector with expectation values $[\langle J_x\rangle, \langle J_y\rangle, \langle J_z\rangle] = [1,0,0]$ may be visualized as a coherent superposition of angular momentum vectors on a cone about the x-axis, all with a projection of $j/2$ along that axis. (ii) After squeezing via the one-axis mechanism (see text), the cone representing the state of a spin–1 particle is elliptical, with its squeezed (minor) axis making an angle of $\pm\pi/4$ with the y,z–axes. (iii) In the maximally squeezed state of a spin–1 particle the cone has been folded into a nearly degenerate ruled surface. 29

2-2 The molecular structure of 2,3-dibromo-thiophene is shown on the left, with the two hydrogen atoms used for the spin–1 simulations numbered as in the main text. The coupling strength J between them and the chemical shift of the first compared to the second are also shown. The diagram on the right shows the pulse sequence used to implement spin squeezing for a given parameter k, where $f(k) \equiv k/(2\pi J)$, narrow rectangles indicate $\pi/2$ y-rotations, the broad rectangles y-rotations by π, and the rectangles point downwards for pulses effecting rotations by the negatives of these angles. 34

2-3 The molecular structure alanine is shown on the left, with the three carbon-13 atoms used for the experiments numbered as in the text. The numbers next to the dashed lines are the corresponding coupling constants (in Hz), while the numbers next to the carbons are their chemical shifts relative to the third (in Hz). On the top right is a schematic diagram of the pulse sequence used, where the horizontal striping indicates an y-pulse, vertical striping an x-pulse, the narrower pulses induce rotations by $\pi/2$, and the wider ones by π (or the negatives thereof if the pulse is below the spin's line). The grey boxes indicate one of the two "modules" show on the bottom right, which allow a $I_z^m I_z^n$ evolution by the angle (k or $\pi/2$) shown on the bottom of the pulse sequence diagram while refocussing the chemical shifts and the coupling between the pairs not contained in the grey box. The functions which relate the delay time to the squeezing parameter k is given by $f_{mn}(k) \equiv k/(4\pi J^{mn})$ for $[m,n] = [1,2],[2,3]$. 35

2-4 (i) The real part of the experimental density matrix representing the initial pseudo-pure state $|00\rangle$ for the spin–1 experiments. (ii) The real part of the experimental density matrix representing the maximally squeezed state of the effective spin–1 particle. 38

2-5 (i) The real part of the experimental density matrix representing the initial pseudo-pure state $|000\rangle$ for the spin–3/2 experiments. (ii) The real part of the density matrix when the squeezing parameter $k = \pi/2$, at which point a GHZ state is obtained [28]. 38

2-6 Plots of the theoretically expected uncertainties as a function of the squeezing parameter k (in degrees) for spin–1 (solid lines), along with the fits (dashed lines) to the uncertainties computed from the experimental density matrices (+ or $*$). (i) Plots of $\langle \Delta \mathrm{J_y} \rangle$ (lower curves), and $\langle \Delta \mathrm{J_z} \rangle$ with k (upper curves). (ii) Plot of $|\langle \mathrm{J_x} \rangle|$ (no fits shown). . 40

2-7 Plots of the theoretically expected uncertainties as a function of the squeezing parameter k (in degrees) for spin–3/2 (solid lines), along with fits (dashed lines) to the uncertainties computed from the experimental density matrices (+ or $*$). (i) Plots of $\langle \Delta \mathrm{J_y} \rangle$ (lower curves) and $\langle \Delta \mathrm{J_z} \rangle$ (upper curves). (ii) Plot of $|\langle \mathrm{J_x} \rangle|$. 42

2-8 Plots of the entanglement of formation (i) and concurrence (ii) with the squeezing parameter k (in degrees) for spin–1. The solid lines are the theoretically expected curves, while the dashed lines interpolate linearly between the values computed from the experimental density matrices ($*$) obtained via tomography. 43

2-9 Plots of the Meyer's metric or average entanglement after tracing down to a single qubit (i) and concurrence after tracing down to any pair of qubits (ii) with the squeezing parameter k (in degrees) for spin–3/2. The solid lines are the theoretically expected curves, while the dashed lines are a fifth-order polyomial fit to the values computed from the experimental density matrices ($*$) obtained via tomography. 44

3-1 Two pairs of strongly coupled spin–$\frac{1}{2}$ systems with each pair decomposed into its singlet and triplet manifolds (in the rotating frame). The triplet manifolds are weakly coupled to each other while the singlet manifolds do not interact. 51

3-2 (a) The proton spectrum of a single crystal of gypsum in the [010] orientation (Pake doublet). The splitting between the peaks corresponds to $3\omega_D^S/2\pi = 44.4$ KHz. Each peak is broadened due to weak dipolar coupling to the other water molecules. Therefore, $3\omega_D^w/2\pi \sim 16.4$ KHz (b) The line narrowing observed under the modulation sequence with RF amplitude $\omega_1 = 3\omega_D^S/4$. (c) Evolution of the collective single spin $\sum_i \sigma_x^i$ terms under the modulation sequence. 54

3-3 (a) pulse sequence used to read out the $\sigma_x^1 + \sigma_x^2$ terms. Following the modulation pulse, a $\pi/2$ pulse is applied to rotate the σ_x terms to σ_z. During the 150 μs interval (much shorter than T_1) all terms other than the σ_z decay. A $\pi/2$ pulse is then used to monitor σ_z. (b) pulse sequence used to read out the $\sigma_y^1\sigma_z^2 + \sigma_z^1\sigma_y^2$ term. Following the modulation two back to back $\pi/2$ pulses act as a double quantum filter to suppress the single spin σ_x terms. A four step phase cycle is necessary to implement the filter. 55

3-4 The solid line shows the $\sigma_x^1 + \sigma_x^2$ and the dashed line shows the $\sigma_z^1\sigma_y^2 + \sigma_y^1\sigma_z^2$ terms. (a) Under the dipolar Hamiltonian evolution, the above terms evolve into unobservable higher order spin correlations within 100 μs. (b) Under the modulation sequence, the terms oscillate 90 deg out-of-phase with each other for up to 360 μs without any significant attenuation in amplitude. In this case the RF amplitude $\omega_1 = 3\omega_D^S/4$. 56

3-5 The solid line shows the $\sigma_x^1 + \sigma_x^2$ and the dashed line shows the $\sigma_z^1\sigma_y^2 + \sigma_y^1\sigma_z^2$ terms. Under the modulation sequence, the terms oscillate 90 deg out-of-phase with each other. The RF amplitude ω_1 is varied from $2\omega_D^S/4$ to $7\omega_D^S/4$ in steps of $\omega_D^S/4$. When the value of ω_1 is no longer in the optimum range, the amplitude of the signal is significantly attenuated. 57

4-1 Energy level diagram of a N spin-$\frac{1}{2}$ system. The eigenvalue of $\widehat{I}_z$ can take any value from $\frac{N}{2}$ to $\frac{-N}{2}$. The number of levels for each allowed eigenvalue is $\binom{N}{m+\frac{N}{2}}$. Thus the number of allowed single-quantum transitions increase exponentially with N and are thus unresolvable in large spin-systems. 61

4-2 The basic form of a multiple-quantum NMR experiment [63] - (i) Preparation: Creating the highly correlated multiple-quantum states. (ii) Evolution: Evolving these states under any desired Hamiltonian. (iii) Mixing: Transforming the higher order coherences to observable single-spin single quantum coherences. (iv) Detection: Measuring the observable single-spin single quantum magnetization 62

4-3 Effective decay times of various coherence orders due to the action of the secular dipolar Hamiltonian. Highly correlated spin-^{19}F states in CaF_2 are created by exciting the thermal spin-^{19}F state using the DQ Hamiltonian. The effective decay times of the coherences for the various excitation times (τ_1) are plotted. 64

4-4 Effective decay times of various coherence orders of the the highly correlated spin-^{19}F states in CaF_2. In this case, the secular dipolar Hamiltonian is suppressed using a multiple-pulse C-48 sequence. The effective decay times of the coherences for the various excitation times (τ_1) under the DQ Hamiltonian are plotted. 65

4-5 The model system (on the right), consists of one **S** spin (labeled as $\mathbf{S_1}$) interacting with an abundant number of **I** spins. The C-48 sequence averages out the homonuclear interaction between the **I** spins during τ_2. During this time interval (τ_2), $\mathbf{S_1}$ is correlated with the multiple-quantum spin-**I** states present in $\rho(\tau_1)$. But if the $\mathbf{S_1}$ spin state remains constant during τ_2, the heteronuclear interaction is also averaged out under the action of the C-48 sequence. Thus $\mathbf{S_1}$ is *no longer correlated* to the spin-**I** states at the end of τ_2. However if $\mathbf{S_1}$ flips at any point during this interval, it will *remain correlated* with the spin-**I** states even at the end of τ_2. 67

4-6 The model system (on the right), consists of one **S** spin (labeled as $\mathbf{S_1}$) interacting with an abundant number of **I** spins and a few neighboring **S** spins. We assume that these **S** spins interact *only* with the $\mathbf{S_1}$ spin. The homonuclear interaction between the **I** spins is averaged out during τ_2 using the C-48 sequence. The Hamiltonians $H_D^{IS_1}$ and $H_D^{SS_1}$ do not commute. Thus the multiple-quantum spin **I** states present in $\rho(\tau_1)$ evolve under their action during τ_2. 68

4-7 Sketch of the experiments designed to detect rare spins (**S**) using the highly correlated multiple-spin states of the abundant spins (**I**) as a 'probe'. It involves contrasting the effect of the two control sequences (in (a) and (b)) on the intensity of the multiple quantum coherence of these correlated spin **I** states. 71

4-8 The schematic diagram of the three-pulse sequences used to design the C-48 sequence, where the horizontal striping indicates an y-pulse, vertical striping an x-pulse. All the pulses induce rotations by $\pi/2$. (or the negatives thereof if the pulses are below the bold reference lines) . 75

4-9 The schematic diagram of the three-pulse sequences used to design the C-48 sequence, where the horizontal striping indicates an y-pulse, vertical striping an x-pulse. All the pulses induce rotations by $\pi/2$. (or the negatives thereof if the pulses are below the bold reference lines) . 76

4-10 (a) The first sub-cycle (n=1) of the time-suspension (TS-96) sequence: **I**-(Aa), **S**-(aE). The sequence is made up of 16 such sub-cycles. The horizontal striping indicates an y-pulse, vertical striping an x-pulse. All the pulses induce rotations by $\pi/2$. (or the negatives thereof if the pulses are below the bold reference lines). 80

4-11 (a) The first sub-cycle (n=1) of the heteronuclear recoupling (HR-96) sequence: **I**-(Aa), **S**-(bE). The sequence is made up of 16 such sub-cycles. The horizontal striping indicates an y-pulse, vertical striping an x-pulse. All the pulses induce rotations by $\pi/2$. (or the negatives thereof if the pulses are below the bold reference lines). 81

4-12 The schematic of the experiment that measures the effective T_2 of the ^{13}C in adamantane under (a) TS-96 sequence and (b) HR-96 sequence. Before applying the two sequences, we use a $\pi/2$ pulse to flip the ^{13}C spins on to the transverse plane. The ^{13}C magnetization is measured while decoupling the ^{1}H spins. 84

4-13 The ^{13}C signal intensity plotted after every 96- pulse cycle of the the TS-96 (□) and the HR-96 (◇) sequences. The cycle time period of 1728 μs. 85

4-14 The ^{13}C signal intensity plotted after every 6 pulse sub-cycle of the (a) TS-96 and (b) HR-96 sequences. The sampling rate in both cases is 108 μs. The points marked by □ in (a) and ◇ in (b) indicate the signal intensity after the full 96-pulse sequence. The system was evolved up to 4 cycles of the 96-pulse sequences with a cycle time period of 1728 μs. 86

4-15 The schematic of the experiment that creates ^{1}H multiple quantum coherences in adamantane. The 16 pulse sequence in the shaded box is used to generate the effective DQ Hamiltonian. The smaller spacing between the pulses is given by Δ while the larger spacing is given by the sum of 2Δ and the $\pi/2$ pulse length. Thus the cycle time of the sequence is $t_c = 24(\Delta + \pi/2$ pulse length). The vertical striping indicates an x-pulse. All the pulses induce rotations by $\pi/2$. (or the negatives thereof if the pulses are below the bold reference lines) . . . 87

4-16 The ^{1}H multiple quantum coherence in adamantane. The system was evolved under the DQ Hamiltonian for a period of 604.8 μs. 88

4-17 Coherence order distribution after evolution under the TS-96 (solid line), two back-to-back C-48 (dashed line) and the HR-96 (dotted line) sequences. The cycle time was 1.4ms for all three sequences. Thus, the time period of evolution (τ_2) were 1.4 ms (for the top figure) and 2.8 ms (for the bottom figure). 89

4-18 The net difference in signal intensity for the various coherence orders after one cycle of the TS-96 and HR-96 sequences. 90

LIST OF TABLES

2.1 The representation of a spin–1 by two spin–1/2 particles 30

2.2 Coupled representation ($|j, m\rangle$) of the basis states spanned by three spin–1/2 particles 30

2.3 Theoretical and experimental spin expectation values and uncertainties of the maximally squeezed spin–1 states 39

2.4 Theoretical and experimental spin expectation values and uncertainties of the maximally squeezed spin–3/2 states 41

4.1 The average Hamiltonian for various time-suspension sequences . . . 73

4.2 Composition of the sub-cycles of the TS-96 and HR-96 sequences . . 79

4.3 The average Hamiltonian properties of the TS-96 and the HR-96 sequence taking into account finite pulse width effects 82

4.4 Sub-cycles at which the various interactions average to zero for the TS-96 and the HR-96 sequences *without* taking into account finite pulse width effects 83

4.5 Sub-cycles at which the various interactions average to zero for the TS-96 and the HR-96 sequences taking into account finite pulse width effects 83

A.1 The 0^{th} order heteronuclear average Hamiltonian values for the TS-96 (top) and the HR-96 (bottom) sequences 95

A.2 The 0^{th} order heteronuclear average Hamiltonian values for the TS-96 sequence 96

A.3 The 0^{th} order heteronuclear average Hamiltonian values for the HR-96 sequence 96

A.4 The 0^{th} order spin-**I** homonuclear average Hamiltonian values for the C-48 sequence 97

A.5 The 0^{th} order spin-**S** homonuclear average Hamiltonian values for the TS-96 sequence 98

A.6 The 0^{th} order spin-**S** homonuclear average Hamiltonian values for the HR-96 sequence 99

CHAPTER 1

INTRODUCTION

Quantum information processors (QIPs) derive their power from the quantum parallelism due to the superposition of quantum states. An n-qubit quantum information processor forms a superposition of 2^n states, with each state being equivalent to a n-bit classical processor. Peter Shor, Lov Grover and other scientists have harnessed this massive power to devise quantum algorithms like the factorization and the quantum database search algorithm. Compared to their classical counterpart, a QIP provides a more efficient platform to solve certain problems. Physical realization of a QIP requires precise quantum control of a physical system while protecting the system from decoherence effects induced by noise in the environment. Coupled with the fact that, as we push Moore's law to its limit with nano-scale devices - a regime where nature follows the laws of quantum physics, development of quantum control techniques assumes added importance.

Various schemes have been proposed for the experimental realization of QIPs including ion traps [1], cavity QEDs [2] and SQUIDs [3]. But the experimental implementation of a QIP based on liquid-state Nuclear Magnetic Resonance (NMR) technology has been the most successful till date [4, 5]. Existing coherent control NMR techniques have been adopted to manipulate up to 10 qubits while new techniques have been developed to account for incoherent and decoherent noise. These advances have enabled researchers to experimentally implement some of the quantum algorithms. However this implementation scheme has its limitations - the non-scalability of the initial state (known as the pseudo-pure state) preparation, large ratio of the gate time over the decoherence time, among others. The method of addressing qubits using chemical shifts becomes increasingly cumbersome as the complexity of the molecules increase with the number of qubits. This severely limits the maximum number of qubits that can be manipulated using this technology.

Solid-state spin-based NMR QIP has been proposed as the next generation processor. The ability to create higher thermal polarization using existing solid-state NMR techniques, the stronger dipolar couplings and the longer spin-lattice relaxation times partially address the issues of scalability, faster quantum gates and higher decoherence times respectively. Using gradient fields to address spins in solid samples removes some of the limitations one faces while addressing a large number of qubits in its liquid-state counterpart. To simulate a QIP, various solid-state system designs have been suggested - single crystals of deuterated molecules with dilute concentration of suitably labeled ones [6], phosphorous atoms in a silicon grid at a low temperature [7], endohedral fullerenes on a silicon surface [8], among others.

In any implementation of a solid-state spin-based NMR QIP, an underlying challenge is the coherent control of spins in large Hilbert spaces. Unlike liquid samples where all intramolecular interactions are averaged out due to molecular motions, in a rigid-solid lattice all nuclear spins strongly interact with each other. Thus the solid-state spin system spans a much larger Hilbert space. The control of spin dynamics in such large Hilbert spaces is essential for the application of quantum gates - a key step in the implementation of quantum algorithms. Experimental investigation of these multi-spin dynamics have been carried out using multiple-quantum coherence [9, 10, 11, 12] and spin diffusion [13, 14] techniques. In this thesis, we primarily focus on developing new coherent control techniques for such large spin systems.

We start by experimentally simulating spin squeezing using a liquid-state NMR QIP (chapter 2). This was done by identifying the energy levels within the symmetric subspace of a system of n spin$-1/2$ nuclei with the energy levels of the simulated spin–($n/2$) system. The results obtained for our simulations of spin–1 and spin–3/2 systems are consistent with earlier theoretical studies of spin squeezing. We demonstrate that the precision of quantum control obtained using strongly modulating pulses [31] was sufficient to reproduce the theoretically expected behavior of the spin observables and the associated entanglement measures among the underlying qubits. Then we investigate coherent control in a more complex solid-state spin system consisting of an ensemble of spin pairs (chapter 3). Using pulse amplitude-modulation techniques, we decouple the weaker interactions between different pairs and extend the coherence lifetimes within the two-spin systems. This is achieved without decoupling the stronger interaction between the two spins within a pair. Finally, we demonstrate the sensitivity of highly correlated spin states to the presence of rare spin defects in a solid-state system (chapter 4). We show that the homonuclear dipolar interactions of the rare spins can cause decoherence effects in such correlated spin states even if these spins are decoupled from the correlated spin system. For our sensitivity measurements, we design two multiple-pulse control techniques (based on coherent averaging theory) - one that suspends all spin interactions in the system while the other selectively allows only the heteronuclear dipolar interaction between the rare spins and the correlated spin system. By measuring the effective relaxation time of the rare spins, we demonstrate the efficiency of the two control sequences. Furthermore, we observe that the sensitivity of the highly correlated spin states to defects depends on the coherence order of the correlated spin states. But beyond a certain cluster size, one observes a saturation effect in the sensitivity measurements as the higher coherence orders are not increasingly sensitive to the defect spin dynamics.

CHAPTER 2

EXPERIMENTAL SIMULATION OF SPIN SQUEEZING BY NMR

2.1 Introduction

The minimum uncertainty associated with complementary observables is given by the uncertainty relations. For example, the position and momentum fluctuations in a coherent state of the quantum harmonic oscillator are both equal to the quantum limit $\hbar/2$. States for which the fluctuations in one of these observables is less than the standard quantum limit of $\hbar/2$, while the fluctuations in the complementary observable increase so as to satisfy the uncertainty relation, are called "squeezed states" [17, 34]. Thus a squeezed state can be visualized as an ellipse of constant uncertainty in phase space.

Squeezed spin states have been defined using analogous criteria [19, 25, 36, 42, 43, 44, 45], and several experimental demonstrations of spin squeezing have been published. They include interaction of collection of atoms with squeezed radiation [15], the displacement of two optical lattices with respect to each other [37], and collisional interactions between the atoms in a Bose-Einstein condensate [19, 36, 38].

---

[1] Parts of this chapter were extracted from the paper "Experimental simulation of spin squeezing by Nuclear Magnetic Resonance", by S. Sinha, J. Emerson, N. Boulant, T. F. Havel and D. G. Cory, *Quantum Information Processing, Vol. 2, No. 6, December 2003.*

Spin squeezing by quantum non-demolition measurements has also been proposed [26].

A spin $1/2$ is always in a coherent state, but it is possible to squeeze the "effective" higher spin with $j = n/2$ that lives within the symmetric manifold of states in a system of $n > 1$ spins each with $j = 1/2$ [20, 33]. In this paper we describe experimental realizations of squeezed states of these simulated higher order spins on a liquid-state nuclear magnetic resonance (NMR) quantum information processor, using the method suggested by Kitagawa [25]. First, we review the properties of coherent spin states and Kitagawa's method for creating squeezed spin states, along with the representation of a spin–j system for $j = 1$ and $3/2$ within the totally symmetric subspace of the Hilbert space of $2j$ spin–$1/2$ particles. We then describe the NMR implementation of the method and the measures used to access its overall precision, after which experimental results of squeezing are presented and the level of control attained is discussed. We end by verifying the relation between the degree of squeezing of the simulated spin–j system and the degree of pure state entanglement among the underlying spin–$1/2$ particles, as quantified by various well-established entanglement measures (cf. [18, 36, 37]).

2.2 Simulation of spin squeezing in a multi-spin–1/2 system

Throughout the remainder of this paper we will work with units such that $\hbar = 1$. Coherent spin states (CSS) may then be defined by the following properties: (i) The uncertainty relation for the total angular momentum operator J becomes saturated, i.e. $\Delta J_{\mathsf{x}} \Delta J_{\mathsf{y}} = \frac{1}{2}|\langle J_{\mathsf{z}} \rangle|$, where $(\mathsf{x}, \mathsf{y}, \mathsf{z})$ label the coordinate axes. (ii) The absolute expectation value of the spin in the direction of polarization, e.g. $|\langle J_{\mathsf{z}} \rangle|$, is maximum and equal to j. (iii) The spin uncertainties are equally distributed in any two orthogonal directions in the plane normal to the direction of polarization,

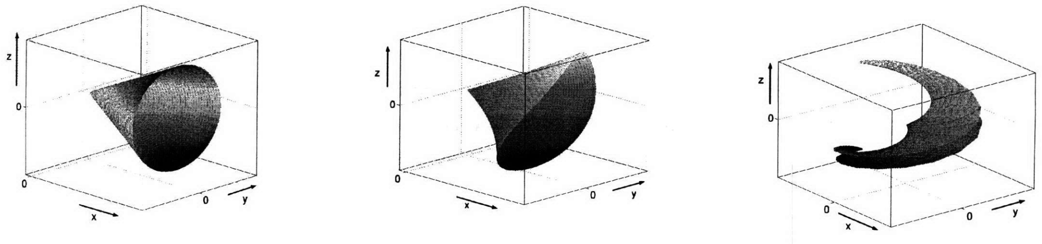

(i) (ii) (iii)

Figure 2-1: (i) A coherent state spin–j vector with expectation values $[\langle J_{\mathsf{x}}\rangle, \langle J_{\mathsf{y}}\rangle, \langle J_{\mathsf{z}}\rangle] = [1, 0, 0]$ may be visualized as a coherent superposition of angular momentum vectors on a cone about the x-axis, all with a projection of $j/2$ along that axis. (ii) After squeezing via the one-axis mechanism (see text), the cone representing the state of a spin–1 particle is elliptical, with its squeezed (minor) axis making an angle of $\pm\pi/4$ with the y, z–axes. (iii) In the maximally squeezed state of a spin–1 particle the cone has been folded into a nearly degenerate ruled surface.

e.g. $\Delta J_{\mathsf{x}} = \Delta J_{\mathsf{y}}$. Kitagawa and Ueda [25] proposed that a spin state is squeezed if the minimum spin uncertainty in the (x, y)-plane is less than the standard quantum limit of $\sqrt{j/2}$. Since a squeezed spin state (SSS) is not related to a CSS by a simple rotation, the polarization of an SSS is less than maximum, e.g. $|\langle J_{\mathsf{z}}\rangle| < j$.

To create a SSS, a "non-linear" operation must be applied, i.e. one that involves products or powers of the spin operators J_{x}, J_{y} & J_{z} in its Hamiltonian H. Kitagawa and Ueda proposed two methods for squeezing a CSS: (i) $H = J_{\mathsf{z}}^2$ (the one-axis twisting mechanism), or (ii) $H = J_{\mathsf{x}}J_{\mathsf{y}} + J_{\mathsf{y}}J_{\mathsf{x}}$ (the two-axis twisting mechanism). The second Hamiltonian can be applied directly to any CSS to squeeze it, whereas the first requires that the CSS be rotated to the (x, y)-plane before the propagator $\exp(\mathrm{i}\, kJ_{\mathsf{z}}^2)$ is used to squeeze it, where k is real number which we will call the squeezing parameter. Figure 2-1 illustrate the one-axis process for $j = 1$, in which case maximum squeezing in the (y, z)-plane is obtained when $k = \pi/2$. This one-axis method was used in the NMR experiments described below.

Table 2.1: The representation of a spin–1 by two spin–1/2 particles

Uncoupled Representation ($\|m^1 m^2\rangle$)	Coupled Representation ($\|j, m\rangle$)
$\|00\rangle = \|\uparrow\uparrow\rangle$	$\|1,1\rangle = \|\uparrow\uparrow\rangle$
$\|01\rangle = \|\uparrow\downarrow\rangle$	$\|1,0\rangle = \frac{1}{\sqrt{2}}[\|\uparrow\downarrow\rangle + \|\downarrow\uparrow\rangle]$
$\|10\rangle = \|\downarrow\uparrow\rangle$	$\|1,-1\rangle = \|\downarrow\downarrow\rangle$
$\|11\rangle = \|\downarrow\downarrow\rangle$	$\|0,0\rangle = \frac{1}{\sqrt{2}}[\|\uparrow\downarrow\rangle - \|\downarrow\uparrow\rangle]$

Table 2.2: Coupled representation ($|j, m\rangle$) of the basis states spanned by three spin–1/2 particles

Spin–3/2 subspace basis	Spin–1/2 subspace basis
$\|\frac{3}{2},\frac{3}{2}\rangle = \|\uparrow\uparrow\uparrow\rangle$	$\|\frac{1}{2},\frac{1}{2}\rangle = \frac{1}{\sqrt{6}}[2\|\uparrow\uparrow\downarrow\rangle - \|\uparrow\downarrow\uparrow\rangle - \|\downarrow\uparrow\uparrow\rangle]$
$\|\frac{3}{2},\frac{1}{2}\rangle = \frac{1}{\sqrt{3}}[\|\uparrow\uparrow\downarrow\rangle + \|\uparrow\downarrow\uparrow\rangle + \|\downarrow\uparrow\uparrow\rangle]$	$\|\frac{1}{2},-\frac{1}{2}\rangle = \frac{1}{\sqrt{6}}[\|\uparrow\downarrow\downarrow\rangle + \|\downarrow\uparrow\downarrow\rangle - 2\|\downarrow\downarrow\uparrow\rangle]$
$\|\frac{3}{2},-\frac{1}{2}\rangle = \frac{1}{\sqrt{3}}[\|\downarrow\downarrow\uparrow\rangle + \|\uparrow\downarrow\downarrow\rangle + \|\downarrow\uparrow\downarrow\rangle]$	$\|\frac{1}{2},\frac{1}{2}\rangle = \frac{1}{\sqrt{2}}[\|\uparrow\downarrow\uparrow\rangle - \|\downarrow\uparrow\uparrow\rangle]$
$\|\frac{3}{2},-\frac{3}{2}\rangle = \|\downarrow\downarrow\downarrow\rangle$	$\|\frac{1}{2},-\frac{1}{2}\rangle = \frac{1}{\sqrt{2}}[\|\uparrow\downarrow\downarrow\rangle - \|\downarrow\uparrow\downarrow\rangle]$

A system of two spin–1/2 particles has 4 basis states. In the coupled representation (in Table 2.1), the three symmetric states span a subspace that transforms under identical rotations of both spins like a single spin–1. Similarly, a system of three spin–1/2 particles has 8 basis states, which span a symmetric subspace that transforms like a single spin–3/2, as well as two spin–1/2 subspaces with lower symmetry. The four states listed on the left-hand column of Table 2.2 are the coupled representation of the spin–3/2 subspace.

From the uncoupled and coupled representations, we see that there is a linear mapping from the spin–j subspaces into the combined $2j$ spin–1/2 systems. These mappings induce the mappings between the spin–j operators and products of spin–1/2 operators (denoted here by $I^{\mathsf{spin}}_{\mathsf{axis}}$), which for $j = 1$ is simply

$$J_{\mathsf{x}} = I^1_{\mathsf{x}} + I^2_{\mathsf{x}}, \quad J_{\mathsf{y}} = I^1_{\mathsf{y}} + I^2_{\mathsf{y}}, \quad J_{\mathsf{z}} = I^1_{\mathsf{z}} + I^2_{\mathsf{z}}. \tag{2.1}$$

For $j = 3/2$, on the other hand, we obtain

$$\begin{aligned}
J_\mathrm{x} &= I^1_\mathrm{x} I^2_\mathrm{x} I^3_\mathrm{x} \left(2 + \tfrac{2}{3}(I^1_\mathrm{x} I^2_\mathrm{x} + I^1_\mathrm{x} I^3_\mathrm{x} + I^2_\mathrm{x} I^3_\mathrm{x}) - \tfrac{8}{3}(\boldsymbol{I}^1 \cdot \boldsymbol{I}^2 + \boldsymbol{I}^1 \cdot \boldsymbol{I}^3 + \boldsymbol{I}^2 \cdot \boldsymbol{I}^3)\right) \\
J_\mathrm{y} &= I^1_\mathrm{y} I^2_\mathrm{y} I^3_\mathrm{y} \left(2 + \tfrac{2}{3}(I^1_\mathrm{y} I^2_\mathrm{y} + I^1_\mathrm{y} I^3_\mathrm{y} + I^2_\mathrm{y} I^3_\mathrm{y}) - \tfrac{8}{3}(\boldsymbol{I}^1 \cdot \boldsymbol{I}^2 + \boldsymbol{I}^1 \cdot \boldsymbol{I}^3 + \boldsymbol{I}^2 \cdot \boldsymbol{I}^3)\right) \quad (2.2) \\
J_\mathrm{z} &= I^1_\mathrm{z} I^2_\mathrm{z} I^3_\mathrm{z} \left(2 + \tfrac{2}{3}(I^1_\mathrm{z} I^2_\mathrm{z} + I^1_\mathrm{z} I^3_\mathrm{z} + I^2_\mathrm{z} I^3_\mathrm{z}) - \tfrac{8}{3}(\boldsymbol{I}^1 \cdot \boldsymbol{I}^2 + \boldsymbol{I}^1 \cdot \boldsymbol{I}^3 + \boldsymbol{I}^2 \cdot \boldsymbol{I}^3)\right)
\end{aligned}$$

Given the apparent complexity of implementing these operations, it was decided instead to implement the far simpler analoges of Eq. (2.2), namely:

$$\tilde{J}_\mathrm{x} \;=\; I^1_\mathrm{x} + I^2_\mathrm{x} + I^3_\mathrm{x} \,, \quad \tilde{J}_\mathrm{y} \;=\; I^1_\mathrm{y} + I^2_\mathrm{y} + I^3_\mathrm{y} \,, \quad \tilde{J}_\mathrm{z} \;=\; I^1_\mathrm{z} + I^2_\mathrm{z} + I^3_\mathrm{z} \,. \tag{2.3}$$

It is easily shown that J_x, J_y, and J_z are contained within the algebra generated by $\tilde{J}_\mathrm{x}$, $\tilde{J}_\mathrm{y}$, and $\tilde{J}_\mathrm{z}$, and that the latter satisfy the usual angular momentum commutation relations. In fact, since they have two extra pairs of identical eigenvalues $\pm 1/2$, they are the sum of the angular momentum operators for a spin–3/2 mixed with those for a pair of spin–1/2. As a result, it was not possible to squeeze the corresponding coherent states to the amount that would have been possible if a pure spin–3/2 representation had been used.

It is apparent that for $j = 1$, $\exp(-\mathrm{i}\, k J_\mathrm{z}^2)$ is an evolution $\exp(-\mathrm{i}\, k\, 4 I^1_\mathrm{z} I^2_\mathrm{z})$ under the bilinear Hamiltonian associated with the scalar coupling interaction between spins in NMR, up to an overall phase factor. Thus the traceless part of the pseudopure state as a function of the squeezing parameter, and its spin–1 pure state equivalent, are

$$\begin{aligned}
e^{-\mathrm{i}k\,4 I^1_\mathrm{z} I^2_\mathrm{z}}\left(\tfrac{1}{2} I^1_\mathrm{x} + \tfrac{1}{2} I^2_\mathrm{x} + I^1_\mathrm{x} I^2_\mathrm{x}\right) e^{\mathrm{i}k\,4 I^1_\mathrm{z} I^2_\mathrm{z}} &= \cos(k)\left(\tfrac{1}{2} I^1_\mathrm{x} + \tfrac{1}{2} I^2_\mathrm{x} + I^1_\mathrm{x} I^2_\mathrm{x}\right) - \sin(k)\left(I^1_\mathrm{y} I^2_\mathrm{z} + I^1_\mathrm{z} I^2_\mathrm{y}\right) \\
\Leftrightarrow\; e^{-\mathrm{i}kJ_\mathrm{z}^2}\, \tfrac{1}{2}\left(J_\mathrm{x} + J_\mathrm{x}^2\right) e^{\mathrm{i}kJ_\mathrm{z}^2} &= \cos(k)\, \tfrac{1}{2} J_\mathrm{x} + \tfrac{1}{2} J_\mathrm{x}^2 - \mathrm{i}\, \sin(k)\, \tfrac{1}{2}\left[J_\mathrm{x},\, J_\mathrm{z}^2\right] \,, \qquad (2.4)
\end{aligned}$$

where $[\,,]$ is the commutator.

For $j = 3/2$, on the other hand, we find that

$$\begin{aligned} J_{\mathsf{z}}^2 &= \tfrac{5}{8} I_8 + \tfrac{1}{6}\big(\boldsymbol{I}^1 \cdot \boldsymbol{I}^2 + \boldsymbol{I}^1 \cdot \boldsymbol{I}^3 + \boldsymbol{I}^2 \cdot \boldsymbol{I}^3\big) + 2\big(I_{\mathsf{z}}^1 I_{\mathsf{z}}^2 + I_{\mathsf{z}}^1 I_{\mathsf{z}}^3 + I_{\mathsf{z}}^2 I_{\mathsf{z}}^3\big), \\ &= \tilde{J}_{\mathsf{z}}^2 + \tfrac{1}{6}\big(\boldsymbol{I}^1 \cdot \boldsymbol{I}^2 + \boldsymbol{I}^1 \cdot \boldsymbol{I}^3 + \boldsymbol{I}^2 \cdot \boldsymbol{I}^3 - \tfrac{3}{4} I_8\big)\,. \end{aligned} \tag{2.5}$$

It follows that $\exp(-\mathrm{i}\,k J_{\mathsf{z}}^2)$ is, to a fairly good approximation, the same as three equal scalar coupling evolutions up to phase, and the (pure) state as a function of the squeezing parameter becomes

$$\begin{aligned} & e^{-\mathrm{i}k\,4(I_{\mathsf{z}}^1 I_{\mathsf{z}}^2 + I_{\mathsf{z}}^1 I_{\mathsf{z}}^3 + I_{\mathsf{z}}^2 I_{\mathsf{z}}^3)}\tfrac{1}{2}\big(I_8 + 2I_{\mathsf{x}}^1\big)\tfrac{1}{2}\big(I_8 + 2I_{\mathsf{x}}^2\big)\tfrac{1}{2}\big(I_8 + 2I_{\mathsf{x}}^3\big)e^{\mathrm{i}k\,4(I_{\mathsf{z}}^1 I_{\mathsf{z}}^2 + I_{\mathsf{z}}^1 I_{\mathsf{z}}^3 + I_{\mathsf{z}}^2 I_{\mathsf{z}}^3)} \\ = \;& \tfrac{1}{2}\big(I_8 + I_{\mathsf{x}}^1(I_8 - 4I_{\mathsf{z}}^2 I_{\mathsf{z}}^3) + \cos(2k) I_{\mathsf{x}}^1(I_8 + 4I_{\mathsf{z}}^2 I_{\mathsf{z}}^3) - \sin(2k)\, I_{\mathsf{y}}^1(I_{\mathsf{z}}^2 + I_{\mathsf{z}}^3)\big) \;\cdots \\ & \tfrac{1}{2}\big(I_8 + I_{\mathsf{x}}^2(I_8 - 4I_{\mathsf{z}}^1 I_{\mathsf{z}}^3) + \cos(2k) I_{\mathsf{x}}^2(I_8 + 4I_{\mathsf{z}}^1 I_{\mathsf{z}}^3) - \sin(2k)\, I_{\mathsf{y}}^2(I_{\mathsf{z}}^1 + I_{\mathsf{z}}^3)\big) \;\cdots \\ & \tfrac{1}{2}\big(I_8 + I_{\mathsf{x}}^3(I_8 - 4I_{\mathsf{z}}^1 I_{\mathsf{z}}^2) + \cos(2k) I_{\mathsf{x}}^3(I_8 + 4I_{\mathsf{z}}^1 I_{\mathsf{z}}^2) - \sin(2k)\, I_{\mathsf{y}}^3(I_{\mathsf{z}}^1 + I_{\mathsf{z}}^2)\big) \\ \leftrightarrow \;& \tfrac{1}{16}\big(e^{-\mathrm{i}k/4}(18 - J_{\mathsf{z}}^2) + e^{-\mathrm{i}k\,9/4}(2 - J_{\mathsf{z}}^2)\big) \;\cdots \\ & \qquad \tfrac{1}{48}\big(- 3I_8 - 2J_{\mathsf{x}} + 12J_{\mathsf{x}}^2 + 8J_{\mathsf{x}}^3\big)\tfrac{1}{16}\big(e^{\mathrm{i}k/4}(18 - J_{\mathsf{z}}^2) + e^{\mathrm{i}k\,9/4}(2 - J_{\mathsf{z}}^2)\big)\,, \end{aligned} \tag{2.6}$$

where in the last line we have expanded both the exponential $\exp(-\mathrm{i}k\, J_{\mathsf{z}}^2)$ and the initial coherent state along x in terms of angular momentum operators. Finally, the CSS $|0\rangle$ is, for both values of j, the same as the Zeeman ground state $|\uparrow\uparrow\rangle$ or $|\uparrow\uparrow\uparrow\rangle$ in the uncoupled representation.

2.3 The NMR implementation of squeezed spin states

The implementation of spin squeezing was carried out on a liquid-state NMR quantum information processor, using the two spin–1/2 hydrogen nuclei of 2,3-dibromothiophene (see Fig. 2-2) to represent the spin–1 system, while the spin–3/2 system was represented using the three carbon atoms of a ^{13}C-labeled sample of alanine (see Fig. 2-3). Both the experiments were carried out on a Bruker AVANCE-400 spectrometer in a field of ca. 9.4 Tesla. In the case of the two-spin experiment, frequency-selective pulses were used to rotate single spins, and hard π-pulses to refocus unwanted chemical shifts. To compensate for pulse imperfections, composite pulses were employed instead of the standard π-pulse [35]. In the three-spin experiment, strongly modulating pulses were used to more accurately perform the desired unitary operations [21, 31]. Unlike low-power "soft" pulses, these pulses average out unwanted evolution, are shorter in time and hence also reduce relaxation effects.

The $I_z^1 I_z^2$ operator used to squeeze the spin–1 system was implemented using π-pulses to refocus the Zeeman evolution of the spins while allowing the scalar coupling between them to evolve, in the standard fashion [22]. Because the coupling between spins 1 and 3 of the alanine system is so small ($J^{13} = -1.29$ Hz), the coupling between them was generated out of the much stronger $1,2$ and $2,3$ couplings [41]. The sum of the three scalar coupling terms of the form $I_z^\ell I_z^m$ was taken as an approximation to J_z^2 in the spin–3/2, as described in Eq. (2.5). As usual in NMR quantum information processing [23, 27], pseudo-pure states were used to represent the dynamics of pure states. These were obtained using spatial averaging techniques based on magnetic field gradients [32, 39].

Even though the decoherence times in liquid-state NMR are long, the intrinsic decoherence rates of the spins still impose limits on the accuracy of the experimental results. The T_2 relaxation rates in $2,3$-dibromo-thiophene were 3.2 s^{-1} for both of the hydrogen spins, while in alanine these rates were 0.55, 0.42 and 0.80 s^{-1} for the C^1, C^2 and C^3 spins, respectively. The products of the shortest of these decoherence times, multiplied by the weakest coupling constant used, were better than 15 for both $2,3$-dibromo-thiophene and alanine, which allows about 30 c-NOT gates before decoherence begins to seriously degrades the quality of the results. The amount of time needed for the longest experiments reported here was only about one third of this.

The accuracy of the experiments is further affected by systematic errors like imperfect calibration of the pulses, off-resonance effects and RF inhomogeneity [22]. The effects

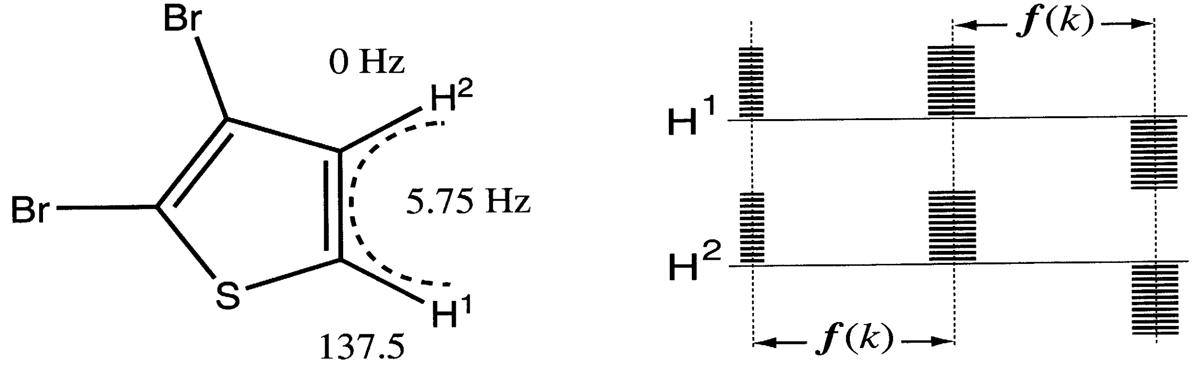

Figure 2-2: The molecular structure of 2,3-dibromo-thiophene is shown on the left, with the two hydrogen atoms used for the spin–1 simulations numbered as in the main text. The coupling strength J between them and the chemical shift of the first compared to the second are also shown. The diagram on the right shows the pulse sequence used to implement spin squeezing for a given parameter k, where $f(k) \equiv k/(2\pi J)$, narrow rectangles indicate $\pi/2$ y-rotations, the broad rectangles y-rotations by π, and the rectangles point downwards for pulses effecting rotations by the negatives of these angles.

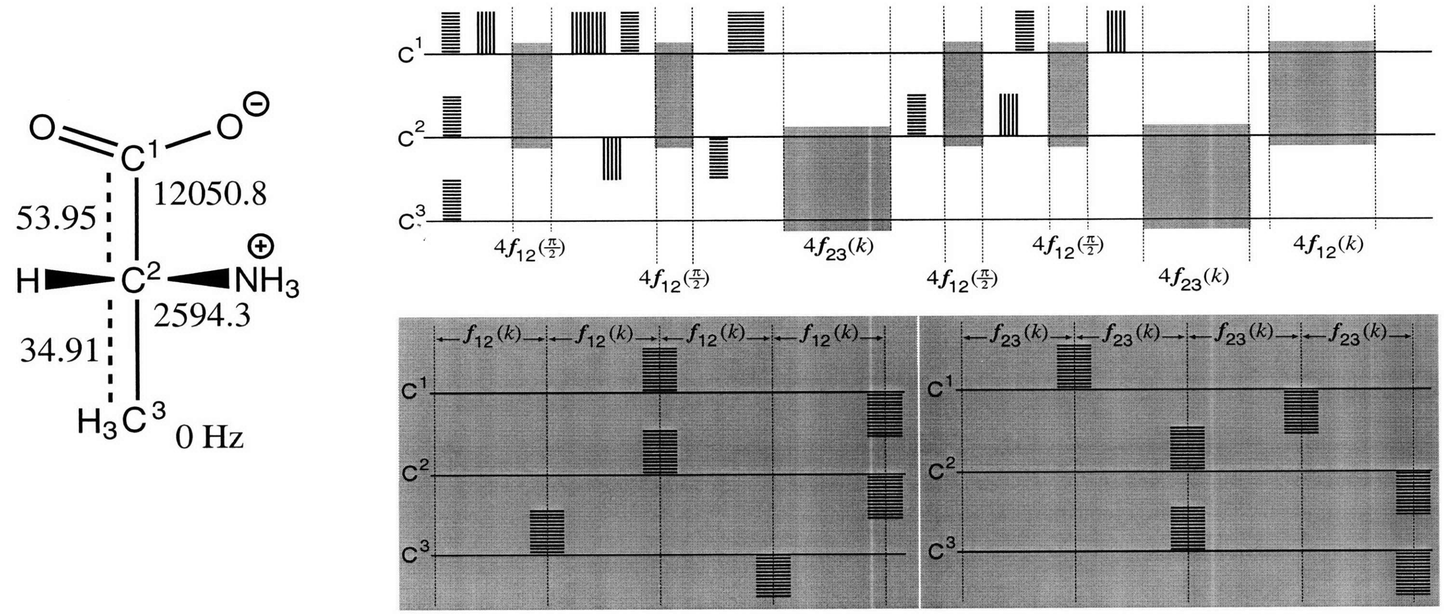
O
C1
O
12050.8
53.95
H
C2
NH3
2594.3
34.91
H3C3
0 Hz
C1
C2
C3
4f12(π/2)
4f12(π/2)
4f23(k)
4f12(π/2)
4f12(π/2)
4f23(k)
4f12(k)
f12(k)
f12(k)
f12(k)
f12(k)
f23(k)
f23(k)
f23(k)
f23(k)

Figure 2-3: The molecular structure alanine is shown on the left, with the three carbon-13 atoms used for the experiments numbered as in the text. The numbers next to the dashed lines are the corresponding coupling constants (in Hz), while the numbers next to the carbons are their chemical shifts relative to the third (in Hz). On the top right is a schematic diagram of the pulse sequence used, where the horizontal striping indicates an y-pulse, vertical striping an x-pulse, the narrower pulses induce rotations by $\pi/2$, and the wider ones by π (or the negatives thereof if the pulse is below the spin's line). The grey boxes indicate one of the two "modules" show on the bottom right, which allow a $I_z^m I_z^n$ evolution by the angle (k or $\pi/2$) shown on the bottom of the pulse sequence diagram while refocussing the chemical shifts and the coupling between the pairs not contained in the grey box. The functions which relate the delay time to the squeezing parameter k is given by $f_{mn}(k) \equiv k/(4\pi J^{mn})$ for $[m, n] = [1, 2], [2, 3]$.

of these errors may be seen in the density matrices of the final states, which in turn were determined by full state tomography [30]. Although plots of these density matrices (see Figs. 2-4 and 2-5) provide a visual overview of the results, a more quantitative summary of the overall accuracy may be obtained by calculating the correlation between the theoretically expected and experimentally determined density matrices ρ_{the} and ρ_{fin}, respectively. This is defined as

$$C = \frac{tr(\rho_{\mathsf{fin}}\rho_{\mathsf{the}})}{\sqrt{tr(\rho_{\mathsf{fin}}\rho_{\mathsf{fin}})tr(\rho_{\mathsf{the}}\rho_{\mathsf{the}})}} . \tag{2.7}$$

To also include an estimate of the precision of the experiment, the amount of signal (or polarization) lost during the experiment must also be taken into account. This leads to a metric called the attenuated correlation [21], namely

$$C_{\mathsf{att}} = C\,\frac{\sqrt{tr(\rho_{\mathsf{fin}}\rho_{\mathsf{fin}})}}{\sqrt{tr(\rho_{\mathsf{ini}}\rho_{\mathsf{ini}})}} = \frac{tr(\rho_{\mathsf{fin}}\rho_{\mathsf{the}})}{\sqrt{tr(\rho_{\mathsf{ini}}\rho_{\mathsf{ini}})tr(\rho_{\mathsf{the}}\rho_{\mathsf{the}})}} . \tag{2.8}$$

The theoretically expected density matrix ρ_{the} was obtained by applying the intended unitary transformation U_{the} to the initial pseudo-pure state ρ_{ini}, as determined by state tomography.

2.4 Results of spin squeezing experiments

Using state tomography [30], the $2j$ spin–1/2 density matrices ρ_{exp} were reconstructed following squeezed state preparation for various values of the squeezing parameter $k = 0, \ldots, \pi$. The expectation values and uncertainties along the basis axes were then calculated directly from these density matrices and the J_μ (or approximate $\tilde{J}_\mu$ matrices given in Eqs. (2.1) and (2.3)), as follows:

$$\begin{aligned} \langle J_\mu \rangle &= tr(J_\mu \rho_{\mathsf{exp}}) \,; \\ \langle \Delta \mathbf{J}_\mu \rangle &= \sqrt{tr(J_\mu^2 \rho_{\mathsf{exp}}) - (tr(J_\mu \rho_{\mathsf{exp}}))^2} \,. \end{aligned} \tag{2.9}$$

where $\mu = \mathsf{x}, \mathsf{y}, \mathsf{z}$.

The correlation for the spin–1 pseudo-pure density matrix (see Fig. 2-4(i)) was 0.99. For the density matrix corresponding to the maximally squeezed ($k = \pi/2$) spin–1 state, the correlation and the attenuated correlation were 0.99 and 0.98 respectively. The correlation for the spin–3/2 pseudo-pure state density matrix (see Fig. 2-5(i)) was 0.98, while the correlation and the attenuated correlation of the maximally squeezed spin–3/2 state were 0.84 and 0.80, respectively.

Since the squeezing operator conserves the total angular momentum, the combined $2j$ spin–1/2 system should stay in the spin–j subspace during the course of the experiment. However, due to decoherence and other errors in the implementation there is some "leakage" out of the effective spin–j subspace. To quantify the accuracy with which we have been able to simulate the spin–j system, we computed the best pseudo-pure-state approximation to mixed-state density matrix ρ_{exp}, by taking the eigenvector $|\psi_{\mathsf{max}}\rangle$ associated with the largest eigenvalue of ρ_{exp}. The probability of leakage was then obtained from the definition

$$Pr_{\mathsf{leak}} = 1 - \sum_{m=-j}^{j} \left|\langle j, m \,|\, \psi_{\mathsf{max}}\rangle\right|^2 , \tag{2.10}$$

where $|j, m\rangle$ are the basis states of spin–j subspace. This probability of leakage, averaged over all the experiments performed, was (0.02 ± 0.02)% for the spin-1 simulations and (7.67 ± 3.20)% for the spin–3/2. The substantially larger leakage in the latter case was due to the fact that the protons were not decoupled from the carbons during the carbon scalar coupling evolution delays, in order to avoid the possibility of carbon-proton nuclear Overhauser effects.

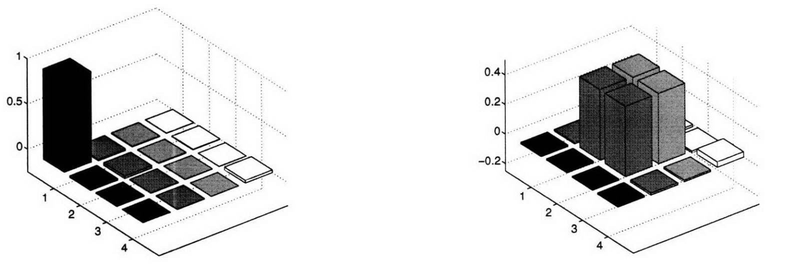

(i) (ii)

Figure 2-4: (i) The real part of the experimental density matrix representing the initial pseudo-pure state $|00\rangle$ for the spin–1 experiments.
(ii) The real part of the experimental density matrix representing the maximally squeezed state of the effective spin–1 particle.

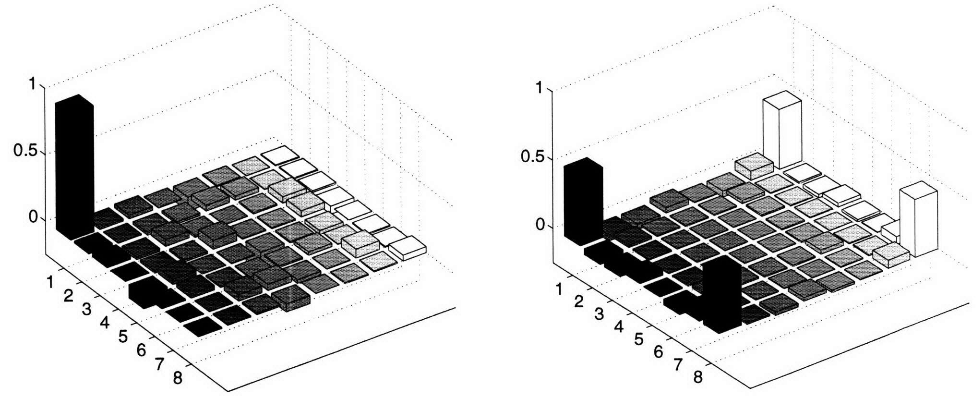

(i) (ii)

Figure 2-5: (i) The real part of the experimental density matrix representing the initial pseudo-pure state $|000\rangle$ for the spin–3/2 experiments.
(ii) The real part of the density matrix when the squeezing parameter $k = \pi/2$, at which point a GHZ state is obtained [28].

2.4.1 The spin-1 case

The initial pseudo-pure state corresponds to a coherent state of the embedded spin–1 subspace. It remains in a coherent spin state after a $\frac{\pi}{2}$ rotation to the x-axis and accordingly, state tomography at this point reveals that $\langle \mathrm{J_x} \rangle$ is nearly equal to 1 while the spin uncertainties in the y and z-directions are nearly equal to $1/\sqrt{2}$. After applying the non-linear interaction for a period of $2f(k) = k/(\pi J)$, the spin–1 expectation values in all directions are all close to 0, consistent with a maximally entangled state (see Table 2.3). The uncertainty is now maximum in the x-direction, while the uncertainties in the y and z-directions are still nearly equal to $1/\sqrt{2}$ because the principle axes of the squeezed ellipsoid are at $\pi/4$ to the y and z axes (see Fig. 2-1(iii)). To make the squeezing more readily apparent, it was convenient to follow the squeezing step by a $\pi/4$ x-pulse so that the uncertainty along the z-axis becomes 1. The experimental and theoretical data for this maximally squeezed and rotated state are given in Table 2.3.

Table 2.3: Theoretical and experimental spin expectation values and uncertainties of the maximally squeezed spin–1 states

	$\langle \mathrm{J_x} \rangle$	$\langle \mathrm{J_y} \rangle$	$\langle \mathrm{J_z} \rangle$	$\langle \Delta\mathrm{J_x} \rangle$	$\langle \Delta\mathrm{J_y} \rangle$	$\langle \Delta\mathrm{J_z} \rangle$
Theory	0.00	0.00	0.00	1.00	0.00	1.00
Experiment	0.00	−0.02	0.00	0.97	0.21	0.98

The variation of $|\langle J_\mathrm{x} \rangle|$, ΔJ_y and ΔJ_z for different values of k is plotted in Fig. 2-6. The corresponding values of $|\langle J_\mathrm{y} \rangle|$ and $|\langle J_\mathrm{z} \rangle|$ are close to zero implying that the spin system is polarized along x direction for all values of the squeezing parameter k.

2.4.2 The spin–3/2 case

After the initial $\pi/2$ rotation to the x-axis, state tomography showed that the spin–3/2 angular momentum vector pointed in the x-direction with $\langle \mathrm{J_x} \rangle \approx 1.5$, and uncertainties in the y and z-directions nearly equal to their theoretical values of $\sqrt{3}/2$.

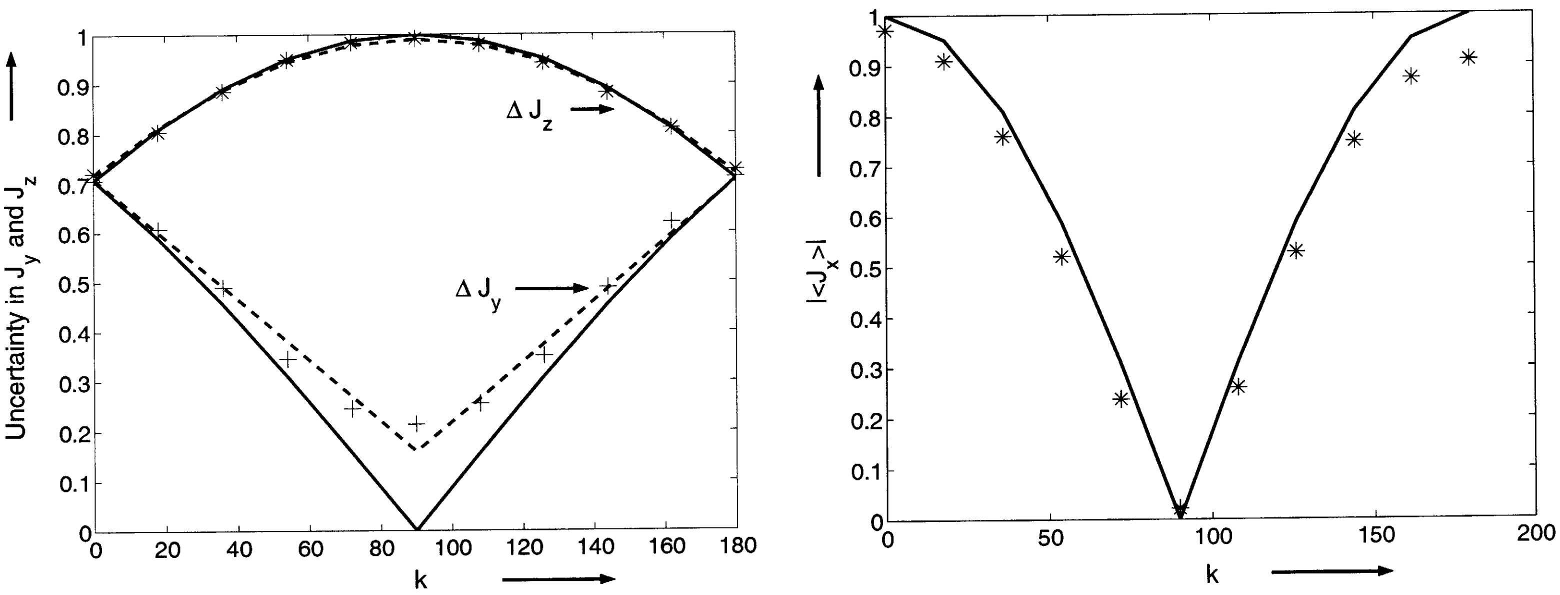

(i)

(ii)

Figure 2-6: Plots of the theoretically expected uncertainties as a function of the squeezing parameter k (in degrees) for spin–1 (solid lines), along with the fits (dashed lines) to the uncertainties computed from the experimental density matrices (+ or $*$). (i) Plots of $\langle \Delta \mathbf{J}_y \rangle$ (lower curves), and $\langle \Delta \mathbf{J}_z \rangle$ with k (upper curves). (ii) Plot of $|\langle \mathbf{J}_x \rangle|$ (no fits shown).

Table 2.4: Theoretical and experimental spin expectation values and uncertainties of the maximally squeezed spin–3/2 states

	$\langle \mathbf{J}_x \rangle$	$\langle \mathbf{J}_y \rangle$	$\langle \mathbf{J}_z \rangle$	$\langle \Delta\mathbf{J}_x \rangle$	$\langle \Delta\mathbf{J}_y \rangle$	$\langle \Delta\mathbf{J}_z \rangle$
Theory	1.00	0.00	0.00	0.87	0.50	1.32
Experiment	0.82	0.05	−0.13	0.92	0.53	1.36

Application of the non-linear interaction for a given k created some apparent entanglement in the system, as indicated by the fact that $\langle \mathbf{J}_x \rangle$ was reduced to about 1 while $\langle \mathbf{J}_y \rangle$ and $\langle \mathbf{J}_z \rangle$ remained zero. The uncertainty in the x-direction also increased from 0 to $\sqrt{3}/2$. To orient the axes of the squeezed uncertainty ellipsoid along the y and z-directions, the results of state tomography were rotated about the x-axis (on a computer, since unlike the spin–1 case the rotation angle needed depends on the value of k [25]). The experimental and theoretical data for the maximally squeezed state are shown in Table 2.4, while the variation of $|\langle J_x \rangle|$, ΔJ_y and ΔJ_z for different values of k is plotted in Fig. 2-7. As in the spin–1 case, the corresponding values of $|\langle J_y \rangle|$ and $|\langle J_z \rangle|$ are close to zero, implying that the spin system is polarized along x-direction for all values of the squeezing parameter k, as desired.

2.4.3 Behavior of entanglement measures

The probability of leakage measurements described above (see Eq. (2.10)) show that the best pseudo-pure-state approximation to the final mixed-state density matrix quite accurately describes the spin–j system. Thus this pseudo-pure state may be used to study the entanglement of the constituent spin–1/2 particles by well-understood pure-state entanglement criteria. The criteria used here are the entanglement of formation [16] (or, for bipartite pure states, the von Neumann entropy of the partial trace over either subsystem), and the concurrence [24, 46] of (the partial trace onto any) pair of qubits. The purpose of this discussion is not to uncover any new features of entanglement in these simple systems, but rather to use the compatibility of the experimental results with the well-known behavior of these entanglement measures as

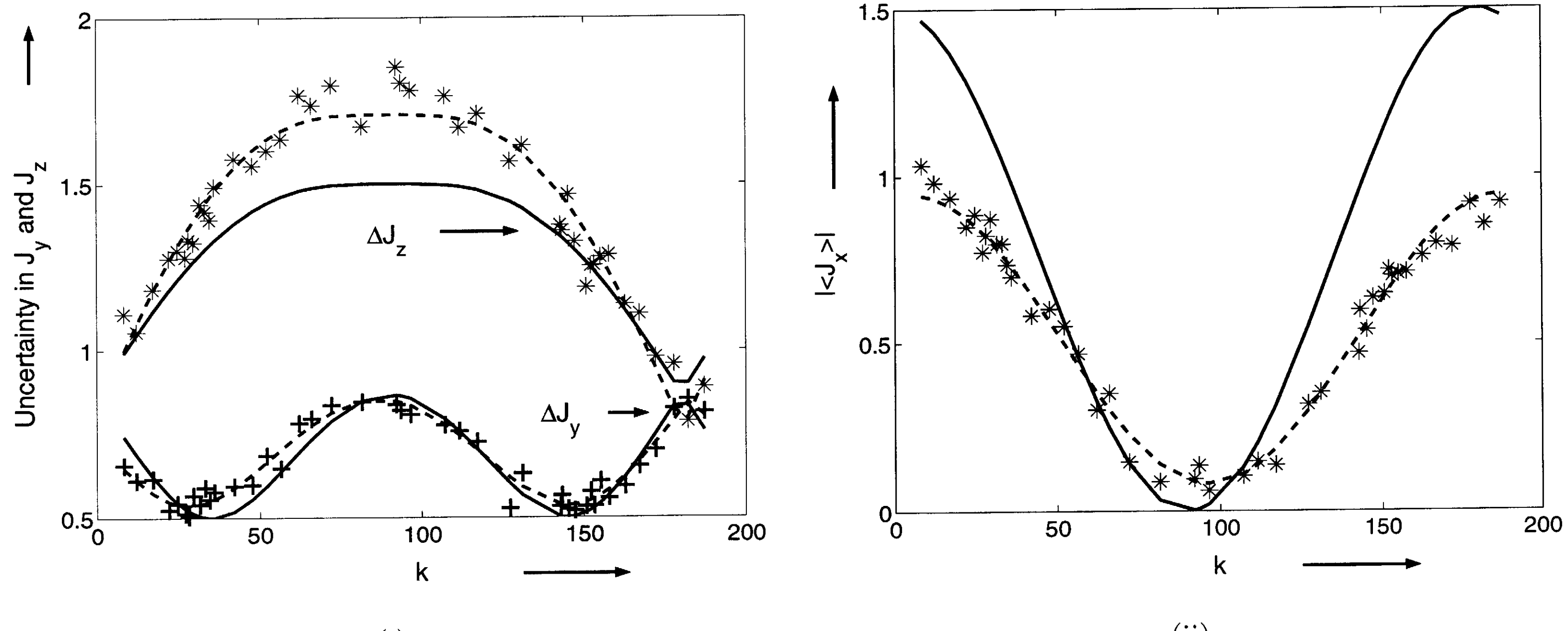

(i) (ii)

Figure 2-7: Plots of the theoretically expected uncertainties as a function of the squeezing parameter k (in degrees) for spin–3/2 (solid lines), along with fits (dashed lines) to the uncertainties computed from the experimental density matrices (+ or $*$). (i) Plots of $\langle \Delta \mathbf{J}_y \rangle$ (lower curves) and $\langle \Delta \mathbf{J}_z \rangle$ (upper curves). (ii) Plot of $|\langle \mathbf{J}_x \rangle|$.

a benchmark for the precision of control obtained. In addition, these entanglement measures were computed without taking into account the very large identity component that is always represent in liquid-state NMR, and hence should be regarded as measures of the "pseudo-entanglement" associated with the pseudo-pure states used for the experiments.

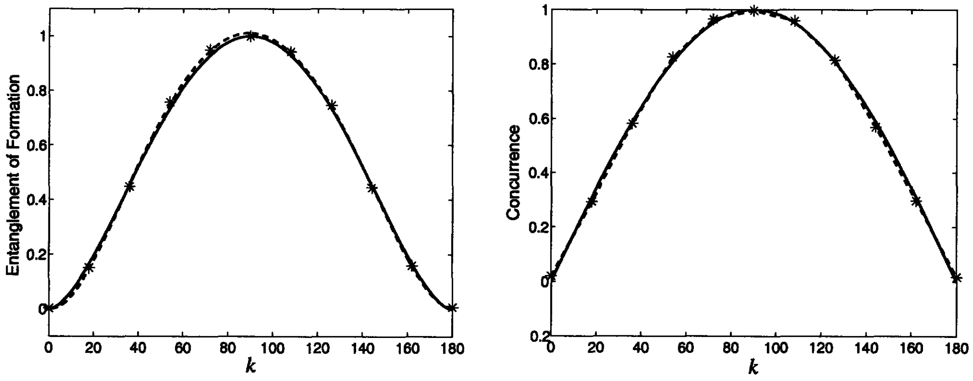

(i) (ii)

Figure 2-8: Plots of the entanglement of formation (i) and concurrence (ii) with the squeezing parameter k (in degrees) for spin–1. The solid lines are the theoretically expected curves, while the dashed lines interpolate linearly between the values computed from the experimental density matrices ($*$) obtained via tomography.

Figure 2-8 shows plots of the theoretically expected and experimentally observed entanglement measures as a function of the squeezing parameter k for the spin–1 experiments. It is immediately apparent that the theory and experiments agree extremely well with respect to either entanglement measure, in accord with the fact that the concurrence and entanglement of formation are monotonically related for two qubits. The maximally squeezed state ($k = 90°$) is observed to correspond to the maximally entangled state, as theory predicts it should in a representation by Dicke states [40].

Figure 2-9 shows the analogous pair of plots for the spin–3/2 experiments, where the interpolation is now done using a fifth-order polynomial fit to the data (dashed lines). In this case three different entanglements of formation are obtained, depending on

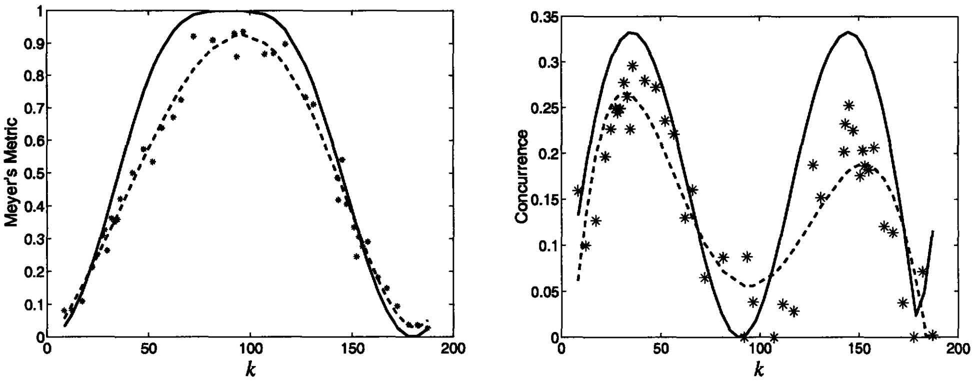

(i) (ii)

Figure 2-9: Plots of the Meyer's metric or average entanglement after tracing down to a single qubit (i) and concurrence after tracing down to any pair of qubits (ii) with the squeezing parameter k (in degrees) for spin–3/2. The solid lines are the theoretically expected curves, while the dashed lines are a fifth-order polyomial fit to the values computed from the experimental density matrices ($*$) obtained via tomography.

which pair of qubits is traced over in order to obtain the reduced density matrix, and their average, also known as the Meyer's entanglement metric[29], is plotted for simplicity. According to this metric, the maximum entanglement again occurs at $k = 90°$ and corresponds to a Greenberger-Horne-Zeilinger state, which is however not a maximally squeezed state. The maximally squeezed state now occurs instead at $k = 34.7°$ and again at $180 - 34.7 = 155.3°$, and corresponds to the maximum concurrence of the reduced density matrix obtained by tracing over any one qubit (which is attained by a W-state). The correspondence between theory and experiment in this case is noticeably lower than in the spin–1 experiments, primarily because of leakage from the carbons used as qubits into the alpha and methyl protons during the experiment.

2.5 Conclusions

We have demonstrated the use of liquid-state NMR to simulate squeezed states of the effective spin–1 and 3/2 subsystem contained in a two and three-qubit system, respectively. We have further shown that the precision of quantum control obtained was sufficient to reproduce the theoretically expected behavior of the spin–1 and 3/2 observables as well as the associated entanglement measures among the underlying qubits. The results are a further demonstration of the utility of pseudo-pure states [23], and the power of strongly modulating pulses [31], for the development and validation of quantum control methods. The dynamics of the coherences among the fiducial states that were confirmed by complete tomography are fully in accord with these proposals, even though the highly mixed states used in our experiments were, of course, separable at all times. It is interesting to observe, however, that even when the identity component of the density matrix is fully taken into account the uncertainties in the x and y directions were unequal, i.e. the actual mixed states created could be regarded as (very slightly) "squeezed".

It should also be pointed out that the interpretation of the higher spin states as "squeezed" or not depends on how the higher spin states are mapped into the symmetric subspace of the multi-spin–1/2 system. We discussed earlier, for example, how the mapping used here for the spin–3/2 experiments actually gave the sum of a spin–3/2 with a spin–1/2 pair, limiting the degree of squeezing attainable. Even when the mathematical representation is strictly correct, however, the physical properties of the squeezed states can be rather different. For instance, if we were to replace the Dicke states $|\uparrow\uparrow\rangle$ and $|\downarrow\downarrow\rangle$ in Table 2.1 by the Bell states $1/\sqrt{2}\,(|\uparrow\uparrow\rangle \pm |\downarrow\downarrow\rangle)$, the maximally squeezed state of the simulated spin–1 would correspond to the unentangled basis state $|00\rangle$ of the two-qubit system in which it is contained. Such a representation may be a bit unnatural, since rotations of the qubits no longer correspond to rotations of the higher spin, but should still be kept in mind when discussing the relations between entanglement in multi-qubit systems and the squeezing of the effective higher spins therein [18, 25].

CHAPTER 3

SELECTIVE COHERENCE TRANSFERS IN HOMONUCLEAR DIPOLAR COUPLED SPIN SYSTEMS

3.1 Introduction

Nuclear spins feature prominently in most proposals for solid state quantum information processors. They have the advantage of a simple and well defined energy level structure and they are normally well isolated from other degrees of freedom. The challenge of using nuclear spins in solids is to obtain control over the multi-spin dynamics. In a dielectric solid, the dominant interaction between the spins is the magnetic dipolar coupling. Since the strength of the coupling between two spins is inversely proportional to the cube of the distance between them, a single spin is coupled to a large number of surrounding spins, and not just its immediate neighbors. Therefore every desired gate is embedded in a complex, multi-body space and the dynamics have so far proven to be intractable. Controlling the evolution of a dipolar coupled spin system has long been an important goal in solid state NMR, particularly for spectroscopic studies. For example, the dipolar coupling has been effectively

---

[2] Parts of this chapter were extracted from the paper "Selective coherence transfers in homonuclear dipolar coupled spin systems", by C. Ramanathan, S. Sinha, J. Baugh, T. F. Havel and D. G. Cory, *Physical Review A, Vol. 71, 020303(R), February 2005.*

turned off using techniques such as spinning the sample rapidly at the magic angle ($\theta_m = \cos^{-1}(1/\sqrt{3})$) and a variety of multiple pulse techniques, which average the spatial and spin tensors of the coupling respectively, as well as a combination of these [50, 51].

A very useful element of control would be to map the physical dipolar Hamiltonian of the spin system onto an effective interaction that has the form of only nearest neighbor couplings. This would significantly simplify the implementation of accurate two-qubit operations in a many-qubit solid state spin-based quantum processor [6, 47, 48, 8]. This restricted evolution is also necessary to avoid cross-talk between adjacent solid state quantum information processors in ensemble quantum computation [4, 5]. Without such control the gate fidelities achievable within a given processor element will be degraded due to leakage to other members of the ensemble. Nearest neighbor mapping would also allow quantum simulations of many-body systems such as the Ising, XY or Heisenberg Hamiltonians in 1, 2 or 3 dimensions. The mapping envisioned here would have significant applications beyond quantum information processing. For example, a nearest neighbor interaction could allow a more accurate determination of distances in NMR structural studies, and could be used to perform sequential polarization transfers, such as along the backbone of a protein.

Here we report the first step towards the experimental realization of such a scheme for the special case of an ensemble of spin pairs, where the dipolar coupling between the spins within a pair is significantly larger than the coupling between spins on neighboring pairs. We are able to extend the phase memory of the spin pairs by decoupling the pairs from each other, without decoupling the interaction between spins within a pair. The control sequence consists of a simple amplitude modulated RF field, with the modulation frequency set to the desired dipolar coupling strength.

3.2 Theory of the modulation scheme

Our model system is an assembly of identical spin pairs with (strong) dipolar coupling ω_D^S and weaker couplings between spins on different pairs. In a strong external magnetic field aligned along $\hat{z}$ the truncated secular dipolar Hamiltonian for this system is given by

$$H_d = \frac{\hbar}{4}\sum_i \omega_D^S h_{12}^{ii} + \frac{\hbar}{4}\sum_{\alpha,\beta=1}^{2}\sum_{i\neq j}\omega_D^{ij\alpha\beta} h_{\alpha\beta}^{ij} \tag{3.1}$$

where $h_{\alpha\beta}^{ij} = 2\sigma_{zi}^{\alpha}\sigma_{zj}^{\beta} - \sigma_{xi}^{\alpha}\sigma_{xj}^{\beta} - \sigma_{yi}^{\alpha}\sigma_{yj}^{\beta}$, and $\omega_D^{ij\alpha\beta}$ is the coupling between spin-α on pair i and spin-β on pair j.

The goal is to introduce a modulated RF field such that the effective Hamiltonian is restricted to just the isolated spin pairs (the first term in Eq. 3.1). Our solution may be understood by viewing the RF field in the interaction frame of this coupling. In the fully symmetric case the state $\sigma_x^1 + \sigma_x^2$ evolves as $(\sigma_x^1 + \sigma_x^2)\cos\left(\frac{3\omega_D^S}{2}t\right) + \left(\sigma_y^1\sigma_z^2 + \sigma_z^1\sigma_y^2\right)\sin\left(\frac{3\omega_D^S}{2}t\right)$, so we chose a RF that has an amplitude modulation frequency $\omega_m = 3\omega_D^S/2$ and is given (in the lab frame) by

$$\begin{aligned} H_{\mathrm{mod}}(t) &= \frac{\hbar\omega_1}{2}\cos\left(\frac{3\omega_D^S}{2}t\right)\times \\ & e^{i(\omega_0 t/2)\sum_i \sigma_z^i}\left(\sum_i \sigma_x^i\right)e^{-i(\omega_0 t/2)\sum_i \sigma_z^i} \end{aligned} \tag{3.2}$$

where ω_0 is the Larmor frequency of the spins. The cosine amplitude modulation produces frequency sidebands at $\omega_0 \pm 3\omega_D^S/2$. Amplitude modulated pulses have previously been used in NMR for simultaneously irradiating multiple transitions in quadrupolar spin systems [49] to create multiple quantum coherences in the regime where the RF power is significantly smaller than the strength of the quadrupolar coupling.

We illustrate a simple physical picture of the averaging process using a 3-spin case. Consider the Hamiltonian (in the rotating frame) of a three-spin system, in which spins 1 and 2 are strongly coupled and spin 3 is weakly coupled to spins 1 and 2 ($\omega_D^S \gg \omega_D^w$), under the RF modulation

$$\begin{aligned} H &= \frac{\hbar\omega_D^S}{4} h_{12} + \frac{\hbar\omega_D^w}{4}\left(h_{13} + h_{23}\right) + \\ &\qquad \frac{\hbar\omega_1}{2}\cos\left(\frac{3\omega_D^S}{2}t\right)\left(\sigma_x^1 + \sigma_x^2 + \sigma_x^3\right) \ . \end{aligned} \tag{3.3}$$

The time-dependent Hamiltonian in the interaction frame of the (1,2) pair interaction is given by

$$\tilde{H}(t) = e^{-i(\omega_D^S t)h_{12}/4}\left(H - \frac{\hbar\omega_D^S}{4}h_{12}\right)e^{+i(\omega_D^S t)h_{12}/4} \tag{3.4}$$

The zeroth order average Hamiltonian [51] of this interaction frame Hamiltonian over a period $\tau = 4\pi/3\omega_D^S$ is

$$\bar{H}^{(0)} = \frac{\hbar\omega_D^w}{2}\left(\sigma_z^1\sigma_z^3 + \sigma_z^2\sigma_z^3\right) + \frac{\hbar\omega_1}{4}\left(\sigma_x^1 + \sigma_x^2\right) \ . \tag{3.5}$$

The system can then be transformed into a second interaction frame via

$$U' = \exp\left(\frac{i\omega_1 t}{4}\left(\sigma_x^1 + \sigma_x^2\right)\right) \ . \tag{3.6}$$

Now, in this second averaging frame of $\bar{H}^{(0)}$ (Eq. 3.6),the first term, i.e. the residual dipolar couplings to spin 3, averages to zero over a cycle $\tau' = 4\pi/\omega_1$. Hence the second averaging of the couplings to spin 3 is efficient when $\omega_1 \gg 4\omega_D^w$, and the effective total system dynamics are generated by the (1,2) dipolar coupling (the Hamiltonian of the first frame transformation). This picture provides the motivation for our approach, but the overall dynamics are more complicated than that suggested by the zeroth-order average shown above. If ω_D^S is not significantly stronger than ω_1, the higher order terms of the Magnus expansion become more important. In addition, if the strength of the 1-3 and 2-3 couplings are different, additional two and three body terms appear in the Hamiltonian.

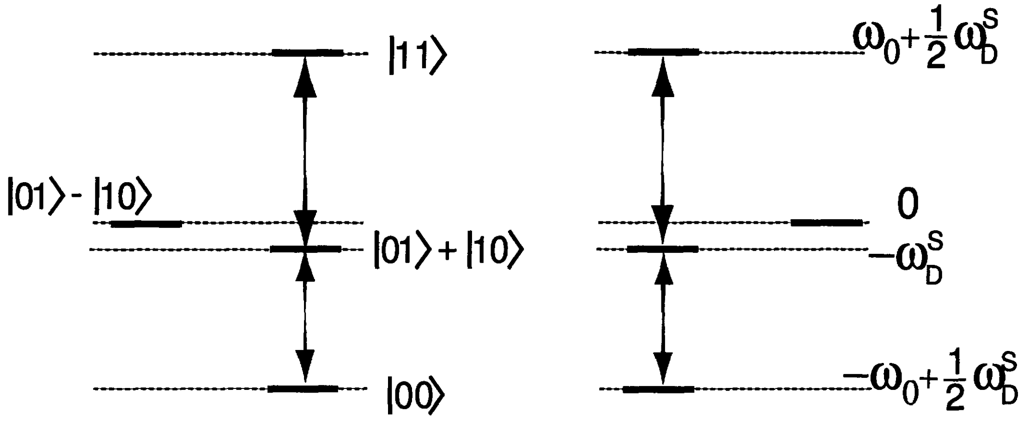

Figure 3-1: Two pairs of strongly coupled spin-$\frac{1}{2}$ systems with each pair decomposed into its singlet and triplet manifolds (in the rotating frame). The triplet manifolds are weakly coupled to each other while the singlet manifolds do not interact.

Further insight may be obtained by considering the energy level structure of an isolated dipole-coupled pair of spin-1/2 nuclei. This has four energy levels, with three triplet levels corresponding to a composite I = 1 system and a non-magnetic singlet with I = 0 [?]. A weakly coupled set of spin pairs will largely preserve this structure, but transitions between the singlet and triplet will no longer be forbidden due to the coupling between spins on different pairs. Let ω_D^w represent the average strength of the weaker couplings. Figure 1 illustrates how the spin pairs are decoupled from each other under the amplitude modulated (AM) RF irradiation. If $\omega_m = 3\omega_D^S/2$, the AM irradiation simultaneously drives transitions $|00\rangle \leftrightarrow |01\rangle + |10\rangle$ and $|01\rangle + |10\rangle \leftrightarrow |11\rangle$ of the triplet manifold. The rate at which these transitions are driven depend on the strength of the modulation field, ω_1. If $\omega_1 \gg \omega_D^w$, the two triplet manifolds are decoupled from each other and the pairs are isolated from each other. However, if the RF power is increased further such that $\omega_1 \geq \omega_D^S$, the triplet sub-space structure gets destroyed as the strong coupling between the spins within the pair is decoupled.

Thus, our scheme works in the regime where $\omega_m = 3\omega_D^S/2$ and $\omega_D^S \gg \omega_1 \gg \omega_D^w$. Not surprisingly these are exactly the same conditions as obtained in the previous section. Intuitively, the RF modulation allows us to move into an interaction frame that is moving with the magnetization of the dipole coupled spin pair. The experiment bears some similarities to the spin-1 decoupling experiments originally proposed by Pines and coworkers [53, 54]. In fact they suggest that their method could be used to decouple a heteronuclear spin from a pair of identical spins. However, the scheme presented here goes further, and permits a coherent evolution of the isolated spin pair while decoupling the pairs from each other.

It is also useful to move into the interaction frame of the RF modulation. The zeroth-order average Hamiltonian [81] of an isolated spin pair in the interaction frame of the RF modulation is

$$\begin{aligned} \bar{H}_d^{(0)} &= -\frac{\hbar}{8}\omega_D^S\left(2\sigma_x^1\sigma_x^2 - \sigma_y^1\sigma_y^2 - \sigma_z^1\sigma_z^2\right) + \\ & \frac{3\hbar}{8}\omega_D^S J_0\left(\frac{4\omega_1}{\omega_D^S}\right)\left(\sigma_z^1\sigma_z^2 - \sigma_y^1\sigma_y^2\right) \ . \end{aligned} \tag{3.7}$$

where the average has again been performed over one period of the amplitude modulation ($t = 2\pi/\omega_m = 4\pi/3\omega_D^S$). Starting from the equilibrium state where the spins are along the external magnetic field, a collective $\pi/2$ rotation of the spins places a spin pair in the initial state $\sigma_x^1 + \sigma_x^2$. This state commutes with the first term of the interaction Hamiltonian shown above, and the effective evolution is only due to the second term $\sigma_z^1\sigma_z^2 - \sigma_y^1\sigma_y^2$. The set of operators, $(\sigma_x^1 + \sigma_x^2,\ \sigma_z^1\sigma_y^2 + \sigma_y^1\sigma_z^2,\ \sigma_z^1\sigma_z^2 - \sigma_y^1\sigma_y^2)$ form a subalgebra under the commutator that is isomorphic to the Cartesian subalgebra $(\sigma_x, \sigma_y, \sigma_z)$. Thus the strongly coupled spins oscillate between the single spin state $\sigma_x^1 + \sigma_x^2$ and the two spin state $\sigma_z^1\sigma_y^2 + \sigma_y^1\sigma_z^2$. If the first term of the Hamiltonian in Eq. 3.7 were absent, this scheme would map onto a nearest neighbor interaction, and as long as the initial state of the spin pairs was within this subspace, leakage out of the subspace would be substantially suppressed. However, in the current scheme, the initial state should be both within the subspace and commute with the first term of Eq. 3.7. For an ensemble of spin pairs, only the collective σ_x state satisfies these conditions.

3.3 Experimental Results

Gypsum ($CaSO_4 \cdot 2\ H_2O$) was taken as a prototypical system for a weakly interacting ensemble of identical spin pairs. The protons in the waters of crystallization comprise the strongly coupled spins. The coupling between protons on different water molecules is significantly smaller than that between protons in the same molecule. A unit cell of gypsum has four water molecules, with two pairs in two inequivalent sites. When the external magnetic field is applied along the [010] orientation, the dipolar splitting at the inequivalent water sites coincide and a Pake doublet is observed (see Fig. 3-2) in a one-pulse experiment [56]. In this orientation the strong dipolar coupling between protons in the water molecule is $\omega_D^S/2\pi = 14.8$ kHz, and the mean coupling between protons on different water molecules is $\omega_D^w/2\pi = 5.5$ kHz.

The experiments were carried out at room temperature at 7.1 T (^{1}H 300 MHz) using a Bruker Avance spectrometer on a 1 mm^3 single crystal of gypsum in the [010] orientation. The length of the $\pi/2$ pulse used was 1.67 μs. The experiment was repeated as the duration of the AM RF was varied from 100 μs to 2.9 ms with an increment of 5.5 μs. The signal was Fourier transformed with respect to the length of the modulation pulse to yield the spectrum shown in Fig. 3-2(b). Fig. 3-2(c) shows the observed $\sum_i \sigma_x^i$ terms plotted against the length of the modulation pulse [57]. A dramatic narrowing of the spectral line is observed in the experiment. The effective T_2 of the spins under the modulation is 11.1 ms which corresponds to a linewidth of 29 Hz. This is a factor of 572 times smaller than the 16.6 kHz width of a single line of the Pake doublet.

In order to demonstrate that the spin pair continues to undergo a coherent evolution, we performed a second series of experiments to specifically filter out and separate the $\sigma_x^1 + \sigma_x^2$ and the $\sigma_y^1\sigma_z^2 + \sigma_z^1\sigma_y^2$ terms. The two experiments are shown in Figure 3-3. Figure 3-5(a) shows the coherence transfer under the dipolar Hamiltonian while Fig. 3-5(b) shows the coherence transfer under the action of the modulation sequence. Under the dipolar coupling the interactions with distant spins rapidly generate higher order spin correlations, and there is a strong damping of the oscillation between the single spin and the two-spin terms. However, under the modulation sequence this oscillation is seen to extend out significantly farther. Thus the observed line-narrowing is not a form of spin-locking of the single spin terms, as occurs under strong RF irradiation,

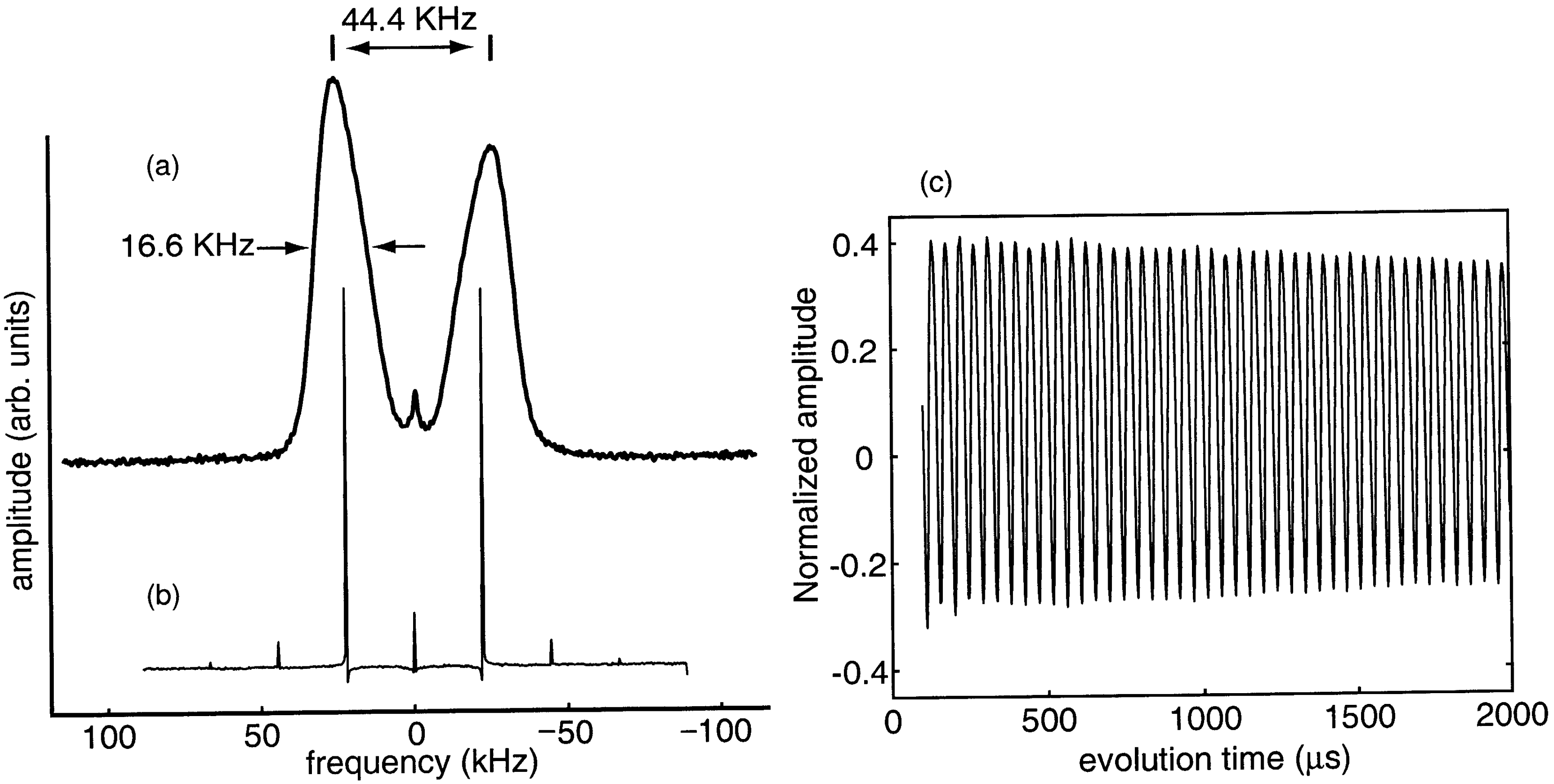

Figure 3-2: (a) The proton spectrum of a single crystal of gypsum in the [010] orientation (Pake doublet). The splitting between the peaks corresponds to $3\omega_D^S/2\pi = 44.4$ KHz. Each peak is broadened due to weak dipolar coupling to the other water molecules. Therefore, $3\omega_D^w/2\pi \sim 16.4$ KHz (b) The line narrowing observed under the modulation sequence with RF amplitude $\omega_1 = 3\omega_D^S/4$. (c) Evolution of the collective single spin $\sum_i \sigma_x^i$ terms under the modulation sequence.

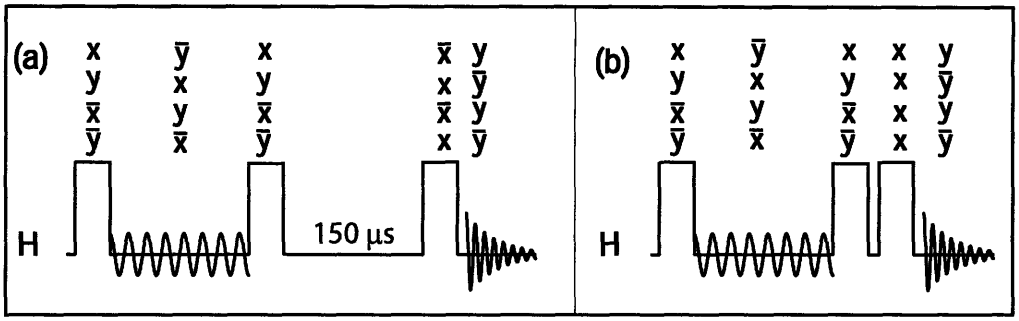

Figure 3-3: (a) pulse sequence used to read out the $\sigma_x^1 + \sigma_x^2$ terms. Following the modulation pulse, a $\pi/2$ pulse is applied to rotate the σ_x terms to σ_z. During the 150 μs interval (much shorter than T_1) all terms other than the σ_z decay. A $\pi/2$ pulse is then used to monitor σ_z. (b) pulse sequence used to read out the $\sigma_y^1\sigma_z^2 + \sigma_z^1\sigma_y^2$ term. Following the modulation two back to back $\pi/2$ pulses act as a double quantum filter to suppress the single spin σ_x terms. A four step phase cycle is necessary to implement the filter.

but is due to the selective decoupling of the weaker interactions between spins on different pairs.

3.4 Conclusions

In conclusion, we have demonstrated that it is possible to restrict the evolution of a dipolar coupled spin network to a much smaller subspace of the system Hilbert space. This restriction allows us to significantly extend the phase coherence times for selected states. The scheme developed works for a system consisting of an ensemble of spin pairs, where the coupling between spins in the same pair is stronger than the coupling between spins on different pairs.

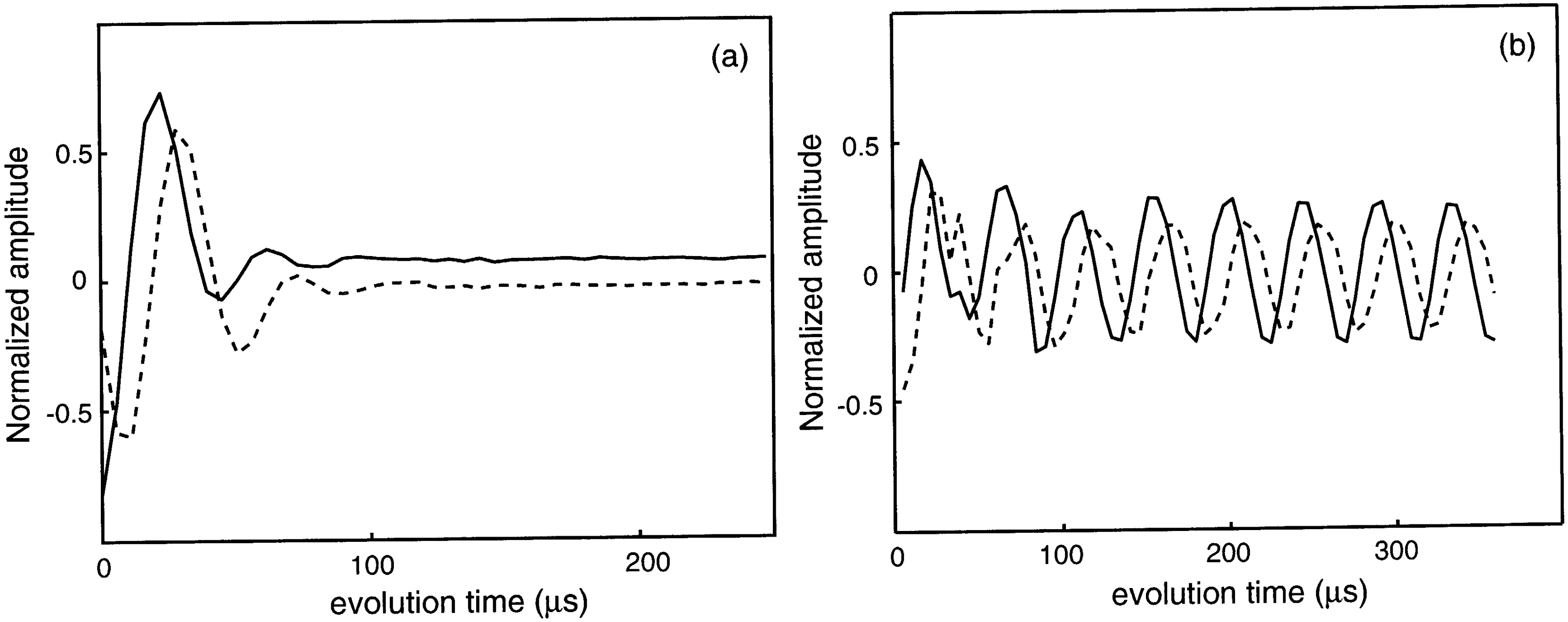

Figure 3-4: The solid line shows the $\sigma_x^1 + \sigma_x^2$ and the dashed line shows the $\sigma_z^1\sigma_y^2 + \sigma_y^1\sigma_z^2$ terms. (a) Under the dipolar Hamiltonian evolution, the above terms evolve into unobservable higher order spin correlations within 100 μs. (b) Under the modulation sequence, the terms oscillate 90 deg out-of-phase with each other for up to 360 μs without any significant attenuation in amplitude. In this case the RF amplitude $\omega_1 = 3\omega_D^S/4$.

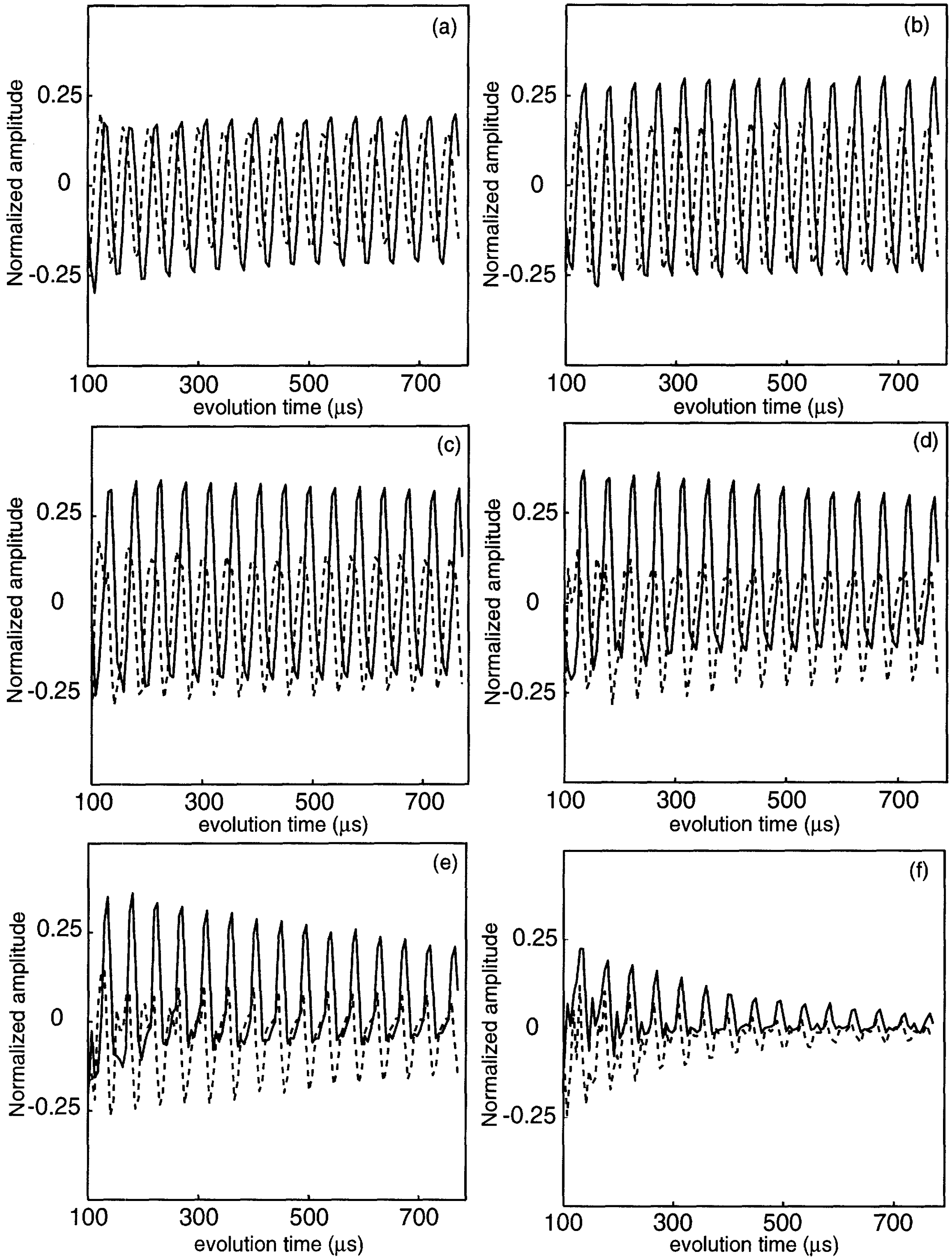

Figure 3-5: The solid line shows the $\sigma_x^1 + \sigma_x^2$ and the dashed line shows the $\sigma_z^1\sigma_y^2 + \sigma_y^1\sigma_z^2$ terms. Under the modulation sequence, the terms oscillate 90 deg out-of-phase with each other. The RF amplitude ω_1 is varied from $2\omega_D^S/4$ to $7\omega_D^S/4$ in steps of $\omega_D^S/4$. When the value of ω_1 is no longer in the optimum range, the amplitude of the signal is significantly attenuated.

CHAPTER 4

SENSITIVITY OF HIGHLY CORRELATED MULTIPLE-SPIN STATES TO THE PRESENCE OF RARE SPINS

4.1 Introduction

Solid-state spin-based NMR QIPs are a useful test-bed for the coherent control of modest Hilbert spaces. Using existing solid-state NMR techniques, one can study the dynamics and control of many-spin states. Here we explore our ability to control many spins in the presence of small number of spin defects. In the following subsection, we give a brief overview of the solid-state NMR techniques used to create and detect these many-spin states.

All the spins in a rigid spin lattice strongly interact with one another through their dipolar fields. In high magnetic fields and following a $\pi/2$ pulse, the evolution of the spin system is dominated by the secular dipolar Hamiltonian. This interaction creates highly correlated multiple-spin states causing the measured signal (Free Induction Decay - FID) to decay. The observable magnetization in NMR (as measured by the FID) comprises of the single-spin single quantum states. These single-spin single quantum states are transformed into unobservable multiple-spin single quantum states under the action of the dipolar Hamiltonian. By encoding the higher order coherences of the multiple-spin states in a non-commuting basis of the secular dipolar Hamiltonian, Cho *et al.* [9] have studied the growth of these coherent multiple spin correlations during the FID. Solid-state NMR provides a ideal test-bed to investigate not only the growth of these large, correlated quantum states but also the dynamics and control of such states.

4.1.1 Creation and detection of highly correlated multiple-quantum states

In a strong magnetic field, $(B_0\hat{z})$, a N-spin $\frac{1}{2}$ system has 2^N stationary states. These states can be classified according to the magnetic quantum number M_z.

$$m = \sum_j m_{zj} = (N_{+\frac{1}{2}} - N_{-\frac{1}{2}})/2 \tag{4.1}$$

where m_{zj} is the eigenvalue of the j^{th} spin in the system. m_{zj} can take the values of either $\pm\frac{1}{2}$. $N_{+\frac{1}{2}}$ and $N_{-\frac{1}{2}}$ are the number of spins pointing up and down respectively. The energy eigenvalue corresponding to m is $E_z = -\gamma\hbar B_0 m$. In the case of non-degenerate states, there are on the order of 2^{2N-1} possible transitions between any two energy levels. The difference in the M_z values between the two levels is known as the coherence number.

When the state of the spin system is expressed in its eigenbasis as a density matrix, the presence of a non-zero matrix element $(< z_i \mid \rho \mid z_j >)$ indicates the presence of a n-quantum coherence where $n = m(z_j) - m(z_i)$ (the difference between the magnetic quantum numbers of the two basis states z_i and z_j). This in turn indicates the presence of a superposition of the basis states z_i and z_j in the state of the spin system.

In theory, one can create multiple-quantum states by exciting the thermal equilibrium spin state $(\rho(0))$ using the double quantum (DQ) Hamiltonian given by:

$$H_{DQ}^{II} = \sum_{j<k} D_{jk}^{II}\{\hat{I}_j^{+}\hat{I}_k^{+} + \hat{I}_j^{-}\hat{I}_k^{-}\} \tag{4.2}$$

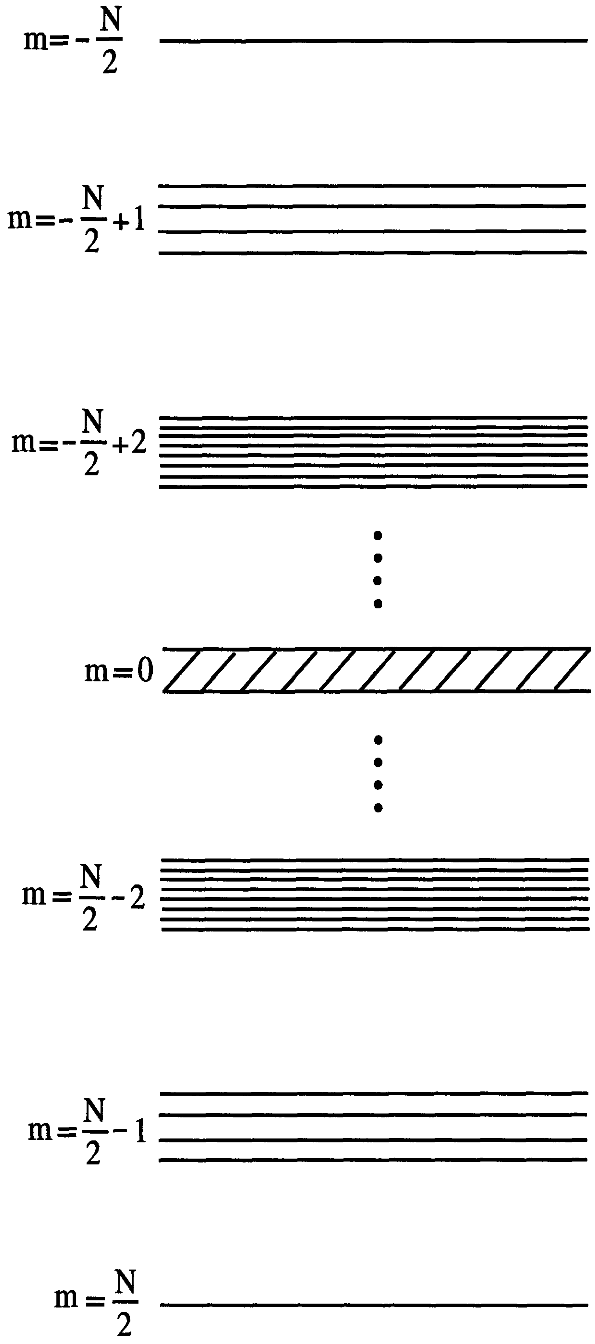

Figure 4-1: Energy level diagram of a N spin-$\frac{1}{2}$ system. The eigenvalue of $\widehat{I}_z$ can take any value from $\frac{N}{2}$ to $\frac{-N}{2}$. The number of levels for each allowed eigenvalue is $\binom{N}{m+\frac{N}{2}}$. Thus the number of allowed single-quantum transitions increase exponentially with N and are thus unresolvable in large spin-systems.

Though this particular form of spin interaction is not provided by nature, it can be engineered using standard multiple-pulse cycles based on coherent averaging techniques [58]. These multiple-pulse cycles implement an effective DQ Hamiltonian ($\overline{H^{II}_{DQ}}$) over the period of the pulse cycles.

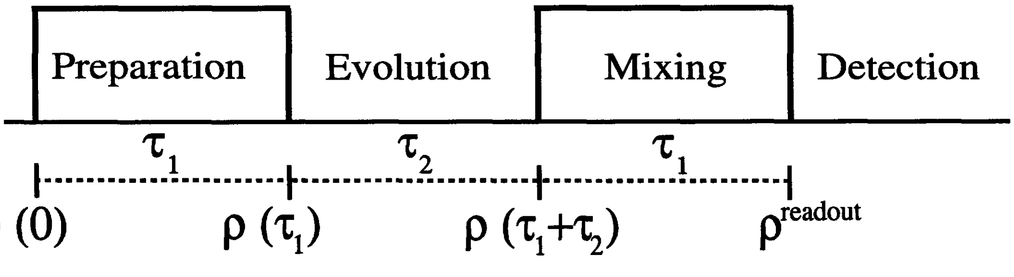

Figure 4-2: The basic form of a multiple-quantum NMR experiment [63] - (i) Preparation: Creating the highly correlated multiple-quantum states. (ii) Evolution: Evolving these states under any desired Hamiltonian. (iii) Mixing: Transforming the higher order coherences to observable single-spin single quantum coherences. (iv) Detection: Measuring the observable single-spin single quantum magnetization

A basic multiple-quantum NMR experiment is shown in Fig. 4-2. The DQ Hamiltonian is effective during τ_1 and creates highly correlated multiple-spin states in the preparation stage. These states give rise to a distribution of higher order coherences, which are encoded as phase factors (ϕ) using a collective rotation about the z-axis ($\sum_j \hat{I}_{jz}$).

$$\rho(\tau_1) = e^{-\imath\phi\sum_j \hat{I}_{jz}} e^{-\imath\overline{H^{II}_{DQ}}\,\tau_1}\ \rho(0)\ e^{\imath\overline{H^{II}_{DQ}}\,\tau_1} e^{\imath\phi\sum_j \hat{I}_{jz}} \tag{4.3}$$

In the evolution stage during τ_2, we evolve the system under any desired Hamiltonian. By time-reversing the DQ Hamiltonian evolution in the mixing stage, higher order coherences are transformed to observable single-spin single quantum terms.

$$\rho^{readout} = e^{\imath\overline{H^{II}_{DQ}}\,\tau_1}\ \rho(\tau_1+\tau_2) e^{-\imath\overline{H^{II}_{DQ}}\,\tau_1} \tag{4.4}$$

$$S(t) \ = \ Tr\{(\sum_j \hat{I}_j^{+})\ \rho^{readout}\} \tag{4.5}$$

To extract the coherence order distribution in $\rho(\tau_1 + \tau_2)$, the signal $(S(t))$ observed in the detection stage is Fourier transformed with respect to ϕ.

Several pulse sequences have been developed to create and detect multiple-quantum coherences [59, 60, 61]. However, time-reversal schemes during preparation and detection are most widely used since they enhance the intensity of the multiple-quantum NMR experiments by refocusing the dipolar interaction [62, 63, 64].

While the advent of a n-quantum coherence in the coherence order distribution guarantees the creation of a n-spin state, it does not arise solely from such a spin state. Thus the distribution of the sizes of the highly correlated spin clusters for various excitation times under the DQ Hamiltonian is not known. However, as the excitation time period - τ_1 increases, higher order spin coherences emerge, indicating an increase in the effective size of these spin clusters. Even without precise knowledge of the size of the spin cluster, one can gain some insight on the many-spin dynamics by manipulating the existing multiple-quantum techniques. These techniques have been used extensively to study many body spin dynamics in dipolar coupled solids [65, 66, 67, 68]. It has also been used to probe spatial relationships between spins in large macromolecules, determine the size of spin clusters and in spin counting experiments [59, 60, 69, 70].

4.1.2 Decay of highly correlated multiple-spin states in CaF_2

The cubic lattice of 100% abundant ^{19}F spin-1/2 nuclei (denoted as **I** in the rest of this section) in a single crystal of CaF_2 have been used to study the decay of highly correlated multiple-spin states. Cho *et al.* report the effective T_2 under the dipolar Hamiltonian and under a time-suspension (C-48) sequence. See Figs. 4-3 and 4-4. The measurement was repeated for various periods of preparation under the grade-raising operator (DQ Hamiltonian). For a given coherence number, larger preparation

---

[3] The experimental data on CaF_2 has been extracted with permission from the doctoral thesis "Exploring large coherent spin systems with solid-state NMR", by H. Cho, submitted to the Department of NSE, MIT, February 2005.

periods incorporate more spins leading to larger clusters of correlated spins. We see in the figures that for both the dipolar evolution and the time-suspension sequence, as the number of spins in the cluster increase, the variation in T_2 with coherence number vanishes. Also, we note that the T_2 grows more slowly with spin number than simple theory predicts.

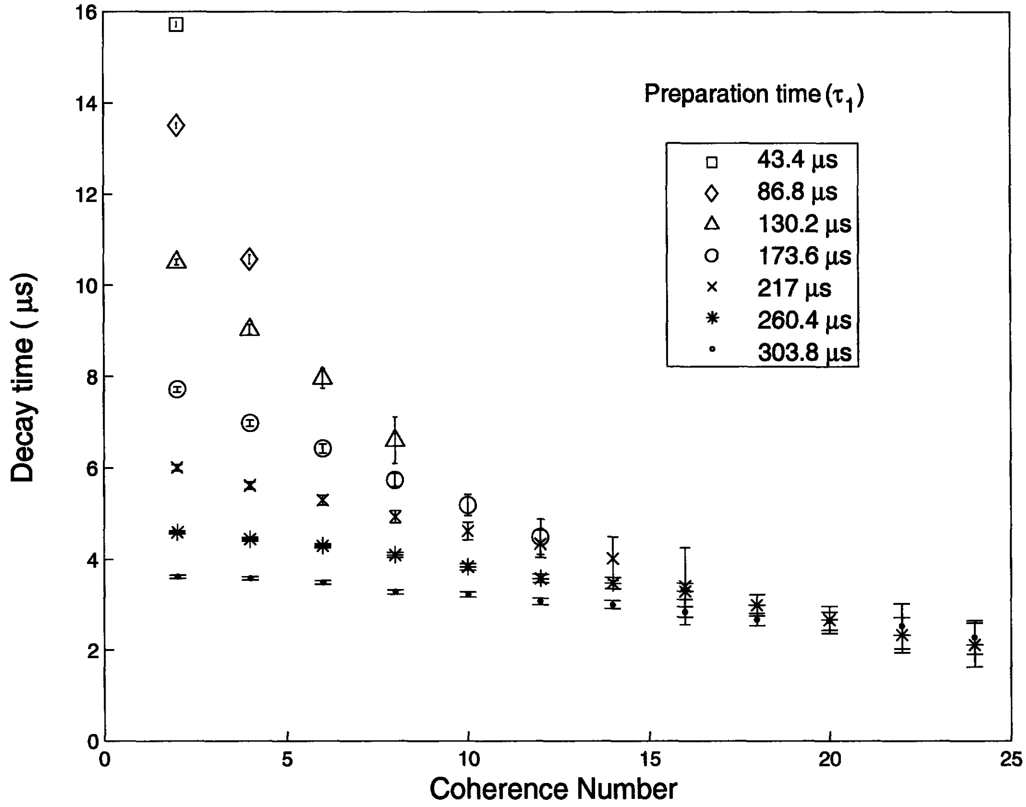

Figure 4-3: Effective decay times of various coherence orders due to the action of the secular dipolar Hamiltonian. Highly correlated spin-^{19}F states in CaF_2 are created by exciting the thermal spin-^{19}F state using the DQ Hamiltonian. The effective decay times of the coherences for the various excitation times (τ_1) are plotted.

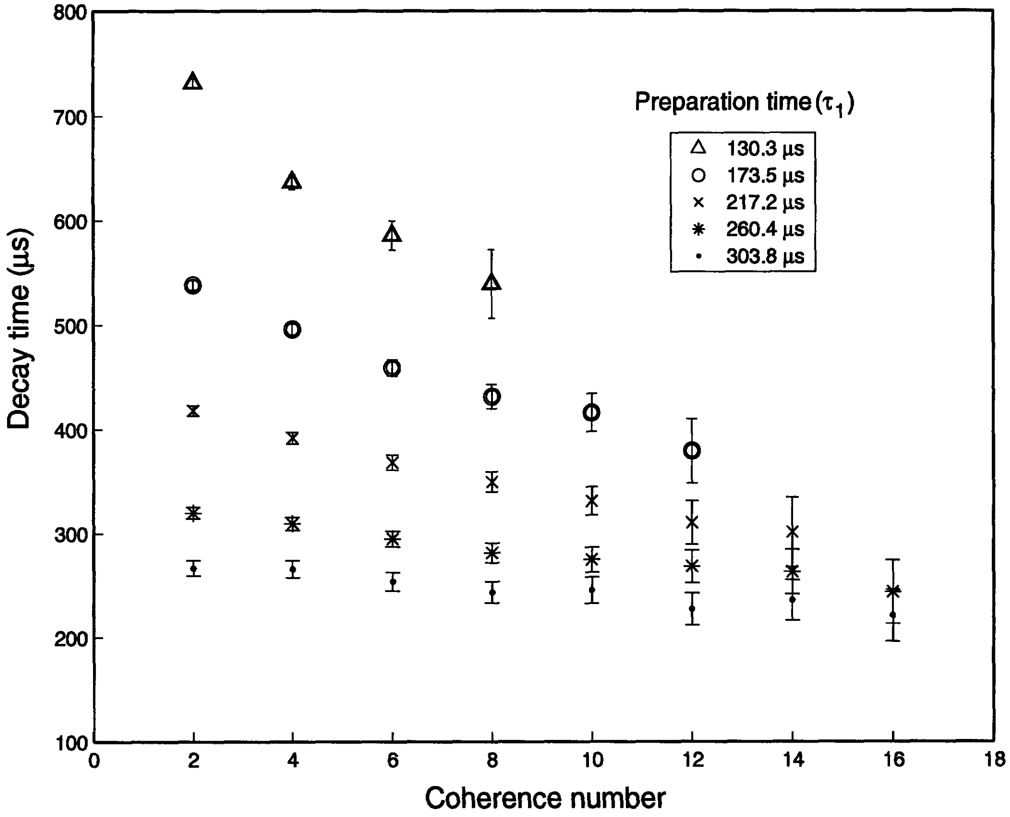

Figure 4-4: Effective decay times of various coherence orders of the the highly correlated spin-^{19}F states in CaF_2. In this case, the secular dipolar Hamiltonian is suppressed using a multiple-pulse C-48 sequence. The effective decay times of the coherences for the various excitation times (τ_1) under the DQ Hamiltonian are plotted.

4.1.3 Effect of rare spins on the decay of the multiple-spin states.

To understand this decay behavior, we take a closer look at the spin-system on which these experiments were carried out. In a CaF_2 single crystal, a spin-7/2 isotope of ^{43}Ca is present in low (0.13%) concentrations. Thus in addition to the homonuclear ^{19}F (H_D^{II}) dipolar spin interactions, the internal Hamiltonian of the spin system includes the heteronuclear ^{19}F-^{43}Ca (H_D^{IS}) and the homonuclear ^{43}Ca (H_D^{SS}) dipolar spin interactions. Denoting this rare spin species as S, the initial equilibrium thermal spin state and the on-resonance internal Hamiltonian are given by:

$$\begin{aligned}
\rho(0) &= \sum_j I_{jz} + \sum_k S_{kz} \\
H_{int} &= H_D^{II} + H_D^{SS} + H_D^{IS} \qquad (4.6) \\
&= H_D^{II} + \sum_{j<k} D_{jk}^{SS}\{\widehat{S}_{jz}\widehat{S}_{kz} - \frac{1}{4}(\widehat{S}_j^{+}\widehat{S}_k^{-} + \widehat{S}_j^{-}\widehat{S}_k^{+})\} + \sum_{j\epsilon I,\ k\epsilon S} D_{jk}^{IS}\ \widehat{I}_{jz}\widehat{S}_{kz}
\end{aligned}$$

The multiple-pulse sequence that creates the effective DQ interaction averages out the heteronuclear interaction (H_D^{IS}) to the 0^{th} order approximation. The efficiency with which the H_D^{SS} and H_D^{IS} interactions are suppressed during this excitation period (τ_1) affect the initial coherence order distribution of the created multiple-quantum spin-**I** states. However, the inefficiencies of the multiple-quantum creation process should not affect their subsequent decay which is the focus our discussion.

The C-48 sequence while averaging out the spin-**I** dipolar interaction, also averages out the heteronuclear interaction. Since $\overline{H_D^{IS}} \sim 0$, we would expect that the presence of **S** spins in the system will have no effect on the multiple-quantum spin-**I** states. If we could instantaneously 'switch-off' the dipolar coupling between the **I** and the **S** spins, our naive expectation would indeed hold true. However, this heteronuclear interaction is *not zero* at any given time point during the C-48 sequence. It *averages to zero* over the total cycle time of C-48 sequence. Thus we should not neglect the presence of **S** spins in the system.

To get a more intuitive understanding, we consider a model spin system comprising of a single **S** spin (labeled as $\mathbf{S_1}$) and an abundant number of **I** spins with a internal Hamiltonian given by

$$H_{int} = H_D^{II} + H_D^{IS_1} = H_D^{II} + \sum_j D_{j1}^{IS_1}\ \widehat{I}_{jz}\widehat{S}_{1z} \qquad (4.7)$$

Applying the DQ Hamiltonian on the equilibrium thermal spin state, we create our initial multiple-quantum spin-**I** states. The corresponding density matrix $\rho(\tau_1)$ is

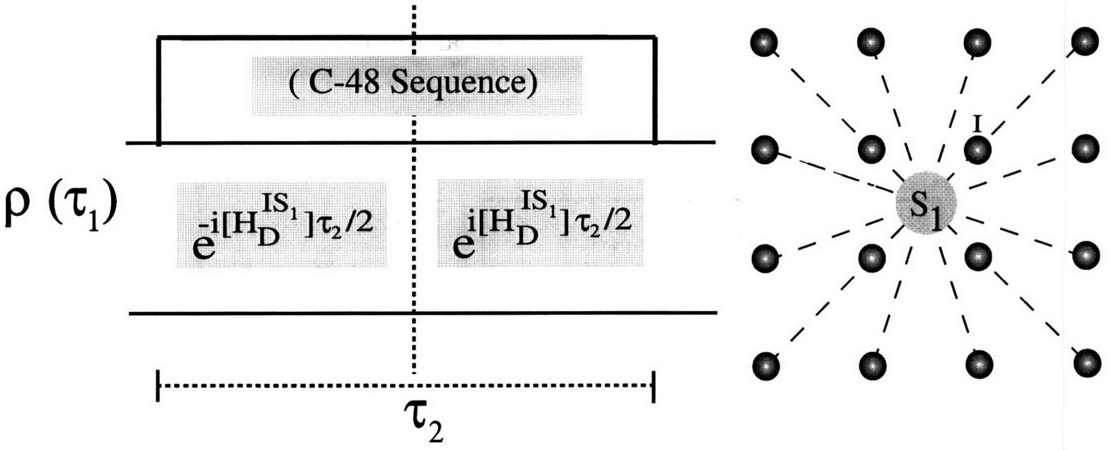

Figure 4-5: The model system (on the right), consists of one **S** spin (labeled as $\mathbf{S_1}$) interacting with an abundant number of **I** spins. The C-48 sequence averages out the homonuclear interaction between the **I** spins during τ_2. During this time interval (τ_2), $\mathbf{S_1}$ is correlated with the multiple-quantum spin-**I** states present in $\rho(\tau_1)$. But if the $\mathbf{S_1}$ spin state remains constant during τ_2, the heteronuclear interaction is also averaged out under the action of the C-48 sequence. Thus $\mathbf{S_1}$ is *no longer correlated* to the spin-**I** states at the end of τ_2. However if $\mathbf{S_1}$ flips at any point during this interval, it will *remain correlated* with the spin-**I** states even at the end of τ_2.

allowed to evolve under the C-48 sequence over a time period τ_2.

$$\rho^I(\tau_1) = Tr_{S_1}[e^{-\imath \overline{H_{DQ}^{II}}}\ \rho(0)\ e^{\imath \overline{H_{DQ}^{II}}\ \tau_1}] \tag{4.8}$$

$$\rho^I(\tau_1+\tau_2) = Tr_{S_1}[U^{-IS_1}(\frac{\tau_2}{2})U^{IS_1}(\frac{\tau_2}{2})\rho(\tau_1)U^{\dagger IS_1}(\frac{\tau_2}{2})U^{\dagger -IS_1}(\frac{\tau_2}{2})] = \rho^I(\tau_1) \tag{4.9}$$

Since the C-48 sequence averages out the $H_D^{IS_1}$ interaction, the density matrix (obtained following a partial trace of the $\mathbf{S_1}$ spin) $\rho^I(\tau_1+\tau_2)$ undergoes zero net evolution over the period τ_2 (as shown in Eq. 4.9). Now if the $\mathbf{S_1}$ spin flips in the middle of τ_2, the density matrix (obtained after tracing out $\mathbf{S_1}$) is no longer preserved.

$$\begin{aligned}\rho^I(\tau_1+\tau_2) &= Tr_{S_1}[U^{-IS_1}(\frac{\tau_2}{2})U^{S_1}(\frac{\pi}{\omega})U^{IS_1}(\frac{\tau_2}{2})\rho(\tau_1)U^{\dagger IS_1}(\frac{\tau_2}{2})U^{\dagger S_1}(\frac{\pi}{\omega})U^{\dagger -IS_1}(\frac{\tau_2}{2})] \\ &\neq \rho^I(\tau_1) \end{aligned} \tag{4.10}$$

This holds true independent of when the spin flips during the course of the time interval. See Fig. 4-5. In a solid-state spin system, energy conserving spin-flips can occur due to the flip-flop term of the homonuclear dipolar interaction.

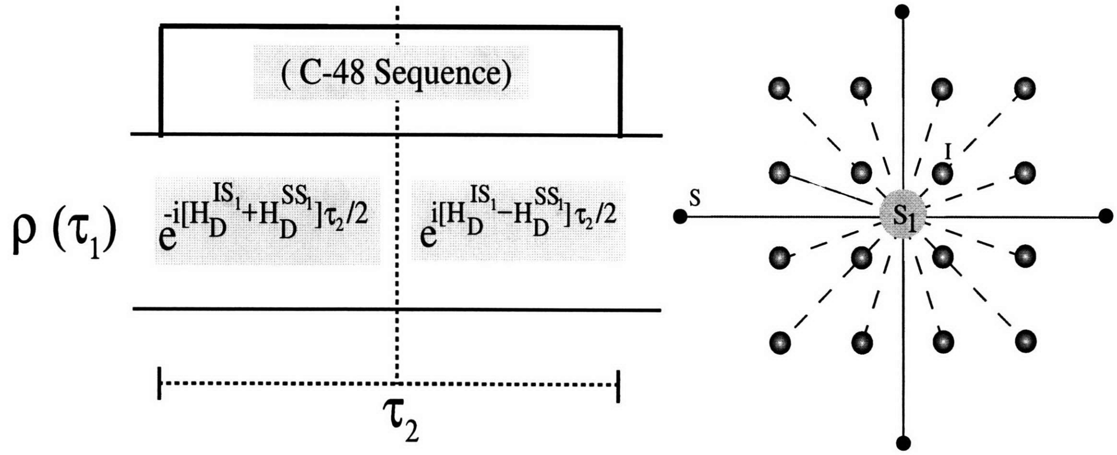

Figure 4-6: The model system (on the right), consists of one **S** spin (labeled as $\mathbf{S_1}$) interacting with an abundant number of **I** spins and a few neighboring **S** spins. We assume that these **S** spins interact *only* with the $\mathbf{S_1}$ spin. The homonuclear interaction between the **I** spins is averaged out during τ_2 using the C-48 sequence. The Hamiltonians $H_D^{IS_1}$ and $H_D^{SS_1}$ do not commute. Thus the multiple-quantum spin **I** states present in $\rho(\tau_1)$ evolve under their action during τ_2.

To incorporate these spin-flip effects, we upgrade our model system to include a few neighboring **S** spins that interact with the $\mathbf{S_1}$ spin. To simplify our arguments, we assume that these **S** spins do not interact with each other or with the **I** spins. These assumptions do not affect the conclusion we derive from the following arguments. The internal Hamiltonian of our model system is given by Eq. 4.11.

$$\begin{aligned} H_{int} &= H_D^{II} + H_D^{SS_1} + H_D^{IS_1} \\ &= H_D^{II} + \sum_j D_{j1}^{SS_1}\{\widehat{S}_{jz}\widehat{S}_{1z} - \frac{1}{4}(\widehat{S}_j^+\widehat{S}_1^- + \widehat{S}_j^-\widehat{S}_1^+)\} + \sum_{j\epsilon I} D_{j1}^{IS_1}\,\widehat{I}_{jz}\widehat{S}_{1z} \end{aligned} \tag{4.11}$$

Under the dipolar interaction $H_D^{SS_1}$, the total spin-**S** magnetization is conserved, not the state of the individual spin- $\mathbf{S_1}$. Therefore, the Hamiltonians $H_D^{SS_1}$ and $H_D^{IS_1}$ do not commute and the net evolution during the first half of τ_2 can no longer be refocused during the second half. See Fig. 4-6.

$$\rho^I(\tau_1+\tau_2) \;=\; Tr_{S_1}[U^{SS_1-IS_1}(\frac{\tau_2}{2})U^{SS_1+IS_1}(\frac{\tau_2}{2})\rho(\tau_1)U^{\dagger SS_1+IS_1}(\frac{\tau_2}{2})U^{\dagger SS_1-IS_1}(\frac{\tau_2}{2})] \;\neq\; \rho^I(\tau_1)$$

When the coherence order distribution of spin-**I** states is extracted from $\rho^I(\tau_1+\tau_2)$, we will see a decay of the higher order coherences. Thus in this simple model, a single spin-**S** ($\mathbf{S_1}$) interacting with neighboring **S** spins act as a spin defect for the highly correlated spin **I** states.

Going back to the coherence decay experiments under the secular dipolar Hamiltonian, neglecting arbitrary errors in experimental implementation, H_D^{II} and H_D^{IS} average to zero. However, the finite time period over which the heteronuclear decoupling takes place ensures that energy-conserving spin flips between neighboring **S** spins will lead to multiple-quantum spin-**I** transitions which are not refocused during the time-reversal of the DQ Hamiltonian - thus leading to a coherence order decay. Therefore, we need to refocus the homonuclear interaction (H_D^{SS}) since it facilitates these energy-conserving spin flips via the flip-flop component of its Hamiltonian. Moreover, the H_D^{IS} interaction needs to be averaged out on a time-scale which is fast with respect to the spin-**S** homonuclear dipolar coupling strength.

The C-48 sequence applied on the ^{19}F spins suppresses only the homonuclear ^{19}F interactions and the heteronuclear ^{19}F-^{43}Ca interactions. Thus the ^{43}Ca spins act as centers of decoherence for the highly correlated multiple-spin states of the abundant ^{19}F spins. We need to design new control sequences that address these rare spin homonuclear interactions and thus refocus the full internal Hamiltonian of the spin system. The decay rates of the highly correlated abundant spin states measured under this complete refocusing scenario will provide a more accurate measure of control of such states.

4.1.4 Sensitivity the of highly correlated multiple-spin states to the presence of rare spins

Quantifying the effect of these rare spins on the spin system dynamics is quite challenging - techniques that involve direct observation of these rare spins are experimentally unviable due to low S/N ratios. 'Spy detection' techniques [72] allows us to circumvent this problem by letting us take advantage of the higher bulk sensitivity (due to higher concentration) of the abundant spins in the system. This technique utilizes a particular spin species as a probe to monitor the behavior of a neighboring spin species. Spy techniques have been used to study spin diffusion in a single crystal of ferrocene. Ernst *et al.* proposed an indirect measurement of diffusion among the abundant spins (^1H) using the rare spins (^{13}C) as a probe.

For our sensitivity measurements, we excite the abundant spins in the system using the DQ Hamiltonian. This creates highly correlated multiple-spin states while preserving thermal $\hat{z}$ magnetization of the rare spins. We then isolate the effect of the rare spins on the dynamics of these abundant spin clusters. This involves designing a control sequence that selectively turns on the dipolar interaction between the rare spins and clusters of the abundant spins. Since all the spins (both abundant and rare) interact at all times through their dipolar couplings and chemical shifts, we must simultaneously suspend all the homonuclear spin interactions. To quantify a change in response, we also need a reference experiment against which we can measure this change. We design another control sequence, which in addition to suspending all the above interactions, turns off the interactions between the abundant spin clusters and the rare spins. We measure the relative intensities of the multiple quantum coherence of the abundant spins in both cases. Comparison of the intensities allow us to quantify the sensitivity of the abundant spin clusters to the rare spin defects. In the rest of this chapter, we refer to these two multiple-pulse control sequences as the heteronuclear recoupling (HR-96) sequence and the time-suspension (TS-96) sequence respectively. In the next section, we give a brief overview of average hamiltonian theory which was used to design these control sequences.

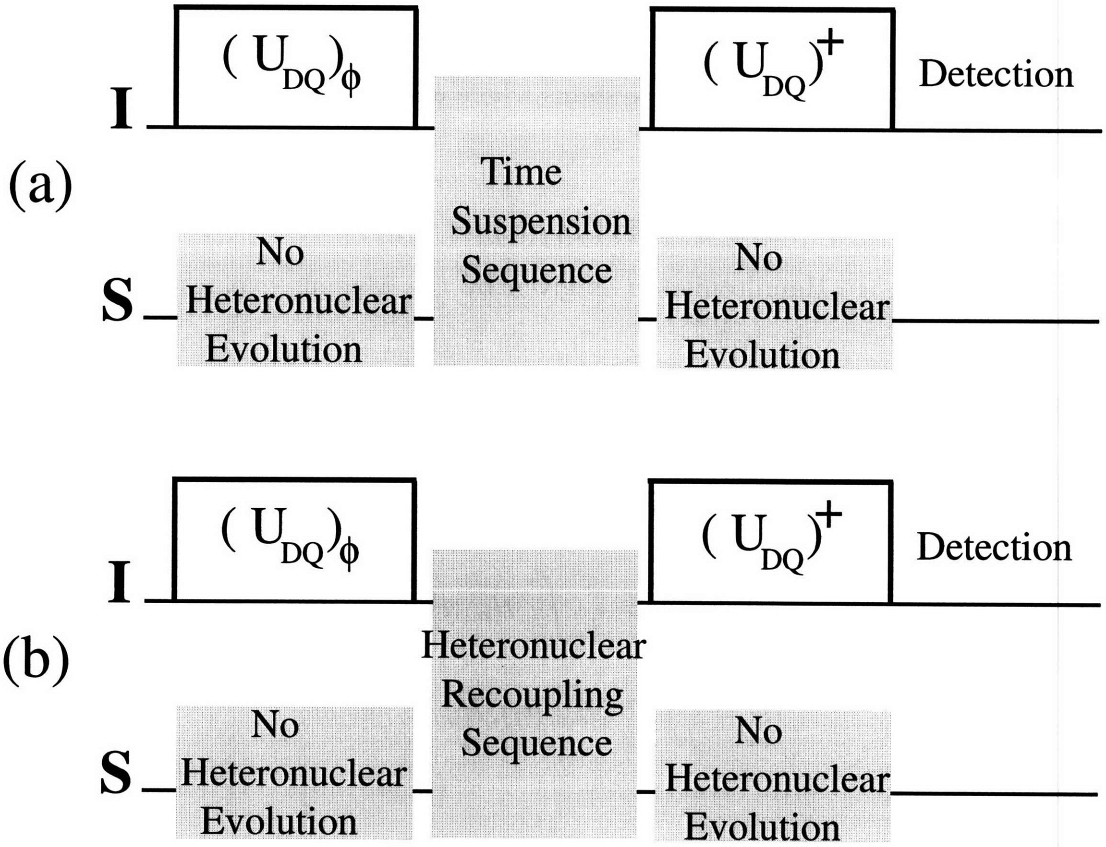
(a)
I
$(U_{DQ})_\phi$
Time Suspension Sequence
$(U_{DQ})^+$
Detection
S
No Heteronuclear Evolution
No Heteronuclear Evolution
(b)
I
$(U_{DQ})_\phi$
Heteronuclear Recoupling Sequence
$(U_{DQ})^+$
Detection
S
No Heteronuclear Evolution
No Heteronuclear Evolution

Figure 4-7: Sketch of the experiments designed to detect rare spins (**S**) using the highly correlated multiple-spin states of the abundant spins (**I**) as a 'probe'. It involves contrasting the effect of the two control sequences (in (a) and (b)) on the intensity of the multiple quantum coherence of these correlated spin **I** states.

4.2 Overview of average Hamiltonian theory

The concept of average hamiltonian theory has been used to design a wide range of pulse experiments. If a spin system is evolved under a periodic and cyclic sequence of RF pulses and delays (i.e., free evolution under the internal Hamiltonian), at periodic observation points it acts as if it was exposed to a time-independent average internal Hamiltonian. The time period between successive observations must however be much smaller then the spin lattice relaxation times. In between these observation times, the spin system passes through a complex array of states depending on the applied RF pulses. The average Hamiltonian defines the state of the system at successive observation times also known as the cycle time (t_c) of the sequence. One of the important features of this theory is that it provides a simplified means of designing pulse sequences in solid state spin systems where calculations using density matrices are not possible.

If the sequence of RF pulses is cyclic ($U_{rf}(t_c) = \pm 1$), periodic ($H_{rf}(t) = H_{rf}(t + Nt_c)$), the average Hamiltonian $\overline{H}$ is given by the Magnus expansion (written as Eq. 4.12). The 0^{th} order average Hamiltonian is given by Eq. 4.13 and the 1^{st} order average is given by Eq. 4.14.

$$\overline{H} = \overline{H^0} + \overline{H^1} + \overline{H^2} + \overline{H^3} + ... \tag{4.12}$$

$$\overline{H^0} = \frac{1}{t_c} \int_0^{t_c} \widetilde{H}_{int}(t)dt \tag{4.13}$$

$$\overline{H^1} = \frac{-i}{t_c} \int_{t_1}^{t_2} [\widetilde{H}_{int}(t_1), \widetilde{H}_{int}(t_2)]dt_1dt_2 \tag{4.14}$$

where $\widetilde{H}_{int}(t)$, also know as the toggling frame internal Hamiltonian, is given by

$$\widetilde{H}_{int}(t) = U_{RF}^{-1} H_{int} U_{RF} \tag{4.15}$$

U_{RF} which is the unitary RF operator determined by the applied pulse sequence, is given by the Dyson time-ordering functional as expressed in Eq. 4.16. Each term U_i refers to the propagator corresponding to the i^{th} RF pulse of the pulse sequence.

$$U_{RF} = Te^{-i\int_0^{t_c} \widetilde{H}_{RF}(t)dt} = ...U_4U_3U_2U_1 \tag{4.16}$$

Since the RF field is of finite strength, the evolution of the internal Hamiltonian during the duration of the pulse should be taken into account. The convergence of the series has been discussed by Maricq [73]. If the cycle time of the pulse sequence is short compared to the T_2 characterizing the homogenous broadening due to the interaction being averaged, the RF fields applied during experiments are strong enough that calculation of the first two terms of the Magnus expansion (as given by Eqs. 4.13 and 4.14) provide a good approximation of the average Hamiltonian $\overline{H}$. Furthermore, designing the RF cycle to be symmetric gives the added advantage that all the odd order terms identically go to zero [74, 75]. This appealing property has been used repeatedly to design line narrowing sequences.

4.3 The C-48 time-suspension sequence

Time-suspension sequences have been widely used in NMR for purposes of imaging in solid-state samples [76, 77, 78]. Designing multiple-pulse cycles, that improve the line-narrowing efficiency by compensating for pulse errors while averaging out the dipolar spin interactions, has been the goal of NMR physicists since coherent averaging techniques were proposed [58, 75]. Other uses of time suspension sequences include the study of spin diffusion and molecular motion through relaxation experiments [79, 80].

Table 4.1: The average Hamiltonian for various time-suspension sequences

Average Hamiltonian terms	Second-averaged MREV-8	16 pulse cycle	24 pulse cycle
$\overline{H}_D^0$	0	0	0
$\overline{H}_D^1$	0	0	0
$\overline{H}_D^2$	$\neq 0$	$\neq 0$	0
$\overline{H}_{DO}^1$	0	0	$\neq 0$
$\overline{H}_O^0$	0	0	0

If a homonuclear spin system is off-resonance, the internal Hamiltonian can be written as $H_{int} = H_O + H_D$, where H_O and H_D are given by Eq. 4.17

$$\begin{aligned} H_O &= \hbar\Delta\omega^I \sum_j I_{jz} \\ H_D &= \sum_{j<k} D_{jk}^{II}\{\widehat{I}_{jz}\widehat{I}_{kz} - \frac{1}{4}(\widehat{I}_j^+\widehat{I}_k^- + \widehat{I}_j^-\widehat{I}_k^+)\} \end{aligned} \tag{4.17}$$

The WAHUHA sequence, the second-averaged MREV-8 and other 16 and 24 pulse supercycles based on the MREV-8 sequence, average out some or all of these homo nuclear spin interactions with varying degrees of efficiency [81, 82]. The average internal Hamiltonians under these time-suspension sequences are listed in Table 4.1. By focussing on the state of the offset Hamiltonian in the toggling frame, Burum and Rhim used a simple notation to describe multiple-pulse cycles. For e.g., the toggling frame offset Hamiltonian during a solid-echo pulse pair cycle: τ— $(\pi/2)_x$— τ— $(\pi/2)_y$— τ can be written as $(I_z, -I_y, -I_x)$. Denoting the three orthogonal directions in the spin space as **a**, **b** and **c**, this solid-echo pulse sequence can be rewritten as $(\mathbf{a}\overline{\mathbf{bc}})$. Using this notation, the three time-suspension sequences can be written as follows:

- Second averaged MREV-8: $(\mathbf{abc})(\mathbf{cba})_p(\mathbf{a}\bar{\mathbf{b}}\mathbf{c})(\mathbf{c}\bar{\mathbf{b}}\mathbf{a})_p$.
- The 16-pulse cycle: $(\mathbf{abc})(\mathbf{c}\overline{\mathbf{ba}})_p(\bar{\mathbf{a}}\mathbf{b}\bar{\mathbf{c}})(\overline{\mathbf{cba}})_p(\mathbf{a}\overline{\mathbf{bc}})(\bar{\mathbf{c}}\mathbf{b}\bar{\mathbf{a}})_p(\overline{\mathbf{ab}}\mathbf{c})(\mathbf{cba})_p$
- The 24-pulse cycle: $(\mathbf{abc})(\mathbf{c}\bar{\mathbf{a}}\mathbf{b})(\mathbf{cb}\bar{\mathbf{a}})_p(\overline{\mathbf{ac}}\mathbf{b})(\mathbf{bac})(\mathbf{c}\bar{\mathbf{b}}\mathbf{a})_p(\mathbf{ab}\bar{\mathbf{c}})(\overline{\mathbf{cab}})(\bar{\mathbf{b}}\mathbf{c}\bar{\mathbf{a}})_p(\overline{\mathbf{acb}})(\bar{\mathbf{b}}\mathbf{a}\bar{\mathbf{c}})(\overline{\mathbf{cba}})_p$

where the sub-script p indicates that the RF pulse pair are phase toggled.

In [83], Cory *et al.* proposed a sequence that averaged the dipolar Hamiltonian and the dipolar-offset cross term to zero up to the 1^{st} order. The C-48 sequence is made up of three-pulse sequences -$A, a, B, b, C, c, ...H, h$. See Figs. 4-8 and 4-9. Various permutations and combinations of two of these three-pulse sequences lead to the formation of dipolar-decoupled π pulse cycles, e.g., (Aa),(Bb),(Cc),(Dd),(Ee)...Eight of these dipolar-decoupled π pulse cycles are combined to form a 'super cycle' that averages out to zero all the terms in Table 4.1. The complete C-48 sequence can be written as: $(Aa)(Bb)(Cc)(Dd)(Ee)(Ff)(Gg)(Hh)$.

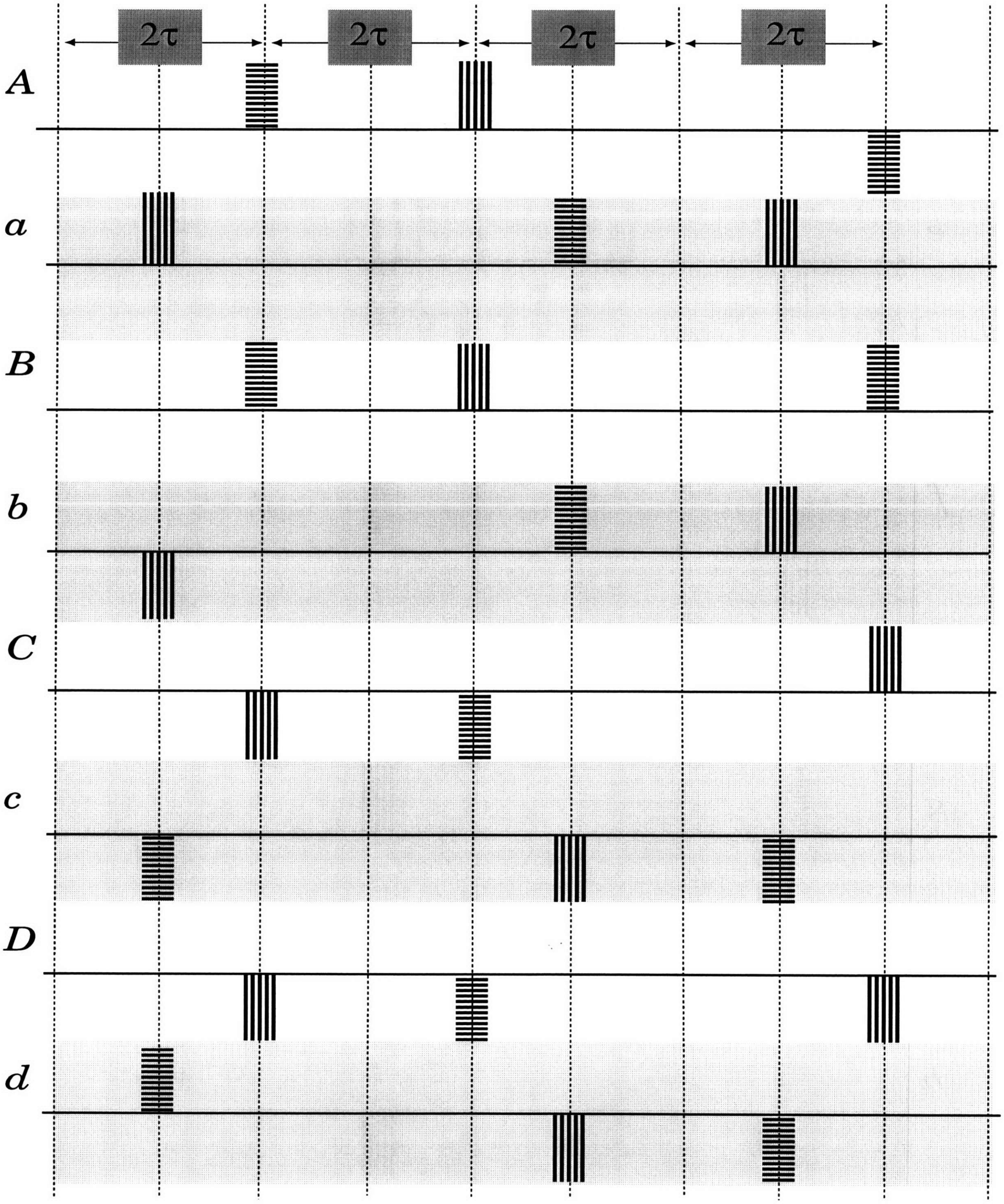

Figure 4-8: The schematic diagram of the three-pulse sequences used to design the C-48 sequence, where the horizontal striping indicates an y-pulse, vertical striping an x-pulse. All the pulses induce rotations by $\pi/2$. (or the negatives thereof if the pulses are below the bold reference lines)

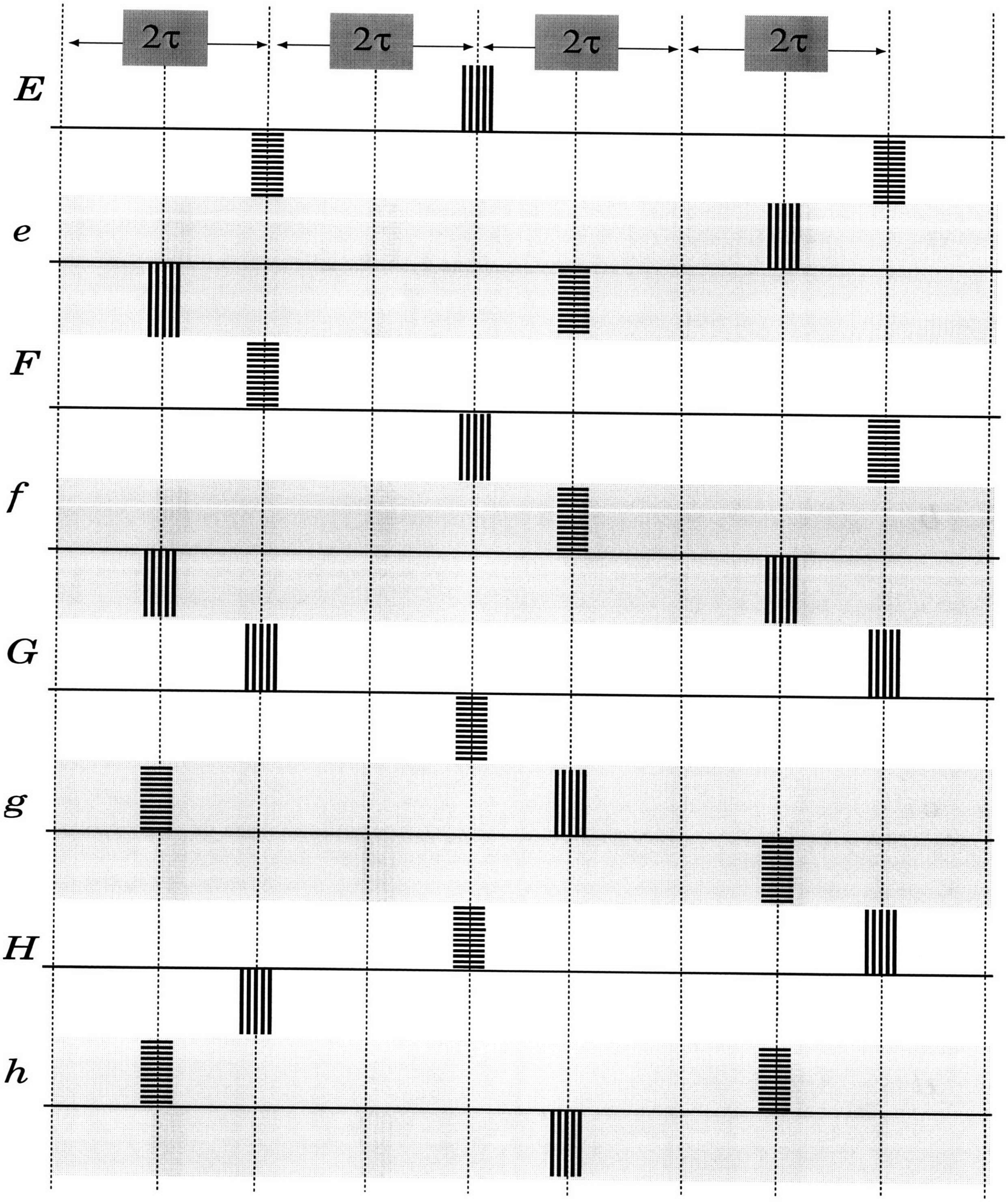

Figure 4-9: The schematic diagram of the three-pulse sequences used to design the C-48 sequence, where the horizontal striping indicates an y-pulse, vertical striping an x-pulse. All the pulses induce rotations by $\pi/2$. (or the negatives thereof if the pulses are below the bold reference lines)

4.4 The design criteria for the new time-suspension and heteronuclear recoupling sequences

In a heteronuclear spin system, the internal Hamiltonian is modified to include both the homonuclear as well as the heteronuclear spin interactions.

$$\begin{aligned} H_O &= \hbar\Delta\omega^I \sum_j I_{jz} + \hbar\Delta\omega^S \sum_k S_{kz} \\ H_{int} &= H_D^{II} \ + \ H_D^{SS} \ + \ H_D^{IS} \\ &= \sum_{j<k} D_{jk}^{II}\{\widehat{I}_{jz}\widehat{I}_{kz} - \frac{1}{4}(\widehat{I}_j^+\widehat{I}_k^- + \widehat{I}_j^-\widehat{I}_k^+)\} \ + \ \sum_{j<k} D_{jk}^{SS}\{\widehat{S}_{jz}\widehat{S}_{kz} - \frac{1}{4}(\widehat{S}_j^+\widehat{S}_k^- + \widehat{S}_j^-\widehat{S}_k^+)\} \\ &\quad + \sum_{j\epsilon I,\ k\epsilon S} D_{jk}^{IS}\{\widehat{I}_{jz}\widehat{S}_{kz}\} \end{aligned} \tag{4.18}$$

D_{jk}^{IS} is the heteronuclear dipolar coupling constant between the j^{th} spin-**I** and the k^{th} spin-**S**. The homonuclear dipolar constants for the j^{th} and k^{th} spins of spin-**I** (or spin-**S**) is defined by D_{jk}^{II} (or D_{jk}^{SS} respectively). In general, the dipolar constant can be defined as

$$D_{jk}^{\alpha\beta} \ = \ \frac{\gamma_\alpha\gamma_\beta\,\hbar^2}{r_{jk}^3}\ (\ 1 \ - \ 3cos^2\theta_{jk}\ ) \tag{4.19}$$

where γ_α and γ_β are the gyromagnetic ratios, $\overrightarrow{r}_{jk}$ is the distance between j^{th} spin-α and k^{th} spin-β, and θ_{jk} is the angle between the external magnetic field and the internuclear vector $\overrightarrow{r}_{jk}$.

In designing the new time-suspension sequence, the objective was to average out all the homonuclear and heteronuclear interactions as expressed in Eq. 4.18. Note that if the C-48 sequence is applied to one of nuclear spin species, for e.g. spin-**I**, the **S** spins will evolve under the spin-S offset and dipolar terms (the 2nd term of H_O and H_D respectively in Eq. 4.18). However, since the spin-**I** offset term goes to zero to the 0^{th} order, the heteronuclear dipolar interaction between the **I** and **S** spins (i.e., the 3rd term of H_D in Eq. 4.18) also goes to zero. Applying the C-48 sequence to both **I** and **S** spins will average out all the homonuclear interactions. However, it will lead to a resultant heteronuclear strong coupling (**I.S**) interaction.

The dipolar spin interactions have varying strengths. We assume that for our model system, the average strength of the dipolar spin interactions (in descending order) can be written as: $D^{II} \gg D^{IS} \gg D^{SS}$. Note that for many typical solid-state samples, these are the correct assumptions. Since the spin-**I** average homonuclear dipolar interaction is the strongest, it needs to be averaged out faster than the other interactions. Using the three-pulse sequences – $A, a, B, ...h$ (shown in Figs. 4-8 and 4-9) as building blocks, we construct two 96-pulse sequences for the **S** spins. The multiple-pulse cycles of the TS-96 and HR-96 sequences average out the spin-**S** dipolar and offset interactions. At the same time, the multiple-pulse cycle of the HR-96 sequence selectively reintroduces the heteronuclear dipolar interaction. To average out the spin-**I** dipolar and offset interactions, we apply two back-to-back C-48 sequences to the **I** spins. Both pulse sequences consist of 16 six-pulse sub-cycles. Each six-pulse sub-cycle averages the homonuclear dipolar Hamiltonian (for both **I** and **S** spins) to zero. The details of the composition are written in Table 4.2. In the case of the TS-96 sequence, the complete averaging out of all interactions require 16 sub-cycles (96 pulses). The RF sequence applied during sub-cycles 9:16 is the same as that applied during sub-cycles 1:8 *except* that all 48 pulses in the first eight sub-cycles are phase shifted by π. For e.g. in Table 4.2, $\overline{a}$ denotes a pulse-sequence in which the three applied RF pulses of the pulse-sequence a are phase shifted by π. In the case of the HR-96 sequence, all undesired interactions are averaged out at the end of sub-cycle number 8 i.e., after every 48 pulses. Thus in sub-cycles 9:16, the sequence applied in sub-cycle 1:8 is repeated. This was done to ensure that both sequences had the same cycle time.

Table 4.2: Composition of the sub-cycles of the TS-96 and HR-96 sequences

Sub-cycles numbers n	TS-96		HR-96	
	I	**S**	**I**	**S**
1	Aa	aE	Aa	bE
2	Bb	fB	Bb	fA
3	Cc	dG	Cc	dG
4	Dd	hD	Dd	hC
5	Ee	bF	Ee	aF
6	Ff	eA	Ff	eB
7	Gg	cH	Gg	cH
8	Hh	gC	Hh	gD
9	Aa	$\overline{aE}$	Aa	bE
10	Bb	$\overline{fB}$	Bb	fA
11	Cc	$\overline{dG}$	Cc	dG
12	Dd	$\overline{hD}$	Dd	hC
13	Ee	$\overline{bF}$	Ee	aF
14	Ff	$\overline{eA}$	Ff	eB
15	Gg	$\overline{cH}$	Gg	cH
16	Hh	$\overline{gC}$	Hh	gD

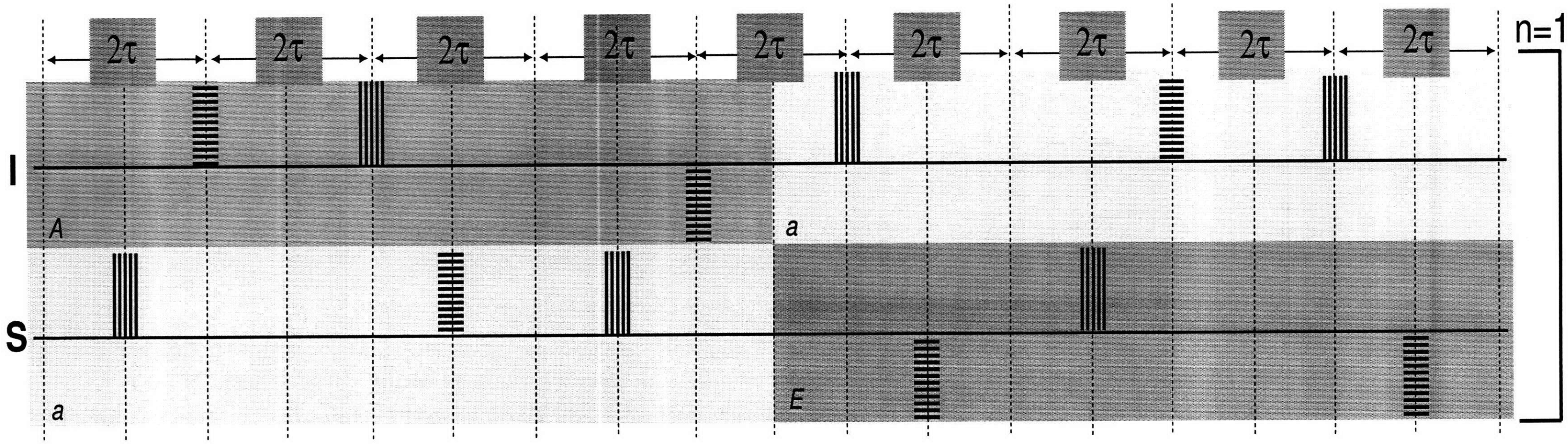

Figure 4-10: (a) The first sub-cycle (n=1) of the time-suspension (TS-96) sequence: **I**-(Aa), **S**-(aE). The sequence is made up of 16 such sub-cycles. The horizontal striping indicates an y-pulse, vertical striping an x-pulse. All the pulses induce rotations by $\pi/2$. (or the negatives thereof if the pulses are below the bold reference lines).

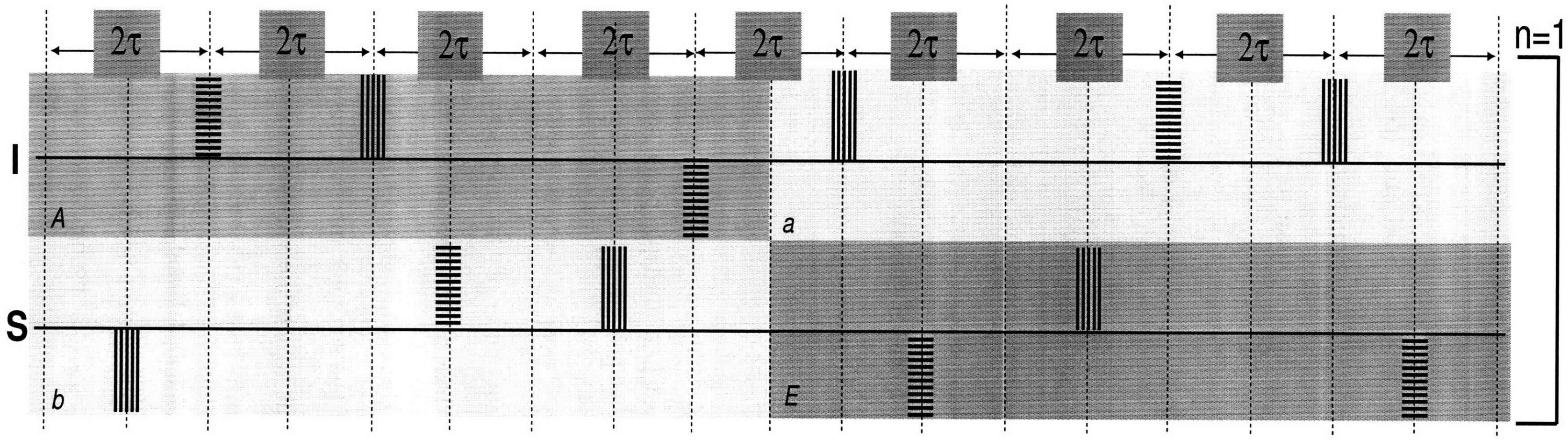

Figure 4-11: (a) The first sub-cycle (n=1) of the heteronuclear recoupling (HR-96) sequence: **I**-(Aa), **S**-(bE). The sequence is made up of 16 such sub-cycles. The horizontal striping indicates an y-pulse, vertical striping an x-pulse. All the pulses induce rotations by $\pi/2$. (or the negatives thereof if the pulses are below the bold reference lines).

4.5 The properties of the TS-96 and the HR-96 sequences

The average Hamiltonian properties of TS-96 and HR-96 are listed in Table 4.3. The HR-96 sequence scales down the heteronuclear interaction by a factor of $\frac{2}{9}$. For detailed calculation of the average Hamiltonian terms, please refer to the Appendix. As mentioned before, average Hamiltonian theory allows one to follow the complex path that the spin system takes when multiple pulse sequences are applied. In other words, one can calculate the rate at which the various product operators that span the interaction space average out over the whole duration of the sequence. This is especially useful considering that some of the interactions are much stronger than the others. Ideally, one would like to average out all the interactions as quickly as possible. However, considering the complexity of the problem, our approach has been to preferentially average out all the stronger interactions faster than the weaker ones. In Table 4.4 we show the rate at which the various interactions average to zero with out taking into account the finite strength of the applied RF pulses. In Table 4.5 we show the same taking into account these finite pulse width effects. Note that all undesired interactions average out within 8 sub-cycles for both sequences in the 0^{th} order approximation. However for the TS-96 sequence, we require 16 sub-cycles to average out some of the undesired interactions to the 1^{st} order approximation.

Table 4.3: The average Hamiltonian properties of the TS-96 and the HR-96 sequence taking into account finite pulse width effects

Terms of Average Hamiltonian	TS-96	HR-96
$\overline{H}_D^1(between\ \mathbf{I}\ spins)$	0	0
$\overline{H}_D^1(between\ \mathbf{S}\ spins)$	0	0
$\overline{H}_D^1(between\ \mathbf{I}\ and\ \mathbf{S}\ spins)$	0	$\frac{2}{9}$
$\overline{H}_O^0(for\ \mathbf{I}\ spins)$	0	0
$\overline{H}_O^0(for\ \mathbf{S}\ spins)$	0	0

Table 4.4: Sub-cycles at which the various interactions average to zero for the TS-96 and the HR-96 sequences *without* taking into account finite pulse width effects

Terms of the Average Hamiltonian	Number of sub-cycles	
	TS-96	HR-96
$\overline{H}_D^0$(*between* **I** *spins*)	1	1
$\overline{H}_D^0$(*between* **S** *spins*)	1	1
$\overline{H}_D^0$(*between* **I** *and* **S** *spins*)	8	–
$\overline{H}_O^0$(*for* **I** *spins*)	8	8
$\overline{H}_O^0$(*for* **S** *spins*)	8	8

Table 4.5: Sub-cycles at which the various interactions average to zero for the TS-96 and the HR-96 sequences taking into account finite pulse width effects

Terms of the Average Hamiltonian	Sub-cycle number of the TS-96	Sub-cycle number of the HR-96
$\overline{H}_D^0$(*between* **I** *spins*)	1	1
$\overline{H}_D^0$(*between* **S** *spins*)	8	2
$\overline{H}_D^0$(*between* **I** *and* **S** *spins*)	8	–
$\overline{H}_D^1$(*between* **I** *spins*)	2	2
$\overline{H}_D^1$(*between* **S** *spins*)	16	4
$\overline{H}_D^1$(*between* **I** *and* **S** *spins*)	16	–
$\overline{H}_O^0$(*for* **I** *spins*)	8	8
$\overline{H}_O^0$(*for* **S** *spins*)	8	8

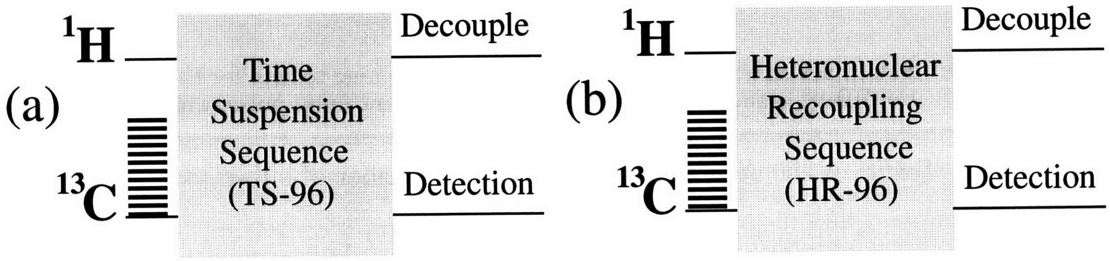

(a)
^{1}H
^{13}C
Time Suspension Sequence (TS-96)
Decouple
Detection
(b)
^{1}H
^{13}C
Heteronuclear Recoupling Sequence (HR-96)
Decouple
Detection

Figure 4-12: The schematic of the experiment that measures the effective T_2 of the ^{13}C in adamantane under (a) TS-96 sequence and (b) HR-96 sequence. Before applying the two sequences, we use a $\pi/2$ pulse to flip the ^{13}C spins on to the transverse plane. The ^{13}C magnetization is measured while decoupling the ^{1}H spins.

4.6 Experimental Results

Adamantane ($C_{10}H_{16}$) was taken as a prototypical system with an ensemble of abundant (^{1}H spins) and rare spins (the natural abundance ^{13}C spins). Adamantane undergoes rapid molecular reorientation above 160K [84]. This rapid isotropic molecular rotation averages all the intramolecular magnetic interactions to zero [84, 85]. The largest interaction in the spin system is the intermolecular homonuclear ^{1}H dipolar coupling which leads to a static proton line-width of 13,800 Hz (full-width at half maximum). The average ^{13}C dipolar coupling strength is approximately 50Hz [86] while the ^{13}C-^{1}H hetero nuclear coupling was measured to be 500Hz [87]. The T_1 relaxation times for ^{1}H and ^{13}C spins are approximately 0.5 s and 30s respectively. The experiments were carried out at room temperature at 9.4 T (^{1}H 400 MHz) using a Bruker Avance spectrometer on a 5 mm^3 powdered sample of adamantane.

4.6.1 Effective T_2 relaxation times of ^{13}C spins under the TS-96 and the HR-96 sequences.

First we tested the efficiency of the the TS-96 and the HR-96 control sequences. We used their line narrowing capabilities as measure of their efficiency. As shown in section **1**.4, the TS-96 sequence suspends all spin interactions. Thus the line narrowing efficiency of this sequence should be much superior than other time suspension sequences like the C-48 sequence. To compare the line-narrowing efficiencies of the

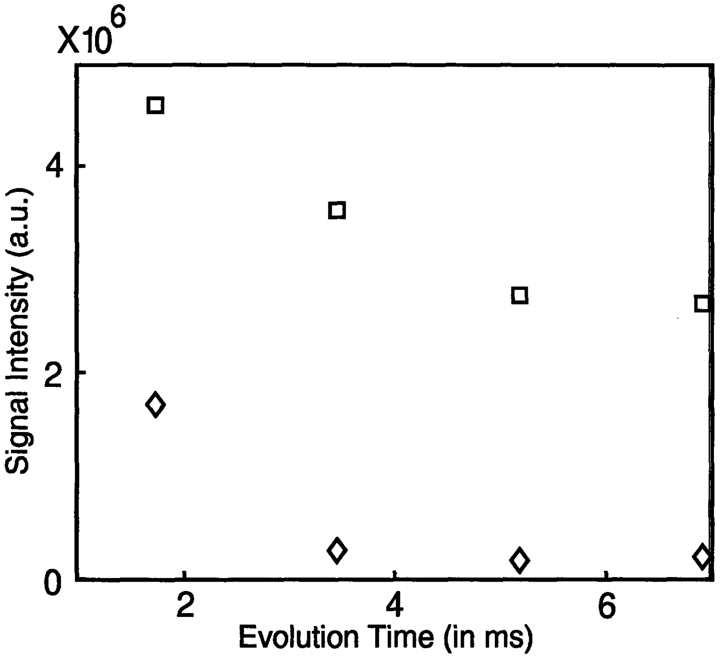

Figure 4-13: The ^{13}C signal intensity plotted after every 96- pulse cycle of the the TS-96 (□) and the HR-96 (◇) sequences. The cycle time period of 1728 μs.

different sequences, we measure the effective T_2 of ^{13}C spins for each sequence.

As shown by the schematic in Fig. 4-12, we run a set of 2-D experiments which measures the ^{13}C magnetization after every 6 pulse sub-cycle of the 96 pulse sequence. To simulate a stroboscopic measurement, the amplitude of the 5^{th} point of the free induction decay (FID) for each experiment is plotted. See Fig. 4-14. The $\pi/2$ pulse length for ^{13}C was 3.8 μs. The optimized ^{1}H $\pi/2$ pulse length was 4.8 μs. The spacing between two consecutive pulses was set at 6 μs for both sequences leading to a 6 pulse sub-cycle time of 108 μs. The effective T_2 in the case of the TS-96 sequence and the HR-96 sequence were measured to be 4.02 ms and 974 μs respectively. Note that in the case of the TS-96 sequence, the signal intensity does not go to zero at longer evolution times due to a spin-locking effect. Thus the calculated linewidths in the two cases are 75 Hz and 300 Hz respectively. We also carried out a ^{13}C observe experiment with ^{1}H decoupling using the C-48 sequence (similar to the experiments outlined in Fig. 4-12). The effective T_2 was measured to be of the order of 1 ms. These results prove that for heteronuclear spin systems, the TS-96 sequence has more efficient line-narrowing capabilities as compared to the C-48 sequence.

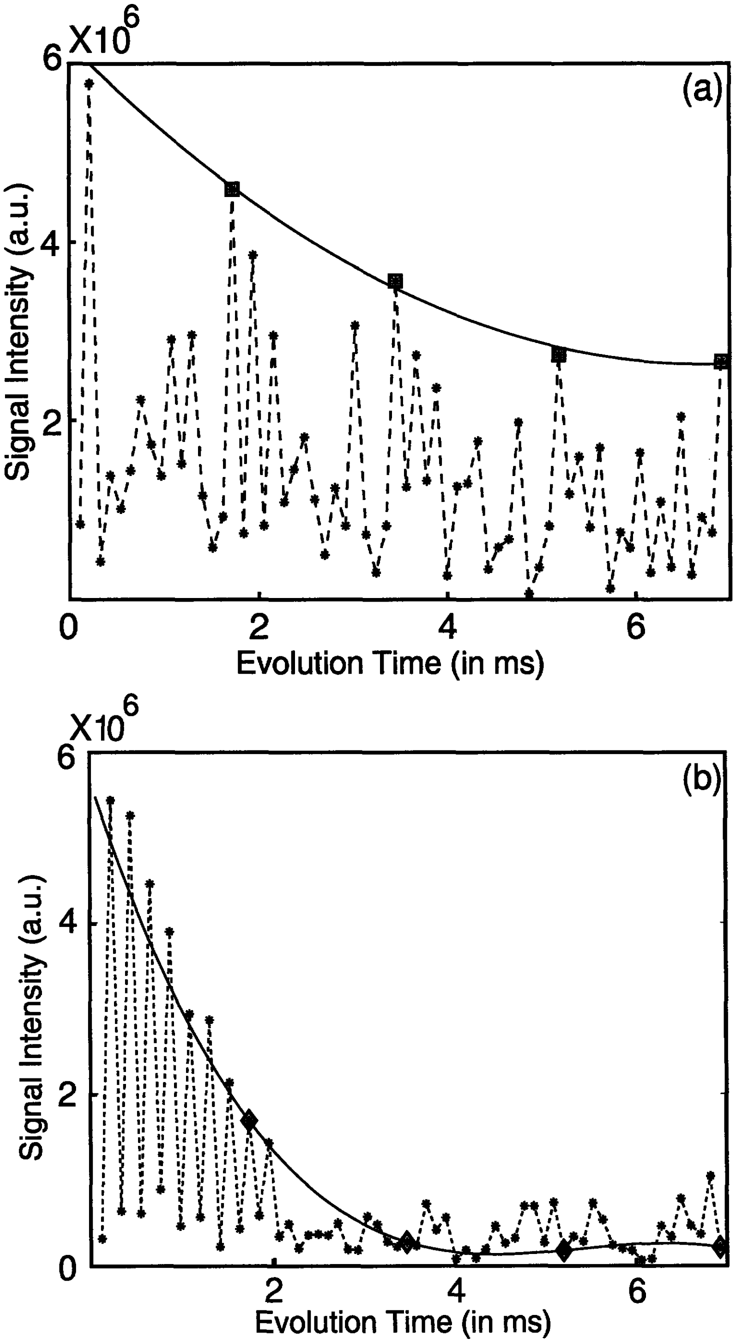

Figure 4-14: The ^{13}C signal intensity plotted after every 6 pulse sub-cycle of the (a) TS-96 and (b) HR-96 sequences. The sampling rate in both cases is 108 μs. The points marked by $\square$ in (a) and $\diamond$ in (b) indicate the signal intensity after the full 96-pulse sequence. The system was evolved up to 4 cycles of the 96-pulse sequences with a cycle time period of 1728 μs.

4.6.2 Sensitivity of ^{1}H multiple quantum coherence to the presence of ^{13}C spins

We create the ^{1}H multiple quantum coherence in adamantane by evolving the initial zeeman state ^{1}H spins under an average double quantum (DQ) Hamiltonian - $\overline{H^{II}_{DQ}}$. A collective rotation by ϕ about the z-axis is applied to this evolved state where ϕ is uniformly sampled out to a multiple of 2π. The resulting data is Fourier transformed with respect to ϕ to obtain the coherence number distribution. The evolution under $\overline{H^{II}_{DQ}}$ creates even order coherences in the z-basis. A 16-pulse DQ selective sequence – comprising of two cycles of 8 pulse sequences that compensate for pulse imperfections and resonance offsets, was used (See Fig. 4-15). To carry out the phase encoding, all the pulses in the 16 pulse experiment were phase-shifted by ϕ [10].

In Fig. 4-16, the maximum coherence encoded was ± 64 with $\Delta\phi = 2\pi/128$. The phase incrementation was carried out to 4π. The ^{13}C $\pi/2$ pulse length was 3.8 μs. The optimized ^{1}H $\pi/2$ pulse length for the DQ selective sequence was 4.3 μs. The smallest delay between the pulses, Δ, was set to 2 μs, resulting in a cycle time of 151.2 μs.

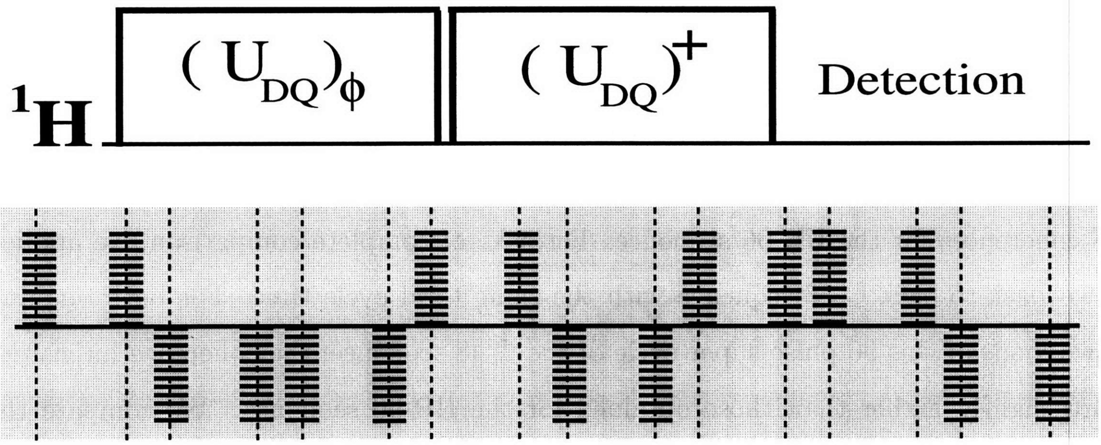

Figure 4-15: The schematic of the experiment that creates ^{1}H multiple quantum coherences in adamantane. The 16 pulse sequence in the shaded box is used to generate the effective DQ Hamiltonian. The smaller spacing between the pulses is given by Δ while the larger spacing is given by the sum of 2Δ and the $\pi/2$ pulse length. Thus the cycle time of the sequence is $t_c = 24(\Delta + \pi/2$ pulse length). The vertical striping indicates an x-pulse. All the pulses induce rotations by $\pi/2$. (or the negatives thereof if the pulses are below the bold reference lines)

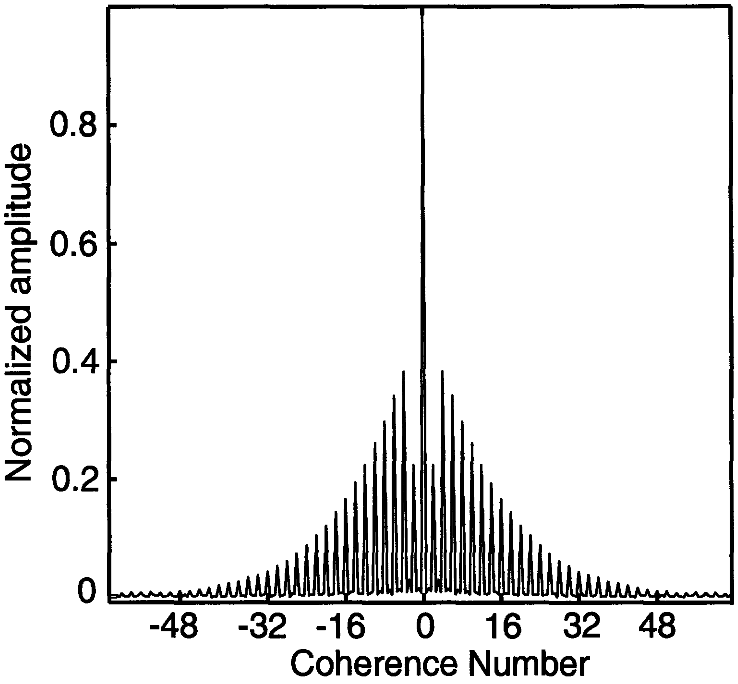

Figure 4-16: The ^{1}H multiple quantum coherence in adamantane. The system was evolved under the DQ Hamiltonian for a period of 604.8 μs.

We then carry out the experiments outlined in Fig. 4-7. The cycle times of the TS-96 and the HR-96 sequences were set to 1.4 ms. At the end of one cycle of the TS-96 and HR-96 sequences, we can observe up to 32 coherences - though the magnitudes of the coherences in the case of the HR-96 sequence are substantially lower. See Fig. 4-17(a). At the end of two cycles, this difference becomes more pronounced. While in the case of TS-96 sequence we observe up to 24 coherences, we do not observe beyond 8 coherences for the HR-96 sequence. For sake of complete comparison, we applied two back-to-back C-48 sequence with the same total cycle time. For both one and two loops of this 96 pulse super-cycle of the C-48 sequence, the coherence intensities are slightly higher than those obtained for the HR-96 sequence. We compare the net change in intensity of the coherence orders after one loop of the TS-96 and the HR-96 sequences. We observe that as the coherence order increases, the net change in intensity also increases. Thus the sensitivity of the multiple-spin state to the presence of ^{13}C spins increase with the number of correlated ^{1}H spins in the multiple-spin state. We discuss our results in more details in the next section.

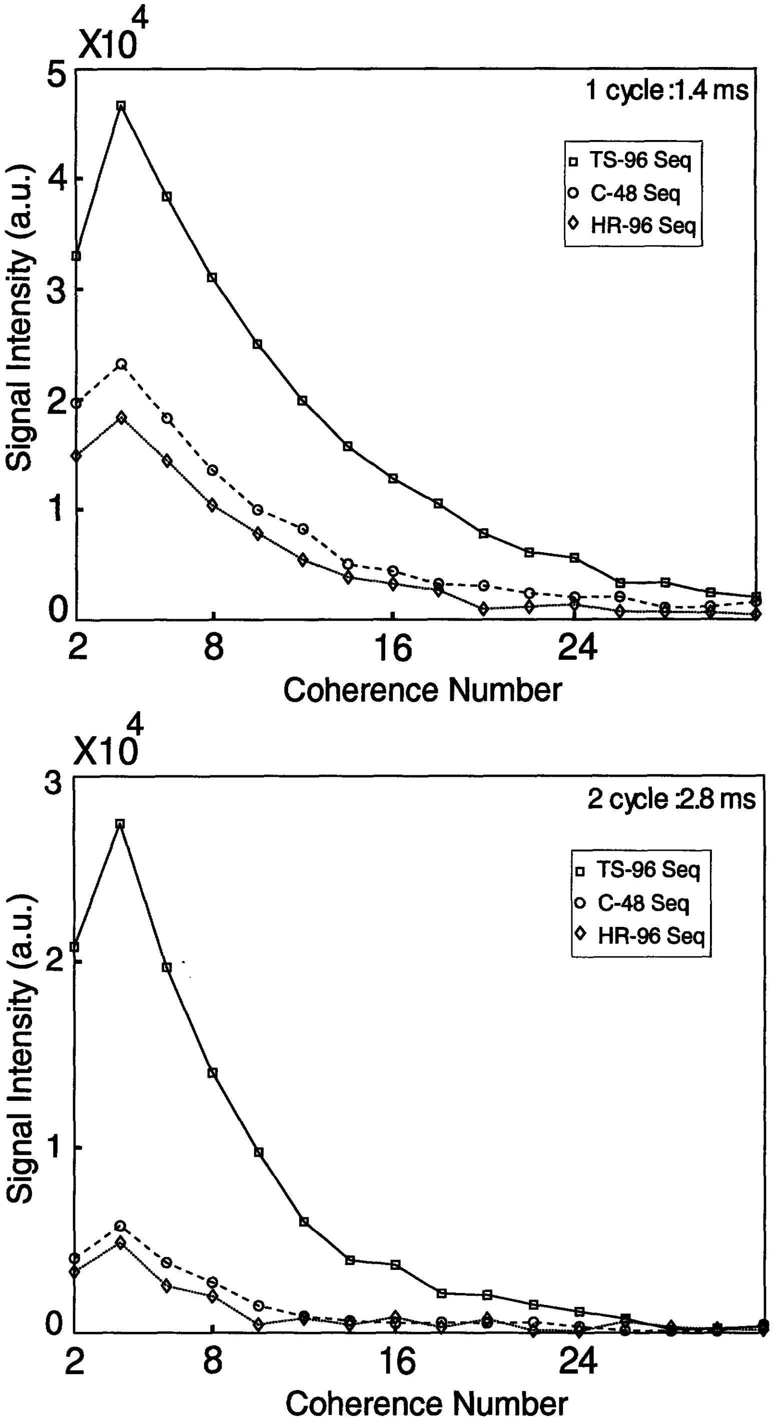

Figure 4-17: Coherence order distribution after evolution under the TS-96 (solid line), two back-to-back C-48 (dashed line) and the HR-96 (dotted line) sequences. The cycle time was 1.4ms for all three sequences. Thus, the time period of evolution (τ_2) were 1.4 ms (for the top figure) and 2.8 ms (for the bottom figure).

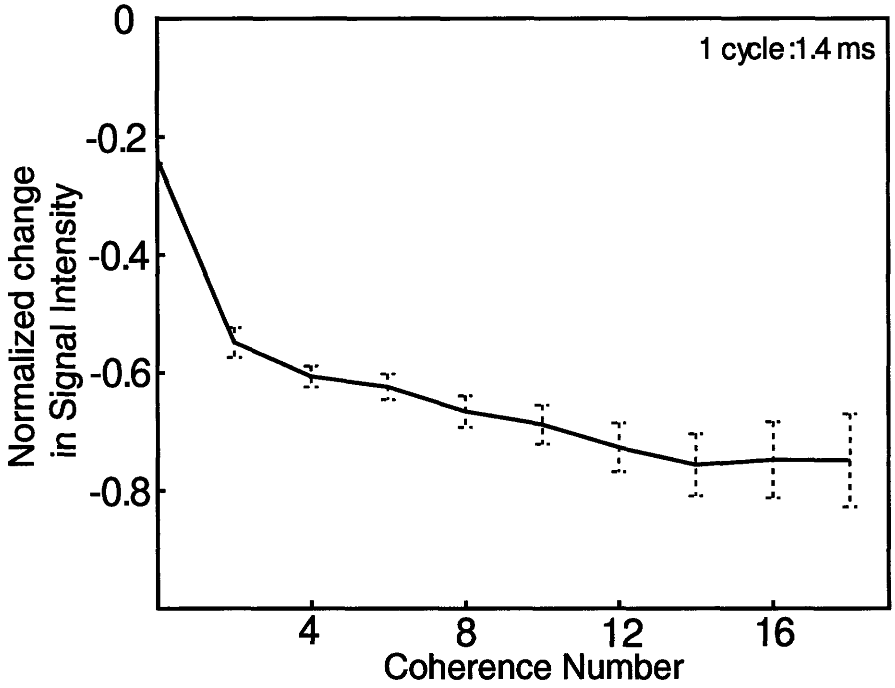

Figure 4-18: The net difference in signal intensity for the various coherence orders after one cycle of the TS-96 and HR-96 sequences.

4.7 Conclusions and future work

In this chapter, we made an attempt to understand the decay behavior of the highly correlated multiple-quantum spin-^{19}F states observed in CaF_2. We used adamantane as a test-bed to study the effect of the rare spins on the correlated multi-spin dynamics for a variety of reasons. Unlike the spin-7/2 ^{43}Ca spins, all the spins in adamantane are spin-1/2. Thus designing the multiple-pulse sequences were much simpler since we could ignore the quadrapolar spin interactions associated with a spin-7/2 system. Furthermore, the absence of intramolecular interactions, the weaker dipolar interactions and the low T_1 times are factors that contribute to the suitability of adamantane for these multiple-quantum experiments.

For our sensitivity measurements, we developed two multiple-pulse cycles - while the TS-96 sequence suppresses all the spin interactions in a heteronuclear system (comprising of two-spin species), the HR-96 sequence selectively reintroduces *only* the heteronuclear interaction between the spin species. Existing time-suspension sequences were designed to address interactions (chemical shift offsets and/or dipolar interactions) of a single-spin species in a spin system. Thus compared to these existing sequences, the TS-96 sequence has superior line-narrowing capabilities in such heteronuclear spin systems. Many solid-state spin systems that are studied in NMR comprise of two-spin species. Therefore this sequence could prove useful for line-narrowing experiments on similar systems.

The rate at which the various interactions average out should affect the line-narrowing capabilities (effective T_2 times) of the sequences. In adamantane, both the TS-96 and the HR-96 sequences average out the homonuclear spin-^{13}C interactions in addition to the homonuclear spin-^{1}H interactions. Comparing the rates at which these interactions are averaged out by the two sequences, we see that the homonuclear dipolar spin-^{13}C interactions are averaged out 4 times faster by the former sequence. Inspite of that, the measured effective T_2 for the spin-^{13}C was 4 times higher for the TS-96 sequence (as seen in Fig. 4-13). This suggests that the effective T_2 is highly sensitive to the heteronuclear dipolar interaction. However, this effective T_2 is still considerably less than the T_1. This could be due to the fact that this heteronuclear interaction is not being averaged out fast enough.

However compared to the C-48 sequence, the heteronuclear averaging capability of the TS-96 sequence is vastly superior. While the C-48 sequence averages out the heteronuclear interaction to the 0^{th} order without taking into account the finite pulse width effects, the TS-96 sequence averages out this interaction to the 1^{st} order while taking into account the finite pulse width effects. These factors partially contribute to the higher intensity of the coherence order distribution for the TS-96 sequence. This noticeable improvement in signal intensity for the TS-96 sequence over that of two back-to-back C-48 sequences can be seen in Fig. 4-17.

In CaF_2, the measured coherence decay patterns were very similar under both cases -(i) evolution under the internal Hamiltonian and (ii) suppression of the spin-^{19}F homonuclear and heteronuclear interactions. The decay behavior in the first case is primarily due to the fact that the multiple-quantum transitions under the action of the

^{19}F (secular) homonuclear dipolar Hamiltonian are not refocused to observable magnetization. To explain the decay behavior in the second case, we hypothesized that even though the ^{19}F-^{43}Ca interaction is decoupled, the presence of rare ^{43}Ca spins give rise to decoherence effects. Due to the finite time period over which the heteronuclear interactions are averaged out, the ^{19}F spin clusters are correlated to neighboring ^{43}Ca spins at any instant during this decoupling period. The ^{43}Ca homonuclear interaction further increases the number of correlated ^{43}Ca spins in the cluster. These interactions are not refocused to observable magnetization leading to a decay in coherence orders. The decay data in both cases showed three broad features:

- As the size of spin correlations grew (with increasing coherence numbers and/or excitation periods under the DQ Hamiltonian), the decay rates became faster.
- As the excitation period under the DQ Hamiltonian increased, the decay times under different coherence orders became more uniform.
- The relative change (reduction) in the decay times decrease with increasing excitation times under the DQ Hamiltonian.

To test our hypothesis, we demonstrated the sensitivity of the highly correlated multiple-spin states of abundant spins (^{1}H) to the presence of rare spins (^{13}C) on our test-bed system. We used the multiple-pulse sequences to selectively create correlations between the ^{13}C spins and multiple-spin states of the ^{1}H spins. We observe that the sensitivity increases with increasing coherence order of the multiple-spin states for a given excitation period under the DQ Hamiltonian. As the coherence number increases, the number of the correlated ^{1}H spins (i.e., the spin cluster size) increase. Since the number of ^{13}C spins present in the cluster also increases with increasing cluster size, the highly-correlated states corresponding to the larger spin clusters are more sensitive to the presence of the ^{13}C spins (as seen in Fig. 4-18).

In light of the above experimental observations on adamantane, some ‘plausible’ explanations for the distinct features of the coherence decay data in CaF_2 are as follows:

We can envision each defect spin as introducing a phase error to the correlated spin states in its neighborhood. When the spin cluster size is small, there are very few defect spins within a cluster. All the spins in a correlated spin state see the same phase errors. Thus the rate of decoherence of the correlated states in the cluster depends on the coherence order of the states – the higher order coherences dephase faster than the lower order ones. However as the preparation time (τ_1) becomes longer, the size of the spin clusters increases and so does the number of defect spins in a cluster. Higher number of defects leads to a higher decoherence rate for the correlated spin states in the cluster. At the same time, the phase errors introduced by these numerous defect spins (at the site of any abundant spin) become increasingly uncorrelated. Thus the decay rate of the correlated states no longer strongly depends on the coherence number of these states. It depends on the spin number i.e., the number of spins in the cluster [88]. At short preparation times, the ^{19}F spin cluster size is small and there are few ^{43}Ca spins in a cluster. The decay rates strongly depend on the coherence number of the correlated spin states. An analogous behavior is experimentally observed for ^{1}H spin correlations and the defect ^{13}C spins in adamantane as seen in Fig. 4-18. For the preparation time of 1.4ms, while the lower order coherences mostly comprise of small spin clusters, the higher order spin coherences (≥ 14) comprise of only large spin clusters and thus see more defect spins. Therefore one observes a flattening of the curve for these higher coherence orders (in Fig. 4-18) suggesting that the increasingly uncorrelated phase errors lead to a saturation of decay rates beyond a certain cluster size. It would be interesting to see how the sensitivity of the correlated states varies with coherence order for various preparation times.

In any multiple-pulse experiment, RF inhomogeneity, phase transients and finite RF pulse widths can contribute to errors in the experimental data. To negate the finite pulse width effects, we took them into consideration for our average Hamiltonian calculations for the multiple-pulse cycles. Many of the the higher order terms of the average Hamiltonian are scaled by (a power of) the RF pulse strength. Thus the shorter the RF pulse, lower will be the effect of these interaction (error) terms on the spin dynamics. All the above factors can lead to errors in the experimental implementation. At the same time, we made certain assumptions which if disregarded can lead to modifications in our initial analysis. We assumed that the inefficiencies of the multiple-quantum state creation process do not affect their subsequent decay. However, it can be shown that imperfect DQ Hamiltonian refocusing can contribute to a coherence order decay.

To conclude, our work provide some insight on the complex dynamics of highly correlated spin states in the presence of spin defects. In the process, we have also developed two multiple-pulse sequences which may have wider applications in NMR. As future work, we can further our study on the control of many spins in the presence of defect spins. One interesting control experiment is to evolve the highly correlated spin-system selectively under a heteronuclear interaction and then time-reverse the evolution. Thus by selectively correlating and then un-correlating the defect spins from the abundant spin system using multiple-pulse techniques, we can further investigate our ability of coherently controlling the defect spin interactions. We can also carry out the above sensitivity measurements on CaF_2. It might be hard to predict the performance the TS-96 and the HR-96 sequences since they were designed for spin-1/2 systems. However working in the spin-$\pm 1/2$ manifold of the spin-7/2 ^{43}Ca spin system, it would be interesting to see the results.

APPENDIX A

ZEROTH ORDER AVERAGE HAMILTONIAN CALCULATIONS FOR THE TS-96 AND THE HR-96 SEQUENCES

The zeroth order average Hamiltonian terms are scaled by a factor which is equal to the inverse of the cycle time ($t_c = 288\tau$) of the sequences.

Table A.1: The 0^{th} order heteronuclear average Hamiltonian values for the TS-96 (top) and the HR-96 (bottom) sequences

Sub-cycles numbers	TS-96		0^{th} order average Hamiltonian
	I	S	
$1-2$	$(Aa)(Bb)$	$(aE)(fB)$	$(-8\tau - \frac{8}{\omega_{rf}} + \frac{2\pi}{\omega_{rf}})\mathbf{I_z S_z}$
$3-4$	$(Cc)(Dd)$	$(dG)(hD)$	$(12\tau + \frac{12}{\omega_{rf}} - \frac{3\pi}{\omega_{rf}})\mathbf{I_z S_z}$
$5-6$	$(Ee)(Ff)$	$(bF)(eA)$	$(-8\tau - \frac{8}{\omega_{rf}} + \frac{2\pi}{\omega_{rf}})\mathbf{I_z S_z}$
$7-8$	$(Gg)(Hh)$	$(cH)(gC)$	$(12\tau + \frac{12}{\omega_{rf}} - \frac{3\pi}{\omega_{rf}})\mathbf{I_z S_z}$

Sub-cycles numbers	HR-96		0^{th} order average Hamiltonian
	I	S	
$1-2$	$(Aa)(Bb)$	$(bE)(fA)$	$(16\tau + \frac{16}{\omega_{rf}} - \frac{4\pi}{\omega_{rf}})\mathbf{I_z S_z}$
$3-4$	$(Cc)(Dd)$	$(dG)(hC)$	$(16\tau + \frac{16}{\omega_{rf}} - \frac{4\pi}{\omega_{rf}})\mathbf{I_z S_z}$
$5-6$	$(Ee)(Ff)$	$(aF)(eB)$	$(16\tau + \frac{16}{\omega_{rf}} - \frac{4\pi}{\omega_{rf}})\mathbf{I_z S_z}$
$7-8$	$(Gg)(Hh)$	$(cH)(gD)$	$(16\tau + \frac{16}{\omega_{rf}} - \frac{4\pi}{\omega_{rf}})\mathbf{I_z S_z}$

Table A.2: The 0^{th} order heteronuclear average Hamiltonian values for the TS-96 sequence

Sub-cycles number n	TS-96		0^{th} order Average Hamiltonian
	I	**S**	
$1-4$	$(Aa)(Bb)(Cc)(Dd)$	$(aE)(fB)(dG)(hD)$	$(4\tau + \frac{4}{\omega_{rf}} - \frac{\pi}{\omega_{rf}})\mathbf{I_z S_z}$
$4-8$	$(Ee)(Ff)(Gg)(Hh)$	$(bF)(eA)(cH)(gC)$	$(4\tau + \frac{4}{\omega_{rf}} - \frac{\pi}{\omega_{rf}})\mathbf{I_z S_z}$

Sub-cycles number n	TS-96		0^{th} order Average Hamiltonian
	I	**S**	
$1-8$	$(Aa)(Bb)(Cc)(Dd)(Ee)(Ff)(Gg)(Hh)$	$(aE)(fB)(dG)(hD)(bF)(eA)(cH)(gC)$	0

Table A.3: The 0^{th} order heteronuclear average Hamiltonian values for the HR-96 sequence

Sub-cycles number n	HR-96		0^{th} order Average Hamiltonian
	I	**S**	
$1-4$	$(Aa)(Bb)(Cc)(Dd)$	$(bE)(fA)(dG)(hC)$	$(32\tau + \frac{32}{\omega_{rf}} - \frac{8\pi}{\omega_{rf}})\mathbf{I_z S_z}$
$4-8$	$(Ee)(Ff)(Gg)(Hh)$	$(aF)(eB)(cH)(gD)$	$(32\tau + \frac{32}{\omega_{rf}} - \frac{8\pi}{\omega_{rf}})\mathbf{I_z S_z}$

Sub-cycles number n	HR-96		0^{th} order Average Hamiltonian
	I	**S**	
$1-8$	$(Aa)(Bb)(Cc)(Dd)(Ee)(Ff)(Gg)(Hh)$	$(bE)(fA)(dG)(hC)(aF)(eB)(cH)(gD)$	$(64\tau + \frac{64}{\omega_{rf}} - \frac{16\pi}{\omega_{rf}})\mathbf{I_z S_z}$

Table A.4: The 0^{th} order spin-**I** homonuclear average Hamiltonian values for the C-48 sequence

Sub-cycles numbers	C-48	0^{th} order Average Hamiltonian	
		Chemical Shift Term	Dipolar Term
$1-2$	$(Aa)(Bb)$	$(2\tau + \frac{4}{\omega_{rf}} - \frac{\pi}{\omega_{rf}})\mathbf{I_x} + (-2\tau - \frac{4}{\omega_{rf}} + \frac{\pi}{\omega_{rf}})\mathbf{I_y} + (2\tau + \frac{4}{\omega_{rf}} - \frac{\pi}{\omega_{rf}})\mathbf{I_z}$	0
$3-4$	$(Cc)(Dd)$	$(-2\tau - \frac{4}{\omega_{rf}} + \frac{\pi}{\omega_{rf}})\mathbf{I_x} + (2\tau + \frac{4}{\omega_{rf}} - \frac{\pi}{\omega_{rf}})\mathbf{I_y} + (2\tau + \frac{4}{\omega_{rf}} - \frac{\pi}{\omega_{rf}})\mathbf{I_z}$	0
$5-6$	$(Ee)(Ff)$	$(-2\tau - \frac{4}{\omega_{rf}} + \frac{\pi}{\omega_{rf}})\mathbf{I_x} + (2\tau + \frac{4}{\omega_{rf}} - \frac{\pi}{\omega_{rf}})\mathbf{I_y} + (-2\tau - \frac{4}{\omega_{rf}} + \frac{\pi}{\omega_{rf}})\mathbf{I_z}$	0
$7-8$	$(Gg)(Hh)$	$(2\tau + \frac{4}{\omega_{rf}} - \frac{\pi}{\omega_{rf}})\mathbf{I_x} + (-2\tau - \frac{4}{\omega_{rf}} + \frac{\pi}{\omega_{rf}})\mathbf{I_y} + (-2\tau - \frac{4}{\omega_{rf}} + \frac{\pi}{\omega_{rf}})\mathbf{I_z}$	0

Sub-cycles numbers	C-48	0^{th} order Average Hamiltonian	
		Chemical Shift Term	Dipolar Term
$1-4$	$(Aa)(Bb)(Cc)(Dd)$	$(4\tau + \frac{8}{\omega_{rf}} - \frac{2\pi}{\omega_{rf}})\mathbf{I_x} + (-4\tau - \frac{8}{\omega_{rf}} + \frac{2\pi}{\omega_{rf}})\mathbf{I_y} + (4\tau + \frac{8}{\omega_{rf}} - \frac{2\pi}{\omega_{rf}})\mathbf{I_z}$	0
$4-8$	$(Ee)(Ff)(Gg)(Hh)$	$(-4\tau - \frac{8}{\omega_{rf}} + \frac{2\pi}{\omega_{rf}})\mathbf{I_x} + (4\tau + \frac{8}{\omega_{rf}} - \frac{2\pi}{\omega_{rf}})\mathbf{I_y} + (-4\tau - \frac{8}{\omega_{rf}} + \frac{2\pi}{\omega_{rf}})\mathbf{I_z}$	0

Sub-cycles numbers	C-48	0^{th} order Average Hamiltonian	
		Chemical Shift Term	Dipolar Term
$1-4$	$(Aa)(Bb)(Cc)(Dd)(Ee)(Ff)(Gg)(Hh)$	0	0

Table A.5: The 0^{th} order spin-$\mathbf{S}$ homonuclear average Hamiltonian values for the TS-96 sequence

Sub-cycles numbers	TS-96	0^{th} order Average Hamiltonian	
		Chemical Shift Term	Dipolar Term
$1-2$	$(aE)(fB)$	$(2\tau+\frac{4}{\omega_{rf}}-\frac{\pi}{\omega_{rf}})\mathbf{S_x}+(2\tau+\frac{4}{\omega_{rf}}-\frac{\pi}{\omega_{rf}})\mathbf{S_y}+(2\tau)\mathbf{S_z}$	$(\frac{3}{\omega_{rf}})(\mathbf{S_xS_z}+\mathbf{S_zS_x}+\mathbf{S_yS_z}+\mathbf{S_zS_y})$
$3-4$	$(dG)(hD)$	$(2\tau+\frac{4}{\omega_{rf}}-\frac{\pi}{\omega_{rf}})\mathbf{S_x}+(-2\tau-\frac{4}{\omega_{rf}}+\frac{\pi}{\omega_{rf}})\mathbf{S_y}+(\frac{2}{\omega_{rf}}-\frac{\pi}{2\omega_{rf}})\mathbf{S_z}$	$(-\frac{3}{\omega_{rf}})(\mathbf{S_xS_z}+\mathbf{S_zS_x})$
$5-6$	$(bF)(eA)$	$(-2\tau-\frac{4}{\omega_{rf}}+\frac{\pi}{\omega_{rf}})\mathbf{S_x}+(-2\tau-\frac{4}{\omega_{rf}}+\frac{\pi}{\omega_{rf}})\mathbf{S_y}+(6\tau+\frac{8}{\omega_{rf}}-\frac{2\pi}{\omega_{rf}})\mathbf{S_z}$	$(-\frac{3}{\omega_{rf}})(\mathbf{S_xS_z}+\mathbf{S_zS_x}+\mathbf{S_yS_z}+\mathbf{S_zS_y}$
$7-8$	$(cH)(gC)$	$(-2\tau-\frac{4}{\omega_{rf}}+\frac{\pi}{\omega_{rf}})\mathbf{S_x}+(2\tau+\frac{4}{\omega_{rf}}-\frac{\pi}{\omega_{rf}})\mathbf{S_y}+(-4\tau-\frac{6}{\omega_{rf}}+\frac{3\pi}{2\omega_{rf}})\mathbf{S_z}$	$(\frac{3}{\omega_{rf}})(\mathbf{S_xS_z}+\mathbf{S_zS_x})$

Sub-cycles numbers	TS-96	0^{th} order Average Hamiltonian	
		Chemical Shift Term	Dipolar Term
$1-4$	$(aE)(fB)(dG)(hD)$	$(4\tau+\frac{8}{\omega_{rf}}-\frac{2\pi}{\omega_{rf}})\mathbf{S_x}+(2\tau+\frac{2}{\omega_{rf}}-\frac{\pi}{2\omega_{rf}})\mathbf{S_z}$	$(\frac{3}{\omega_{rf}})(\mathbf{S_yS_z}+\mathbf{S_zS_y})$
$5-8$	$(bF)(eA)(cH)(gD)$	$(-4\tau-\frac{8}{\omega_{rf}}+\frac{2\pi}{\omega_{rf}})\mathbf{S_x}+(2\tau+\frac{2}{\omega_{rf}}-\frac{\pi}{2\omega_{rf}})\mathbf{S_z}$	$(-\frac{3}{\omega_{rf}})(\mathbf{S_yS_z}+\mathbf{S_zS_y})$

Sub-cycles numbers	TS-96	0^{th} order Average Hamiltonian	
		Chemical Shift Term	Dipolar Term
$1-8$	$(aE)(fB)(dG)(hD)(bF)(eA)(cH)(gD)$	0	0

Table A.6: The 0^{th} order spin-$\mathbf{S}$ homonuclear average Hamiltonian values for the HR-96 sequence

Sub-cycles numbers	HR-96	0^{th} order Average Hamiltonian	
		Chemical Shift Term	Dipolar Term
$1-2$	$(bE)(fA)$	$(-2\tau - \frac{4}{\omega_{rf}} + \frac{\pi}{\omega_{rf}})\mathbf{S_x} + (2\tau + \frac{4}{\omega_{rf}} - \frac{\pi}{\omega_{rf}})\mathbf{S_y} + (2\tau + \frac{4}{\omega_{rf}} - \frac{\pi}{\omega_{rf}})\mathbf{S_z}$	0
$3-4$	$(dG)(hC)$	$(2\tau + \frac{4}{\omega_{rf}} - \frac{\pi}{\omega_{rf}})\mathbf{S_x} + (-2\tau - \frac{4}{\omega_{rf}} + \frac{\pi}{\omega_{rf}})\mathbf{S_y} + (2\tau + \frac{4}{\omega_{rf}} - \frac{\pi}{\omega_{rf}})\mathbf{S_z}$	0
$5-6$	$(aF)(eB)$	$(2\tau + \frac{4}{\omega_{rf}} - \frac{\pi}{\omega_{rf}})\mathbf{S_x} + (-2\tau - \frac{4}{\omega_{rf}} + \frac{\pi}{\omega_{rf}})\mathbf{S_y} + (-2\tau - \frac{4}{\omega_{rf}} + \frac{2\pi}{\omega_{rf}})\mathbf{S_z}$	0
$7-8$	$(cH)(gD)$	$(-2\tau - \frac{4}{\omega_{rf}} + \frac{\pi}{\omega_{rf}})\mathbf{S_x} + (2\tau + \frac{4}{\omega_{rf}} - \frac{\pi}{\omega_{rf}})\mathbf{S_y} + (-2\tau - \frac{4}{\omega_{rf}} + \frac{\pi}{\omega_{rf}})\mathbf{S_z}$	0

Sub-cycles numbers	HR-96	0^{th} order Average Hamiltonian	
		Chemical Shift Term	Dipolar Term
$1-4$	$(bE)(fA)(dG)(hC)$	$(-4\tau - \frac{8}{\omega_{rf}} + \frac{2\pi}{\omega_{rf}})\mathbf{S_x} + (4\tau + \frac{8}{\omega_{rf}} - \frac{2\pi}{\omega_{rf}})\mathbf{S_y} + (4\tau + \frac{8}{\omega_{rf}} - \frac{2\pi}{\omega_{rf}})\mathbf{S_z}$	0
$5-8$	$(aF)(eB)(cH)(gD)$	$(4\tau + \frac{8}{\omega_{rf}} - \frac{2\pi}{\omega_{rf}})\mathbf{S_x} + (-4\tau - \frac{8}{\omega_{rf}} + \frac{2\pi}{\omega_{rf}})\mathbf{S_y} + (-4\tau - \frac{8}{\omega_{rf}} + \frac{2\pi}{\omega_{rf}})\mathbf{S_z}$	0

Sub-cycles numbers	HR-96	0^{th} order Average Hamiltonian	
		Chemical Shift Term	Dipolar Term
$1-8$	$(bE)(fA)(dG)(hC)(aF)(eB)(cH)(gD)$	0	0

BIBLIOGRAPHY

[1] J. I. Cirac and P. Zoller. *Phys. Rev. Lett.*, **74**:4094, 1995.

[2] P. Grangier and G. Reymond and N. Schlosser. *Fortschr. Phys*, **48**:859, 2000.

[3] J. E. Mooij and T. P. Orlando and L. Levitov and L. Tian and C. H. VanderWal and S. LLyod. *Science*, **285**:1036, 1999.

[4] D. G. Cory and A. F. Fahmy and T. F. Havel. *Proc. Nat. Acad. Sci. USA*, **94**:1634, 1997.

[5] I. L. Chuang and N. A. Gershenfeld. *Science*, **275**:350, 1997.

[6] D. G. Cory and R. Laflamme and E. Knill and L. Viola and T. F. Havel and N. Boulant and G. Boutis and E. Fortunato and S. Lloyd and R. Martinez. *Fortschr. Phys*, **48**:975, 2000.

[7] B. E. Kane. *Nature*, **393**:133, 1998.

[8] D. Suter and K. Lim. *Phys. Rev. A*, **65**:052309, 2002.

[9] H. Cho and D. G. Cory and C. Ramanathan. *J. Chem. Phys.*, **118**:3686, 2003.

[10] C. Ramanathan and H. Cho and P. Capperallo and G. S. Boutis and D. G. Cory. *Chem. Phys. Lett.*, **369**:311, 2003.

[11] H. Cho and T. D. Ladd and J. Baugh and D. G. Cory and C. Ramanathan. *Phys. Rev. B*, **118**:3686, 2003.

[12] H. G. Krojanski and D. Suter. *Phys. Rev. Lett.*, **93**:090501-1, 2004.

[13] W. Zhang and D. G. Cory. *Phys. Rev. Lett.*, **80**:1324, 1998.

[14] G. S. Boutis and D. Greenbaum and H. Cho and D. G. Cory and C. Ramanathan. *Phys. Rev. Lett.*, **92**:137201, 2004.

[15] G. S. Agarwal and R. R. Puri. *Phys. Rev. A*, **41**:3782, 1990.

[16] C. H. Bennett, D. P. DiVincenzo, J. A. Smolin, and W. K. Wootters. *Phys. Rev. A*, **54**:3824, 1996.

[17] S. H. Chen and M. Kotlarchyk. *Interactions of photons and neutrons with matter.* World Scientific Publ., 1997.

[18] A. R. Usha Devi, X. Wang, and B. C. Sanders. *Quantum Inform. Processing*, **2**:207, 2003.

[19] L.-M. Duan, A. Sorensen, J. I. Chirac, and P. Zoller. *Phys. Rev. Lett.*, **85**:3991, 2000.

[20] A. R. Edmonds. *Angular Momentum in Quantum Mechanics.* Princeton Univ. Press, 1974.

[21] E. M. Fortunato, M. A. Pravia, N. Boulant, G. Teklemariam, T. F. Havel, and D. G. Cory. *J. Chem. Phys.*, **116**:7599, 2002.

[22] R. Freeman. *Spin Choreography.* Oxford Univ. Press, 1998.

[23] T. F. Havel, S. S. Somaroo, C.-H. Tseng, and D. G. Cory. In T. Beth and M. Grassl, editors, *Applicable Algebra in Engineering, Communications and Computing*, volume 10, pages 339–374, Berlin, 2000. Springer-Verlag.

[24] S. Hill and W. K. Wootters. *Phys. Rev. Lett.*, **78**:5022, 1997.

[25] M. Kitagawa and M. Ueda. *Phys. Rev. A*, **47**:5138, 1993.

[26] A. Kuzmich, L. Mandel, and N. P. Bigelow. *Phys. Rev. Lett.*, **85**:1594, 2000.

[27] R. Laflamme, E. Knill, D. G. Cory, E. M. Fortunato, T. F. Havel, C. Miquel, R. Martinez, C. Negrevergne, G. Ortiz, M. A. Pravia, Y. Sharf, S. Sinha, R. Somma, and L. Viola. *Los Alamos Science*, **27**:2, 2002.

[28] R. Laflamme, E. Knill, W. H. Zurek, P. Catasti, and S. Marathan. *Phil. Trans. R. Soc. Lond. A*, **356**:1941, 1998.

[29] D. A. Meyer and N. R. Wallach. *J. Math. Phys.*, **43**:4273, 2002.

[30] M. A. Nielsen and I. L. Chuang. *Quantum Computation and Quantum Information.* Cambridge Univ. Press, 2000.

[31] M. A. Pravia, N. Boulant, J. Emerson, A. Farid, E. M. Fortunato, T. F. Havel, R. Martinez, and D. G. Cory. *J. Chem. Phys.*, **119**:9993, 2003.

[32] M. D. Price, T. F. Havel, and D. G. Cory. *Phys. D*, **120**:82, 1998.

[33] M. E. Rose. *Elementary theory of Angular Momentum.* John Wiley & Sons, 1957. Reprinted by Dover Publ., 1995.

[34] M. O. Scully. *Quantum Optics.* Cambridge Univ. Press, 1997.

[35] A.J. Shaka and R. Freeman. *J. Magn. Reson.*, **55**:487, 1983.

[36] A. Sorensen, L.-M. Duan, J. I. Cirac, and P. Zoller. *Nature*, **409**:63, 2001.

[37] A. Sorensen and K. Molmer. *Phys. Rev. A*, **83**:2274, 1999.

[38] A. Sorensen and K. Molmer. *Phys. Rev. Lett.*, **83**:2274, 1999.

[39] G. Teklemariam, E. M. Fortunato, M. A. Pravia, T. F. Havel, and D. G. Cory. *Phys. Rev. Lett.*, **86**:5845, 2001.

[40] Xiaoguang Wang and K. Molmer. *Eur. Phys. J. D*, **18**:385, 2002.

[41] Y. S. Weinstein, M. A. Pravia, E. M. Fortunato, S. Lloyd, and D. G. Cory. *Phys. Rev. Lett.*, **86**:1889, 2001.

[42] D. J. Wineland, J. J. Bollinger, W. M. Itano, and F.L. Moore. *Phys. Rev. A*, **46**:6797, 1992.

[43] D. J. Wineland, J.J. Bollinger, W. M. Itano, and D. J. Heinzen. *Phys. Rev. A*, **50**:67, 1994.

[44] K. Wodkiewicz. *J. Mod. Opt.*, **34**:941, 1987.

[45] K. Wodkiewicz and J. Eberly. *J. Opt. Soc. Am. B*, **2**:458, 1985.

[46] W. K. Wootters. *Phys. Rev. Lett.*, **80**:2245, 1998.

[47] J. Wrachtrup and S. Y. Kilin and A. P. Nizovtsev. *Opt. Spectrosc+*, **91**:429, 2001.

[48] T. D. Ladd and J. R. Goldman and F. Yamaguchi and Y. Yamamoto. *Phys. Rev. Lett.*, **89**:017901, 2002.

[49] S. Vega and Y. Naor. *J. Chem. Phys.*, **75**:75, 1981.

[50] M. Mehring. *High Resolution NMR Spectroscopy in Solids.* Springer-Verlag, Berlin, 1983.

[51] U. Haeberlen. *High Resolution NMR in Solids.* Academic Press, New York, 1976.

[52] A. Keller. *Adv. Magn. Reson.*, **12**:183, 1990.

[53] A. Pines and D. J. Ruben and S. Vega and M. Mehring. *Phys. Rev. Lett.*, **36**:110, 1976.

[54] A. Pines and S. Vega and M. Mehring. *Phys. Rev. B*, **18**:112, 1978.

[55] J. Waugh and U. Haeberlen. *Phys. Rev.*, **175**:453, 1968.

[56] G. Pake *J. Chem. Phys.*, **16**:327, 1948.

[57] The signal was measured using a solid echo sequence. The amplitude of the 15th point on the acquired data was then either plotted against the duration of the RF modulation or Fourier transformed to yield a spectrum.

[58] U. Haeberlen and J. S. Waugh. *Phys. Rev.*, **175**:453, 1968.

[59] M. Munowitz and A. Pines. *Adv. Chem. Phys.*, **66**:1, 1987.

[60] D. P. Weitekamp. *Adv. Magn. Reson.*, **11**:111, 1983.

[61] G. Drobny. *Ann. Rev. Phys. Chem.*, **26**:451, 1985.

[62] Y. S. Yen and A. Pines. *J. Chem. Phys.*, **78**:3579, 1982.

[63] J. Baum and and M. Munowitz and A. N. Garroway and A. Pines. *J. Chem. Phys.*, **83**:2015, 1985.

[64] J. Baum and A. Pines. *J. Am. Chem. Soc.*, **108**:7447, 1986.

[65] R. Tycko. *J. Magn. Reson.*, **139**:302, 1999.

[66] M. Munowitz and A. Pines. *Science*, **233**:525, 1986.

[67] S. Lacelle and S. J. Hwang and B. C. Gerstein. *J. Chem. Phys.*, **99**:8407, 1993.

[68] E. B. Feldman and S. Lacelle. *J. Chem. Phys.*, **107**:7067, 1977.

[69] S. Lacelle. *J. Magn. Reson.*, **16**:193, 1991.

[70] D. A. Lathrop and E. S. Handy and K. K. Gleason. *J. Magn. Reson. Series A.*, **111**:161, 1994.

[71] M. Munowitz and A. Pines and M. Mehring. *J. Chem. Phys.*, **86**:3172, 1987.

[72] S. Zhang and B. H. Meier and R. R. Ernst. *Sol. Stat. Nucl. Magn. Reson.*, **1**:313, 1992.

[73] M. Maricq *Phys. Rev. B*, **25**:6622, 1982.

[74] C. H. Wang and J. D. Ramshaw. *Phys. Rev. B*, **6**:3253, 1972.

[75] P. Mansfield and U. Haeberlen. *Z. Naturforch*, **28**:1081, 1973.

[76] P. Mansfield and P. K. Grannell. *Phys. Rev. B*, **12**:3618, 1975.

[77] H. M. Cho and C. J. Lee and D. N. Shykind and D. P. Weitekamp. *Phys. Rev. Lett.*, **55**:1923, 1985.

[78] D. G. Cory and J. B. Miller and R. Turner and A. N. Garroway. *Mol. Phys.*, **70**:331, 1990.

[79] D. P. Weitekamp and J. R. Garbow and A. Pines. *J. Chem. Phys.*, **77**:2870, 1982.

[80] P. Caravatti and L. Braunschweiler and R. R. Ernst. *Chem. Phys. Lett.*, **100**:305, 1983.

[81] J. S. Waugh and L. M. Huber and U. Haeberlen. *Phys. Rev. Lett.*, **20**:180, 1968.

[82] W. K. Rhim and D. D. Elleman and R. W. Vaugan. *J. Chem. Phys.*, **58**:1772, 1973.

[83] D. G. Cory and J. B. Miller and A. N. Garroway. *J. Mag. Reson.*, **90**:205, 1990.

[84] H. A. Resing. *Mol. Cryst. Liq. Cryst.*, **9**:101, 1969.

[85] A. Pines and M. G. Gibby and J. S. Waugh. *J. Chem. Phys.*, **56**:1776, 1972.

[86] A. N. Garroway. *J. Magn. Reson.*, **28**:365, 1977.

[87] C. E. Bronniman and N. M. Szeverenyi and G. E. Maciel. *Mol. Phys.*, **70**:331, 1990.

[88] A. Fedorov and L. Fedichkin. *J. Phys. Cond. Mat.*, **18**:3217, 2006.